

NUMERICAL MODELLING OF EXHUMATION OF HIGH PRESSURE - LOW
TEMPERATURE METAMORPHIC ROCKS: A CASE STUDY OF TAVSANLI
AND AFYON ZONE IN WESTERN ANATOLIA

by

Ömer Faruk Bodur

B.S, Physics, Boğaziçi University, 2013

Submitted to Kandilli Observatory and Earthquake
Research Institute in partial fulfillment of
the requirements for the degree of
Master of Science

Graduate Program in Geophysics

Boğaziçi University

2016

ACKNOWLEDGEMENTS

I have been helped and encouraged greatly by many friends and colleagues at Kandilli Observatory and Earthquake Research Institute and Eurasia Institute of Earth Sciences, without whom this work would not be accomplished. I am very grateful to Prof. Nurcan Meral Özel, Prof. Özgün Konca, Prof. Mustafa Aktar, Prof. Niyazi Türkelli, Prof. Bülent Tank, V. Tayfun Ulusoy, Prof. Hadi Özbal, Prof. Russell Pysklywec, Prof. Aral Okay, Prof. Gültekin Topuz, Assist. Prof. Tuna Eken and Erkan Gün.

I am also thankful for my family who always backed me up and Cemre Öztan for her invaluable help on every matter.

This work would not be possible without the support of The Scientific and Technological Research Council of Turkey. The project I was involved was funded by TÜBİTAK (project ID 113Y200).

My final thanks must go to Prof. Hayrullah Karabulut and my co-advisor Assoc. Prof. Oğuz Göğüş for their invaluable help on my thesis, advice on issues related to my academic career plans and support in my scientific pursuits.

ABSTRACT

NUMERICAL MODELLING OF EXHUMATION OF HIGH PRESSURE - LOW TEMPERATURE METAMORPHIC ROCKS: A CASE STUDY OF TAVSANLI AND AFYON ZONE IN WESTERN ANATOLIA

Despite many numerical modeling works on burial and exhumation of crustal rocks, the formation of metamorphic rocks in **High Pressure / Low Temperature (HP/LT)** region and mechanism of their exhumation are poorly constrained. The metamorphic rocks in Tavsanlı and Afyon Zone have high P/T ratios and they are represented by blueschist and greenschist to blueschist transitional rocks, respectively. The mechanism of burial and exhumation of crustal rocks were investigated by performing numerical experiments such as subduction of oceanic plate under the continental margin, intra-oceanic subduction and post-collision. Rheological constraints on exhumation of HP/LT rocks are presented. The numerical modelling results for subduction settings indicate that lithospheric mantle deforming in viscous rheology is the key factor to preserve the temperature of buried crustal rocks in subduction channel, whereas continental lithospheric mantle deforming in frictional plastic rheology gives metamorphic rocks in higher pressures and temperatures. The weaker crust and viscous rheology imposed in continental lithospheric mantle provides metamorphic rocks with P-T conditions comparable to Tavsanlı Zone; strong crust and viscous rheology in continental lithospheric mantle gives metamorphic rocks with P-T conditions in agreement with Afyon Zone. In post-collision setting, the numerical modelling results show that weaker crust with high Moho temperature are the necessary conditions for exhumation of crustal rocks in high temperature / high pressure region.

ÖZET

YÜKSEK BASINÇ DÜŞÜK SICAKLIK METAMORFİK KAYALARININ YÜZEYLENMESİNİN SAYISAL OLARAK MODELLENMESİ: BATI ANADOLUDA TAVŞANLI VE AFYON ZONLARI ÜZERİNE UYGULAMA

Literatürde kayaların gömülme ve yüzeylenme mekanizması üzerine önemli sayısal modelleme çalışmaları bulunmasına rağmen, Yüksek Basınç - Düşük Sıcaklık (HP/LT) kayalarının gömülme ve yüzeylenme mekanizması tam olarak bilinmemektedir. Tavşanlı ve Afyon Zonlarında bulunan metamorfik kayalar yüksek P/T oranına sahiptir ve bu kayalar sırayla mavişist ile mavişist - yeşilşist geçiş kayaları olarak tanımlanmaktadır. Kabuk kayalarının gömülme ve yüzeylenme mekanizması okyanusal levhanın kıta altına dalması, okyanus ortası yitim ve çarpışma sonrası gibi tektonik konfigürasyonlarda sayısal deney dizileriyle incelenmiş, yüksek basınç / düşük sıcaklık metamorfizması ve yüzeylenme mekanizması üzerine reolojik kısıtlamalar sunulmuştur. Yitim deneyleri sonuçlarına göre, kıtasal litosferik mantonun deformasyon tipinin akışkan (Newtonian) olması yitim kanalına gömülen kayaların sıcaklık değerlerini korumada ana faktör olurken, kırılğan deformasyonda kayalar daha yüksek basınç ve sıcaklık değerlerine sahip olmuşlardır. Zayıf kabuk ile akışkan reolojide kıtasal litosferik manto Tavşanlı Zonu metamorfik kayaları; güçlü kabuk ve akışkan reolojide kıtasal litosferik manto ise Afyon Zonu metamorfik kayaları basınç - sıcaklık değerlerine uygun sonuçlar vermektedir. Çarpışma sonrası tektoniğinde ise zayıf kabuk ile yüksek Moho sıcaklığı yüksek basınç / yüksek sıcaklık değerlerinde metamorfik kayaların yüzeylenmesini sağlamaktadır.

TABLE OF CONTENTS

ACKNOWLEDGEMENTS	iii
ABSTRACT	iv
ÖZET	v
LIST OF FIGURES	viii
LIST OF TABLES	xx
LIST OF SYMBOLS/ABBREVIATIONS	xxi
1. INTRODUCTION	1
1.1. Metamorphism of Rocks	1
1.2. Tectonics of Metamorphism and Exhumation of crustal rocks	5
1.2.1. Proposed Models for Burial and Exhumation	6
1.2.2. Slab Breakoff	7
1.2.3. Subduction Channel Flow	7
1.2.4. Slab Rollback	8
1.2.5. Delamination	8
1.3. Geological Setting of Afyon and Tavşanlı Zone	9
1.3.1. Spatial Distribution of Metamorphic Units and P-T Conditions	10
1.3.2. Temporal Constraints	11
2. EXPERIMENTS AND RESULTS	12
2.1. Explanation of The Numerical Model	12
2.1.1. The Principle Equations	12
2.1.2. Flow Parameters of Materials	14
2.2. Rheology of Lithosphere	16
2.3. Boundary Conditions	18
2.4. Post-collision	22
2.4.1. Experimental Set A1	22
2.4.2. Results of A1	24
2.4.3. Experimental Set A2	29
2.4.4. Results of A2	31
2.4.5. Experimental Set A3	36

2.4.6. Results of A3	38
2.4.7. Experimental Set A4	42
2.4.8. Results of A4	44
2.4.9. Experimental Set B1	48
2.4.10. Results of B1	50
2.4.11. Experimental Set B2	55
2.4.12. Results of B2	57
2.4.13. Experimental Set B3	61
2.4.14. Results of B3	63
2.5. Subduction of Oceanic Plate Under The Continental Margin	66
2.5.1. Experimental Set C1	66
2.5.2. Results of C1	68
2.5.3. Experimental Set C2	79
2.5.4. Results of C2	81
2.5.5. Experimental Set C3	92
2.5.6. Results of C3	94
2.6. Intra-Oceanic Subduction	105
2.6.1. Experimental Set D1	105
2.6.2. Results of D1	107
2.6.3. Experimental Set D2	113
2.6.4. Results of D2	115
3. DISCUSSION AND CONCLUSION	118
REFERENCES	122

LIST OF FIGURES

Figure 1.1.	Temperature profile (thick line) and melting curve (dashed line) between the surface and the centre of the Earth. (Modified from Stüwe, 2007)	2
Figure 1.2.	Metamorphic facies diagram. BS:blueschist, GS:greenschist, AM:amphibolite, EA:epidote-amphibolite, GR:granulite, Amp-EC:amphibole-eclogite, HGR:high pressure granulite, Lw-EC:lawsonite-eclogite.(Liou et al., 2004 [1])	2
Figure 1.3.	World U(HP) terranes (some of the major ones) [2–11]. Compiled from Liou et al., (2009) [12]; Warren (2013) [13].	5
Figure 1.4.	Proposed models of burial and exhumation of crustal rocks. Stars denote the tracked particles. Pressure-Temperature-Time (P-T-t) paths are depicted on the right for each model. (Modified from Hacker and Gerya, (2013) [14])	6
Figure 1.5.	Tectonic and geological Map of Western and Central Turkey. (Modified from Okay and Tüysüz, (1999); [15] Pourteau et al., (2010) [16])	9
Figure 2.1.	Effective viscosity vs. strain rate plot for the materials in Table (1.2). Reference temperatures are shown on the lower left.	15
Figure 2.2.	A) Models of deformation. B) Brace-Goetze failure envelopes for a thermotectonic age of 150 Ma, a weak, undried granulite lower crust, a uniform strain rate of $10^{-15} s^{-1}$ (Burov and Watts, (2006) [17]).	17

Figure 2.3.	Initial model configurations. Each color represent a different layer. Eulerian and Lagrangian partitioning are shown in the model box.	18
Figure 2.4.	C) Oceanic plate subduction model. D) Intra-oceanic subduction model. Each colour represents a different layer. Eulerian and Lagrangian partitioning are shown in the model box.	19
Figure 2.5.	Model configuration and flow parameters for the materials of experimental set A1.	23
Figure 2.6.	Model development and P-T-t paths of tracked particles of experiment A1 with Moho temperature of 450°C (A) after 6.4 Ma, (B) after 12.8 Ma. Blue: crust, Orange: lithospheric mantle, Brown: asthenosphere.	25
Figure 2.7.	Model development and P-T-t paths of tracked particles of experiment A1 with Moho temperature of 600°C (A) after 6.4 Ma, (B) after 12.8 Ma. Blue: crust, Orange: lithospheric mantle, Brown: asthenosphere.	26
Figure 2.8.	Model development and P-T-t paths of tracked particles of experiment A1 with Moho temperature of 750°C (A) after 6.4 Ma, (B) after 12.8 Ma. Blue: crust, Orange: lithospheric mantle, Brown: asthenosphere.	27
Figure 2.9.	Model development and P-T-t paths of tracked particles of experiment A1 with Moho temperature of 900°C (A) after 6.4 Ma, (B) after 12.8 Ma. Blue: crust, Orange: lithospheric mantle, Brown: asthenosphere.	28
Figure 2.10.	Model configuration and flow parameters for the materials of experimental set A2.	30

Figure 2.11. Model development and P-T-t paths of tracked particles of experiment A2 with Moho temperature of 450°C (A) after 6.4 Ma, (B) after 12.8 Ma. Blue: crust, Orange: lithospheric mantle, Brown: asthenosphere.	32
Figure 2.12. Model development and P-T-t paths of tracked particles of experiment A2 with Moho temperature of 600°C (A) after 6.4 Ma, (B) after 12.8 Ma. Blue: crust, Orange: lithospheric mantle, Brown: asthenosphere.	33
Figure 2.13. Model development and P-T-t paths of tracked particles of experiment A2 with Moho temperature of 750°C (A) after 6.4 Ma, (B) after 12.8 Ma. Blue: crust, Orange: lithospheric mantle, Brown: asthenosphere.	34
Figure 2.14. Model development and P-T-t paths of tracked particles of experiment A2 with Moho temperature of 900°C (A) after 6.4 Ma, (B) after 12.8 Ma. Blue: crust, Orange: lithospheric mantle, Brown: asthenosphere.	35
Figure 2.15. Model configuration and flow parameters for the materials of experimental set A3.	37
Figure 2.16. Model development and P-T-t paths of tracked particles of experiment A3 with activation energy of 223 kJ/mol in the crust (A) after 6.4 Ma, (B) after 12.8 Ma. Blue: crust, Orange: lithospheric mantle, Brown: asthenosphere.	39
Figure 2.17. Model development and P-T-t paths of tracked particles of experiment A3 with activation energy of 133 kJ/mol in the crust (A) after 4.8 Ma, (B) after 12.8 Ma. Blue: crust, Orange: lithospheric mantle, Brown: asthenosphere.	40

Figure 2.18. Model development and P-T-t paths of tracked particles of experiment A3 with activation energy of 43 kJ/mol in the crust (A) after 4.8 Ma, (B) after 12.8 Ma. Blue: crust, Orange: lithospheric mantle, Brown: asthenosphere.	41
Figure 2.19. Model configuration and flow parameters for the materials of experimental set A4.	43
Figure 2.20. Model development and P-T-t paths of tracked particles of experiment A4 with activation energy of 223 kJ/mol in the crust (A) after 3.2 Ma, (B) after 14.5 Ma. Blue: crust, Orange: lithospheric mantle, Brown: asthenosphere.	45
Figure 2.21. Model development and P-T-t paths of tracked particles of experiment A4 with activation energy of 133 kJ/mol in the crust (A) after 3.2 Ma, (B) after 14.5 Ma. Blue: crust, Orange: lithospheric mantle, Brown: asthenosphere.	46
Figure 2.22. Model development and P-T-t paths of tracked particles of experiment A4 with activation energy of 43 kJ/mol in the crust (A) after 3.2 Ma, (B) after 14.5 Ma. Blue: crust, Orange: lithospheric mantle, Brown: asthenosphere.	47
Figure 2.23. Model configuration and flow parameters for the materials of experimental set B1.	49
Figure 2.24. Model development and P-T-t paths of tracked particles of experiment B1 with Moho temperature of 450°C (A) after 3.2 Ma, (B) after 11.3 Ma. Blue: upper/middle crust, Brown: lower crust, Green: lith. mantle, Orange: asthenosphere.	51

Figure 2.25. Model development and P-T-t paths of tracked particles of experiment B1 with Moho temperature of 600°C (A) after 3.2 Ma, (B) after 11.3 Ma. Blue: upper/middle crust, Brown: lower crust, Green: lith. mantle, Orange: asthenosphere.	52
Figure 2.26. Model development and P-T-t paths of tracked particles of experiment B1 with Moho temperature of 750°C (A) after 3.2 Ma, (B) after 11.3 Ma. Blue: upper/middle crust, Brown: lower crust, Green: lith. mantle, Orange: asthenosphere.	53
Figure 2.27. Model development and P-T-t paths of tracked particles of experiment B1 with Moho temperature of 900°C (A) after 3.2 Ma, (B) after 11.3 Ma. Blue: upper/middle crust, Brown: lower crust, Green: lith. mantle, Orange: asthenosphere.	54
Figure 2.28. Model configuration and flow parameters for the materials of experimental set B2.	56
Figure 2.29. Model development and P-T-t paths of tracked particles of experiment B2 with activation energy of 223 kJ/mol in the u/m crust (A) after 3.2 Ma, (B) after 11.3 Ma. Blue: u/m crust, Brown: low. crust, Green: lith. mantle, Orange: asth.	58
Figure 2.30. Model development and P-T-t paths of tracked particles of experiment B2 with activation energy of 133 kJ/mol in the u/m crust (A) after 3.2 Ma, (B) after 11.3 Ma. Blue: u/m crust, Brown: low. crust, Green: lith. mantle, Orange: asth.	59
Figure 2.31. Model development and P-T-t paths of tracked particles of experiment B2 with activation energy of 43 kJ/mol in the u/m crust (A) after 3.2 Ma, (B) after 11.3 Ma. Blue: u/m crust, Brown: low. crust, Green: lith. mantle, Orange: asth.	60

Figure 2.32. Model configuration and flow parameters for the materials of experimental set B3.	62
Figure 2.33. Model development and P-T-t paths of tracked particles of experiment B3 with activation energy of 223 kJ/mol in the u/m crust (A) after 3.2 Ma, (B) after 11.3 Ma. Blue: u/m crust, Brown: low. crust, Green: lith. mantle, Orange: asth.	64
Figure 2.34. Model development and P-T-t paths of tracked particles of experiment B3 with activation energy of 43 kJ/mol in the u/m crust (A) after 1.6 Ma, (B) after 6.4 Ma. Blue: u/m crust, Brown: low. crust, Green: lith. mantle, Orange: asth.	65
Figure 2.35. Model configuration and flow parameters for the materials of experimental set C1.	67
Figure 2.36. The positions of tracked lagrangian nodes (rocks) placed on the initial model configuration for the experimental set C1. Red: crust, Blue: continental lith. mantle, Yellow: oceanic lith. mantle, Orange: asthenosphere. Light Blue: weak zone.	70
Figure 2.37. Model development and P-T-t paths of tracked particles of experiment C1 with convergence rate of 2 cm/yr (A) after 6.4 Ma, (B) after 12.9 Ma. Red: crust, Blue: continental lith. mantle, Yellow: oceanic lith. mantle, Orange: asthenosphere.	71
Figure 2.38. Model development and P-T-t paths of tracked particles of experiment C1 with convergence rate of 2 cm/yr after 25.7 Ma. Red: crust, Blue: continental lith. mantle, Yellow: oceanic lith. mantle, Orange: asthenosphere.	72

Figure 2.39. Model development and P-T-t paths of tracked particles of experiment C1 with convergence rate of 3 cm/yr (A) after 6.4 Ma, (B) after 12.9 Ma. Red: crust, Blue: continental lith. mantle, Yellow: oceanic lith. mantle, Orange: asthenosphere.	73
Figure 2.40. Model development and P-T-t paths of tracked particles of experiment C1 with convergence rate of 3 cm/yr after 25.7 Ma. Red: crust, Blue: continental lith. mantle, Yellow: oceanic lith. mantle, Orange: asthenosphere.	74
Figure 2.41. Model development and P-T-t paths of tracked particles of experiment C1 with convergence rate of 4 cm/yr (A) after 6.4 Ma, (B) after 12.9 Ma. Red: crust, Blue: continental lith. mantle, Yellow: oceanic lith. mantle, Orange: asthenosphere.	75
Figure 2.42. Model development and P-T-t paths of tracked particles of experiment C1 with convergence rate of 4 cm/yr after 25.7 Ma. Red: crust, Blue: continental lith. mantle, Yellow: oceanic lith. mantle, Orange: asthenosphere.	76
Figure 2.43. Model development and P-T-t paths of tracked particles of experiment C1 with convergence rate of 5 cm/yr (A) after 6.4 Ma, (B) after 12.9 Ma. Red: crust, Blue: continental lith. mantle, Yellow: oceanic lith. mantle, Orange: asthenosphere.	77
Figure 2.44. Model development and P-T-t paths of tracked particles of experiment C1 with convergence rate of 5 cm/yr after 25.7 Ma. Red: crust, Blue: continental lith. mantle, Yellow: oceanic lith. mantle, Orange: asthenosphere.	78
Figure 2.45. Model configuration and flow parameters for the materials of experimental set C2.	80

- Figure 2.46. The positions of tracked lagrangian nodes (rocks) placed on the initial model configuration for the experimental set C2. Red: crust, Blue: continental lith. mantle, Yellow: oceanic lith. mantle, Orange: asthenosphere. Light Blue: weak zone. 83
- Figure 2.47. Model development and P-T-t paths of tracked particles of experiment C2 with convergence rate of 0 cm/yr (A) after 5.5 Ma, (B) after 9.7 Ma. Red: crust, Blue: continental lith. mantle, Yellow: oceanic lith. mantle, Orange: asthenosphere. 84
- Figure 2.48. Model development and P-T-t paths of tracked particles of experiment C2 with convergence rate of 0 cm/yr after 14.2 Ma. Red: crust, Blue: continental lith. mantle, Yellow: oceanic lith. mantle, Orange: asthenosphere. 85
- Figure 2.49. Model development and P-T-t paths of tracked particles of experiment C2 with convergence rate of 1 cm/yr (A) after 5.5 Ma, (B) after 9.7 Ma. Red: crust, Blue: continental lith. mantle, Yellow: oceanic lith. mantle, Orange: asthenosphere. 86
- Figure 2.50. Model development and P-T-t paths of tracked particles of experiment C2 with convergence rate of 1 cm/yr (A) after 14.2 Ma, (B) after 17.4 Ma. Red: crust, Blue: continental lith. mantle, Yellow: oceanic lith. mantle, Orange: asth. 87
- Figure 2.51. Model development and P-T-t paths of tracked particles of experiment C2 with convergence rate of 2 cm/yr (A) after 5.5 Ma, (B) after 9.7 Ma. Red: crust, Blue: continental lith. mantle, Yellow: oceanic lith. mantle, Orange: asthenosphere. 88

Figure 2.52. Model development and P-T-t paths of tracked particles of experiment C2 with convergence rate of 2 cm/yr (A) after 14.2 Ma, (B) after 17.4 Ma. Red: crust, Blue: continental lith. mantle, Yellow: oceanic lith. mantle, Orange: asth.	89
Figure 2.53. Model development and P-T-t paths of tracked particles of experiment C2 with convergence rate of 3 cm/yr (A) after 5.5 Ma, (B) after 9.7 Ma. Red: crust, Blue: continental lith. mantle, Yellow: oceanic lith. mantle, Orange: asthenosphere.	90
Figure 2.54. Model development and P-T-t paths of tracked particles of experiment C2 with convergence rate of 3 cm/yr (A) after 14.2 Ma, (B) after 17.4 Ma. Red: crust, Blue: continental lith. mantle, Yellow: oceanic lith. mantle, Orange: asth.	91
Figure 2.55. Model configuration and flow parameters for the materials of experimental set C3.	93
Figure 2.56. The positions of tracked lagrangian nodes (rocks) placed on the initial model configuration for the experimental set C3. Red: crust, Blue: continental lith. mantle, Yellow: oceanic lith. mantle, Orange: asthenosphere. Light Blue: weak zone.	96
Figure 2.57. Model development and P-T-t paths of tracked particles of experiment C3 with convergence rate of 0 cm/yr (A) after 4.8 Ma, (B) after 6.8 Ma. Red: crust, Blue: continental lith. mantle, Yellow: oceanic lith. mantle, Orange: asthenosphere.	97
Figure 2.58. Model development and P-T-t paths of tracked particles of experiment C3 with convergence rate of 0 cm/yr after 13.5 Ma. Red: crust, Blue: continental lith. mantle, Yellow: oceanic lith. mantle, Orange: asthenosphere.	98

Figure 2.59. Model development and P-T-t paths of tracked particles of experiment C3 with convergence rate of 1 cm/yr (A) after 4.8 Ma, (B) after 6.8 Ma. Red: crust, Blue: continental lith. mantle, Yellow: oceanic lith. mantle, Orange: asthenosphere.	99
Figure 2.60. Model development and P-T-t paths of tracked particles of experiment C3 with convergence rate of 1 cm/yr after 13.5 Ma. Red: crust, Blue: continental lith. mantle, Yellow: oceanic lith. mantle, Orange: asthenosphere.	100
Figure 2.61. Model development and P-T-t paths of tracked particles of experiment C3 with convergence rate of 2 cm/yr (A) after 4.8 Ma, (B) after 6.8 Ma. Red: crust, Blue: continental lith. mantle, Yellow: oceanic lith. mantle, Orange: asthenosphere.	101
Figure 2.62. Model development and P-T-t paths of tracked particles of experiment C3 with convergence rate of 2 cm/yr after 13.5 Ma. Red: crust, Blue: continental lith. mantle, Yellow: oceanic lith. mantle, Orange: asthenosphere.	102
Figure 2.63. Model development and P-T-t paths of tracked particles of experiment C3 with convergence rate of 3 cm/yr (A) after 4.8 Ma, (B) after 6.8 Ma. Red: crust, Blue: continental lith. mantle, Yellow: oceanic lith. mantle, Orange: asthenosphere.	103
Figure 2.64. Model development and P-T-t paths of tracked particles of experiment C3 with convergence rate of 3 cm/yr after 13.5 Ma. Red: crust, Blue: continental lith. mantle, Yellow: oceanic lith. mantle, Orange: asthenosphere.	104
Figure 2.65. Model configuration and flow parameters for the materials of experimental set D1.	106

- Figure 2.66. Model results and P-T-t paths in exp. D1(plastic lith.) (A)after 6 Ma, (B)after 12 Ma. Blue(light/dark):crust/oceanic slab, Pink:cont. lith. mantle, Green:asth. Brown:cont. margin, Purple/Orange:young/old oceanic crust. 109
- Figure 2.67. Model results and P-T-t paths in exp. D1(plastic lith.) after 42 Ma. Blue(light/dark):crust/oceanic slab, Pink:cont. lith. mantle, Green:asth. Brown:cont. margin, Purple/Orange:young/old oceanic crust. 110
- Figure 2.68. Model results and P-T-t paths in exp. D1(viscous lith.) (A)after 6 Ma, (B)after 12 Ma. Blue(light/dark):crust/oceanic slab, Pink:cont. lith. mantle, Green:asth. Brown:cont. margin, Purple/Orange:young/old oceanic crust. 111
- Figure 2.69. Model results and P-T-t paths in exp. D1(viscous lith.) after 42 Ma. Blue(light/dark):crust/oceanic slab, Pink:cont. lith. mantle, Green:asth. Brown:cont. margin, Purple/Orange:young/old oceanic crust. 112
- Figure 2.70. Model configuration and flow parameters for the materials of experimental set D2. 114
- Figure 2.71. Model results and P-T-t paths in exp. D2(viscoplastic crust.) (A)after 4 Ma, (B)after 8 Ma. Blue(light/dark):crust/oceanic slab, Pink:cont. lith. mantle, Green:asth. Brown:cont. margin, Purple/Orange:young/old oceanic crust. 116
- Figure 2.72. Model results and P-T-t paths in exp. D2(viscoplastic crust.) after 28 Ma. Blue(light/dark):crust/oceanic slab, Pink:cont. lith. mantle, Green:asth. Brown:cont. margin, Purple/Orange:young/old oceanic crust. 117

Figure 3.1. Maximum pressure-temperature values for the whole set of experiments. The results are compared with other works and natural data in the literature. 119

LIST OF TABLES

Table 1.1.	Metamorphic rocks and their protoliths. (Bucher and Frey, 1994) [18]	4
Table 2.1.	Flow parameters of major rock types. Compiled from various sources [19–21].	15

LIST OF SYMBOLS/ABBREVIATIONS

AZ	Afyon Zone
BFZ	Bornova Flysch Zone
HP	High Pressure
HT	High Temperature
LAB	Lithosphere - Asthenosphere Boundary
LT	Low Temperature
P-T-t	Pressure - Temperature - Time
TZ	Tavsanli Zone
UHP	Ultra High Pressure

1. INTRODUCTION

1.1. Metamorphism of Rocks

Metamorphism encompasses changes in texture and mineralogy of sedimentary, igneous or metamorphic rocks [22, 23]. These changes - depending on the geodynamic setting- occur in a whole spectrum of pressure - temperature conditions [18]. The physical/chemical bonds between groups of minerals can be broken if the vibrational or other form of intrinsic energy is increased. The increase in temperature might also lead to vaporization of volatiles in the rock. The atoms can form a different orientation at higher temperatures. It is important to note that this change accounts for metamorphism constrained to the condition that it must not be first by melting. In other words, if a rock changes first by melting, then the rock forms when it cools is a new igneous rock, and if a rock changes by first breaking down into sediment, then the rock that forms when the sediment lithifies is a new sedimentary rock. Therefore, the material must sustain its solid state during the whole process. [18, 22]

Heating causes vibrations in the atomic level [24–26]. These vibrations can be absorbed by the atoms or groups of atoms. After some level, upon breaking of the bonds, a new, high standing (to temperature) bonds might form. The end product happens to be different in orientation and possibly in composition especially when exposed to different mineral groups or atoms [27]. The formation of a new crystal from crystals is called recrystallization. It takes place more rapidly at higher temperatures than at lower, because bonds vibrate faster and break more frequently as the temperature increases.

When crustal or oceanic rocks are buried, not only their temperatures are increased, but also they are pressurized, in other words, the lithostatic pressure increases as we go deeper down to the centre of the Earth [28]. As it can be seen from Figure 1.1, the temperature continuously increases with depth as well.

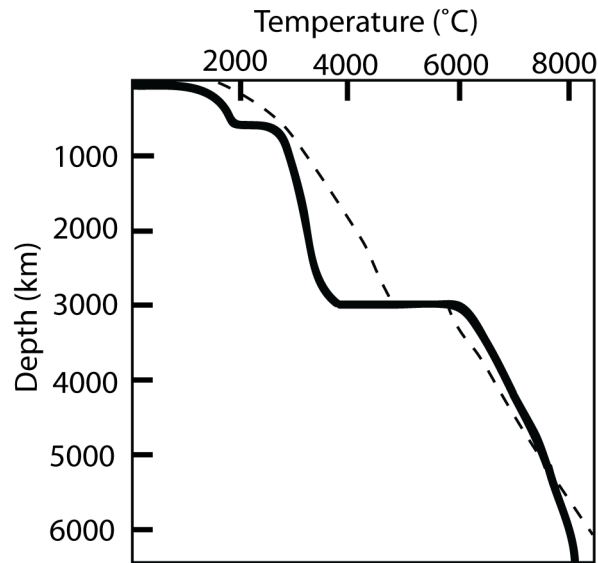


Figure 1.1. Temperature profile (thick line) and melting curve (dashed line) between the surface and the centre of the Earth. (Modified from Stüwe, 2007)

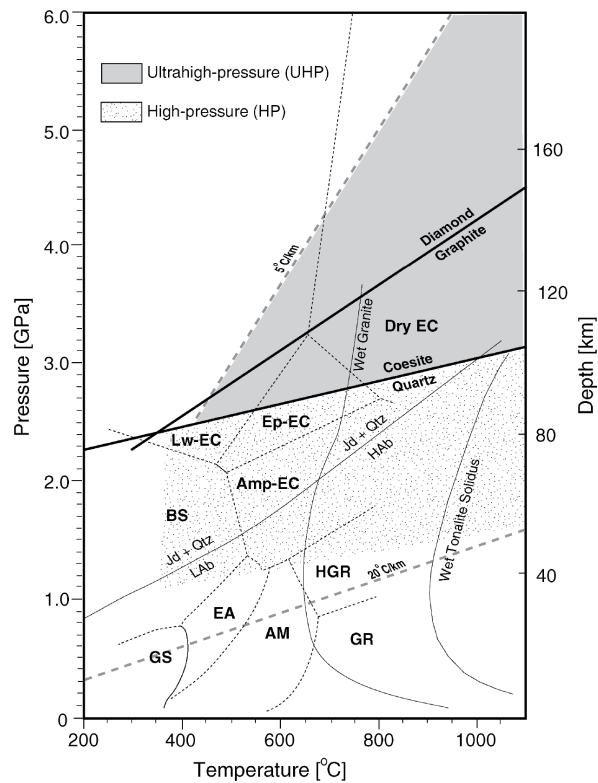


Figure 1.2. Metamorphic facies diagram. BS:blueschist, GS:greenschist, AM:amphibolite, EA:epidote-amphibolite, GR:granulite, Amp-EC:amphibole-eclogite, HGR:high pressure granulite, Lw-EC:lawsonite-eclogite.(Liou et al., 2004 [1])

The diagrams of metamorphic facies is a good reference to classify the grade of metamorphism according to their P-T conditions (Figure 1.2).

Quartz-Coesite line in Figure 1.2 is generally accepted as the boundary for transition from high pressure (HP) to ultra-high pressure (UHP) region. The possible lowest geotherm ($5\text{ }^{\circ}\text{C}/\text{km}$) is also shown as dashed line in the same graph.

Protoliths (the original rock) of metamorphic rocks can be sedimentary, magmatic and metamorphic rocks as well [18]. The distinction between crustal and oceanic rocks is of major importance when we are dealing with tectonic interpretation of the formation of metamorphic rocks.

Metamorphism can occur in various geodynamic settings. A hot magma may intrude as a pluton into a sedimentary rock (shale, limestone, and sandstone) at a depth of about 2 km below the Earth's surface. Heat can slowly transfer from the pluton to the surrounding sedimentary (country) rock. The heat provided by the pluton can not melt the country rock, but it can heat the country rock sufficiently to cause recrystallization. A region of metamorphic aureole might form in this condition. Metamorphism caused by heat conducted into country rock from an igneous intrusion is called thermal metamorphism [18].

In this work, what we are dealing is the tectonic metamorphism, in other words, the burial of crustal rocks and their exposure to heat and pressure in a tectonic environment such as ocean or continent subduction and collision. Tectonic processes providing formation, preservation and exhumation of metamorphic rocks are highly debated [14]. Before delving into this subject, let's consider the seven chemical composition classes of metamorphic rocks as given in Table 1.1.

To give an example for metamorphic rocks, a red shale (sedimentary rock composed of clay, very fine quartz, and hematite) may yield a coarse-grained metamorphic rock consisting of alternating dark and light bands. [22]

Table 1.1. Metamorphic rocks and their protoliths. (Bucher and Frey, 1994) [18]

Metamorphic Rock	Protolith
Metaultramafic Rocks	Usually mantle derived, very Mg-rich family of rocks. Typical composition: Peridotite.
Metacarbonate Rocks	Sedimentary rocks modally dominated by carbonate minerals. Examples: limestones, marbles.
Metapelites (Shales)	Most common type of sedimentary rocks.
Metamafic Rocks	Mafic igneous rocks, mainly badsalts and of lesser importance, gabbros.
Metaquartzo Feldspathic Rocks	Rocks of sedimentary (sandstones) or igneous (granites) origin.
Other Bulk Compositions	Manganese sediments, ironstones, alkaline igneous rocks, etc.

1.2. Tectonics of Metamorphism and Exhumation of crustal rocks

Blueschist and eclogite facies rocks are found in various Phanerozoic orogenic belts (Figure 1.3) [3, 5–10, 29, 30]. It is clearly seen that most of the metamorphism events happen to be in mountain belts. This is related to plate tectonic interactions. The Alpine-Himalayan orogenic belt hosts many of the well known metamorphic terranes.

Metamorphic rocks are characterized by pressures of metamorphism corresponding to depths far exceeding the average thickness of the continental crust. For this work, we ignore the idea that nonlithostatic pressure applied to crustal rocks in collision belts could result in significant pressures on the rocks, that might lead to a wrong interpretation of the burial history of metamorphic rocks when they are investigated based on simple depth-pressure relationship [31]. Additionally, in this context, exhumation is defined as upward displacement of the rocks with respect to the surface [32].

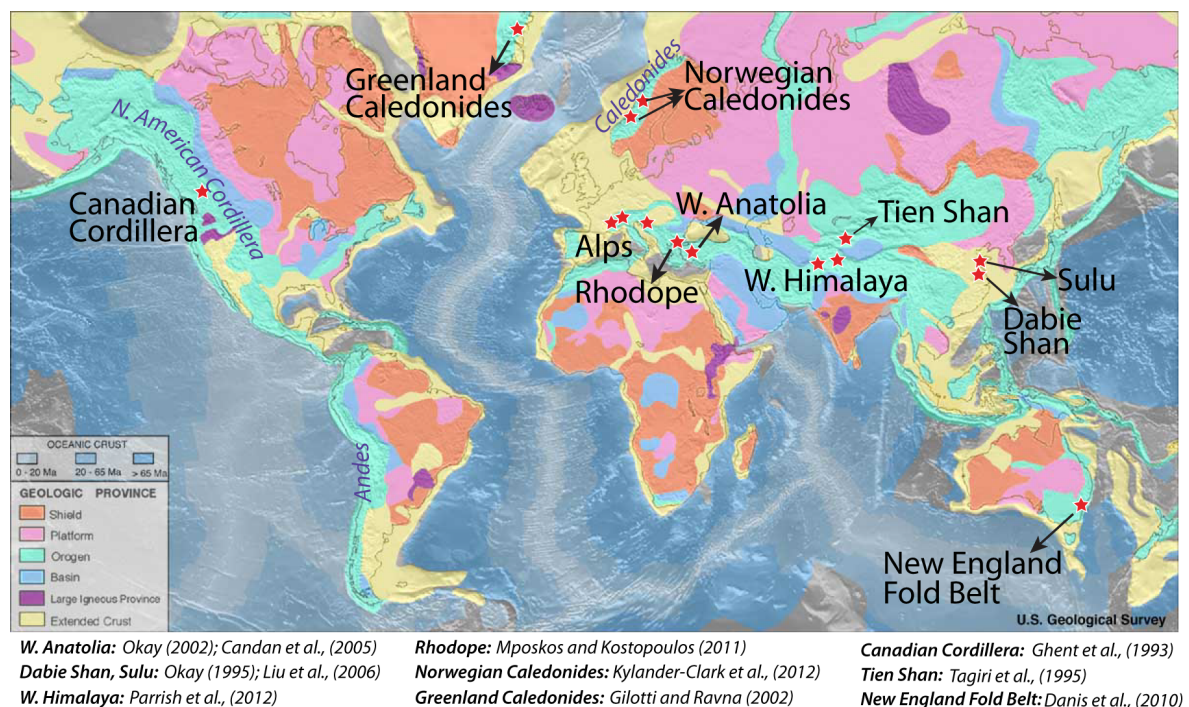


Figure 1.3. World U(HP) terranes (some of the major ones) [2–11]. Compiled from Liou et al., (2009) [12]; Warren (2013) [13].

1.2.1. Proposed Models for Burial and Exhumation

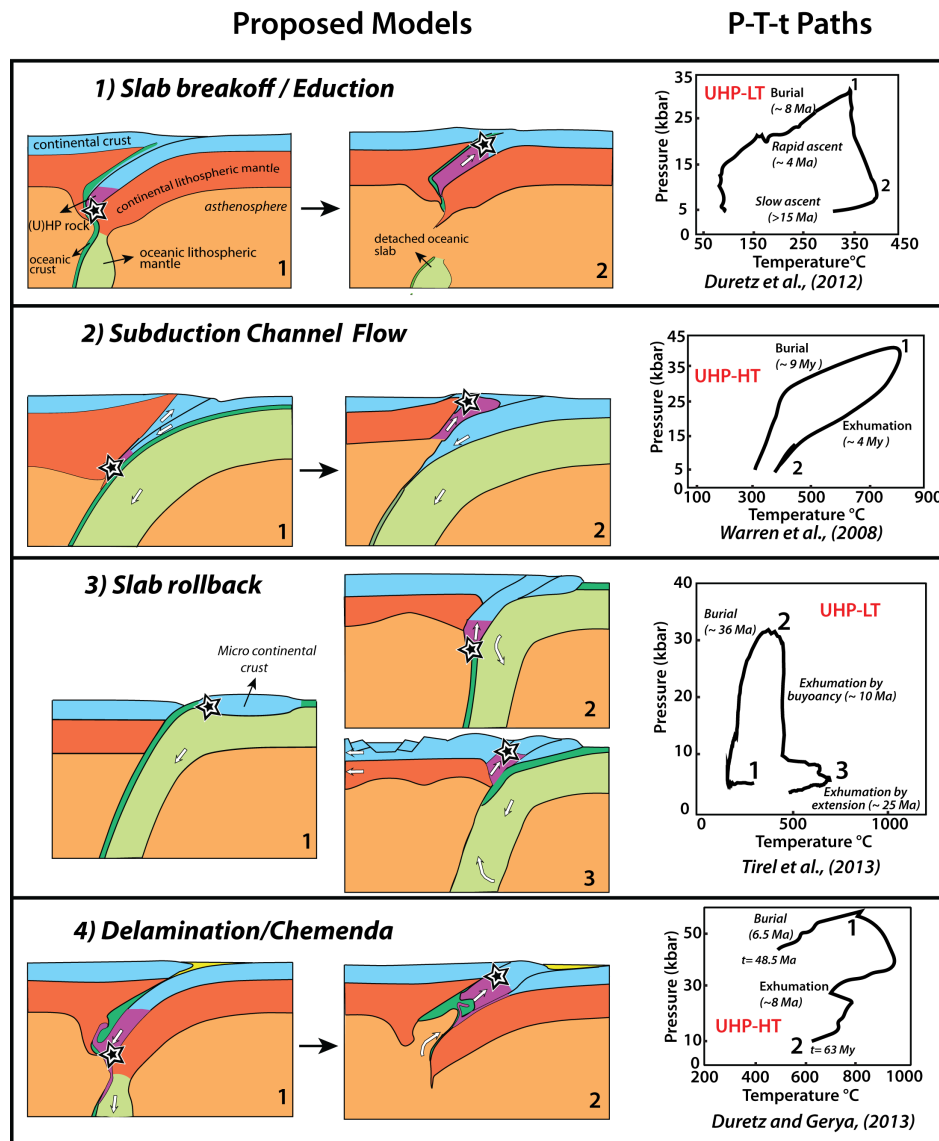


Figure 1.4. Proposed models of burial and exhumation of crustal rocks. Stars denote the tracked particles. Pressure-Temperature-Time (P-T-t) paths are depicted on the right for each model. (Modified from Hacker and Gerya, (2013) [14])

Many constraints on burial and exhumation of high-pressure (HP) and ultra-high-pressure (UHP) rocks of crustal origin have been documented by numerical and analogue experiments [13, 33–43]. It is widely accepted that continental subduction following an oceanic plate subduction is the major tectonic process providing burial and exhumation of crustal rocks [13, 14, 36]. The proposed tectonic models in the literature are classified and presented in Figure 1.4.

1.2.2. Slab Breakoff

In this tectonic configuration, after subduction of oceanic plate, there happens to be necking in the ocean-continent transition zone. After some time, the continental lithosphere is detached from the oceanic plate and buried crustal rocks are exhumed to the surface as a coherent block due to force release and buoyancy of these rocks compared to their surroundings. Although this process has been interpreted in the context of oceanic plate subduction, it is also possible that in intra-plate regions, mostly in post-collision scheme, continental subduction being driven by convergence, can also initiate some instability in the lithospheric mantle [44,45]. The accumulation of viscous lithospheric mantle can drip down into the mantle as a massive block. This process is also interpreted in the context of slab breakoff, because the lithospheric mantle detaches from the upper parts after some necking driven by negative buoyancy of the accumulated viscous block.

This mechanism has been proposed for UHP terrane in Western Gneiss region [45], HP-HT metamorphics of Menderes Massif in Western Turkey [46], and UHP terrane in Dabie-Shan region of Eastern China [44].

1.2.3. Subduction Channel Flow

Subduction channel flow is a widely accepted mechanism for continuous and/or polyphase exhumation of crustal rocks in Dabie-Sulu region of Eastern China [40]. The subduction of oceanic or continental block, oceanic and/or continental crustal rocks are buried along a V shaped subduction channel in which they are circulated like a washing-machine (personal communication with Prof. Bradley Hacker) and then exhume back to the pro- or retro-side. According to Warren et al., (2008), [35] the tip of the subduction channel is named control point. Despite some differences on the names given to this process (Plunger expulsion, cavity-driven flow, wedge flow), the subduction channel is mostly not exposed to asthenospheric flow, otherwise delamination might be favored in later stages of the process.

This model was proposed for the formation and exhumation of metamorphics in Kaghan, Tso Morari, Western Gneiss Region and Dora Maira Massif in Warren et al., (2008) [35]. The polyphase exhumation of metamorphic rocks were interpreted as a result of subduction channel process along with tectonic underplating and sublithospheric plume idea applied to Dabie-Sulu region in Eastern China in Li and Gerya, (2009) [40].

1.2.4. Slab Rollback

Slab Rollback mechanism is introduced in the context of microplate (small continental lithosphere blocks) subduction. It is proposed that subduction of these blocks might trigger the slab rollback, creating the required space for the exhumation of the buoyant continental crust that was deeply buried just before. The crust is then exhumed at a rate that depends directly on the velocity of trench retreat to become part of the overriding plate. Asthenospheric flow initiates a second phase of the exhumation which should be at a lower rate than before. The burial and exhumation process happens whenever a small continental block subducts [36].

This model has been proposed for Aegean type HP metamorphism and exhumation in the works of Brun and Faccenna, (2008) [36] , Jolivet and Brun, (2008) [47] , Gessner et al., (2013) [48] and Tirel et al., (2013) [49].

1.2.5. Delamination

Delamination is the process in which lithospheric mantle decouples from the crust. This might happen when sufficient amount of asthenospheric mantle intrudes into the upper levels and channeled through the lower crust. Based on the rheology models of crust and the beneath, [19, 50] strength of the crust decreases exponentially from upper crust to Moho depths. This drop in strength is interpreted as a change in deformation style from brittle to viscous. A lower crust deforming mostly in viscous regime can decouple from the lithospheric mantle beneath when it is exposed a hot, or pressurized fluid, or when the strain rate ratio of lower crust and the lithospheric

mantle is significant.

Delamination model has been proposed for exhumation of metamorphics in Western Gneiss Region by Duretz et al., (2013) [38]. The early interpretation of this model was explained by Peter Bird for the formation of Colorado Plateau [51]. Later works make use of this model to explain the lack of mantle lithosphere beneath the continental crust and migration of melts in the direction of delaminating slab in Eastern Anatolia [52].

1.3. Geological Setting of Afyon and Tavşanlı Zone

The general tectonic structure of the Western and Central Turkey is shown in Figure 1.5.

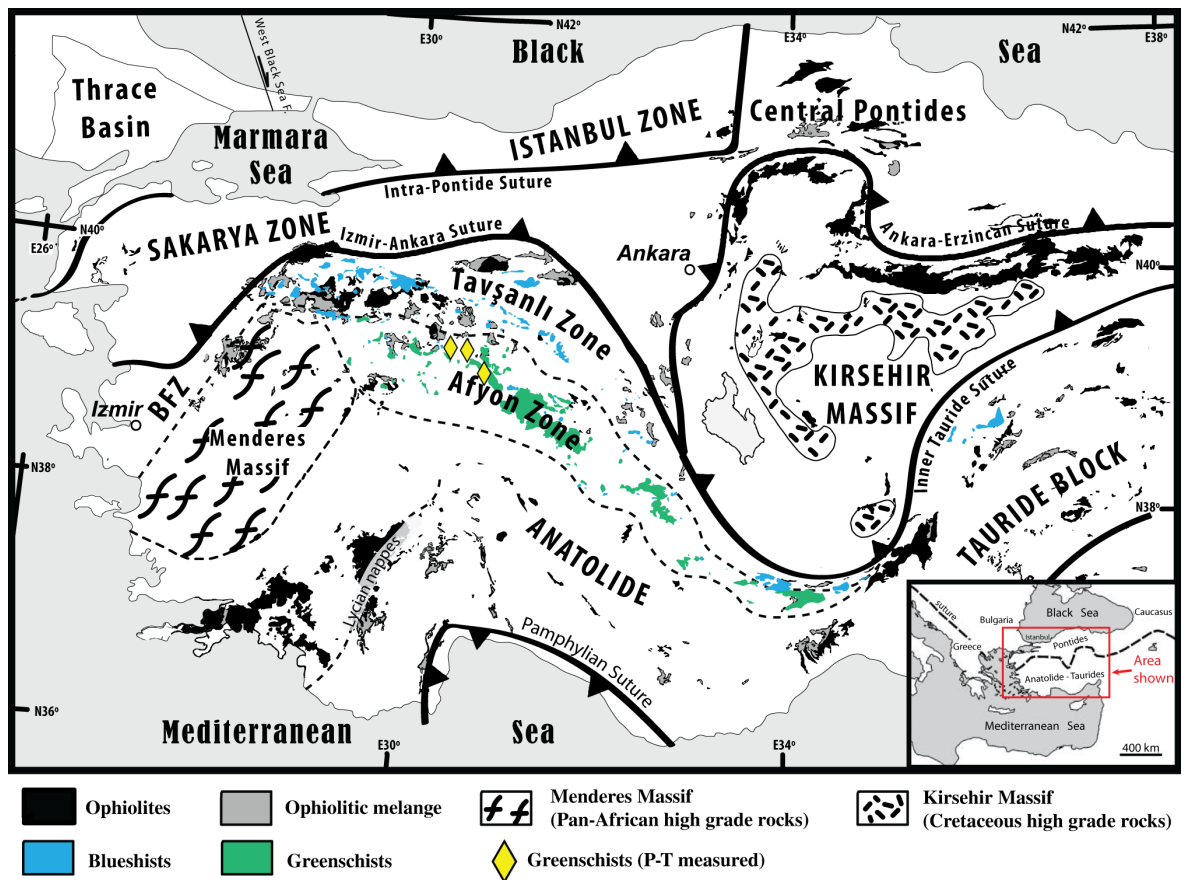


Figure 1.5. Tectonic and geological Map of Western and Central Turkey. (Modified from Okay and Tüysüz, (1999); [15] Pourteau et al., (2010) [16])

During the Alpidic orogeny in the Early Tertiary, the continent-continent collision united several continental fragments with individual structural, stratigraphic and metamorphic units [53]. A well exposed Izmir-Ankara-Erzincan suture along which the Tethyan ocean was consumed separates the Laurasian units to the north from Gondwanian units to the south.

To the south of Izmir-Ankara suture, Tavsanlı Zone forms a 50 km wide coherent blueschist belt, indicating the northward subducted passive continental margin of the Anatolide-Tauride platform [29]. Its western margin is in contact with Bornova Flysch Zone (BFZ) which is a latest Cretaceous-Paleocene flysch zone containing Mesozoic limestone blocks, several kilometers large, in a Maastrichtian-Paleocene greywacke-shale matrix [54].

To the farther south, situated in one of the united distinctive fragments, Afyon Zone is a Devonian to Paleocene sedimentary sequence metamorphosed in greenschist facies. It is a typical shelf-type Palaeozoic-Mesozoic sequence of the Taurides [55]. This region is characterized by low grade regional metamorphism, and its structural setting marks Afyon Zone as a strong member of Anatolides [29, 56].

1.3.1. Spatial Distribution of Metamorphic Units and P-T Conditions

The blueschists in the north-west of the Orhaneli area (north-west of Tavsanlı Zone) make up a regionally metamorphosed clastic-limestone sequence overlain tectonically by an accretionary complex and a peridotite slab. The base of the blueschists is not exposed. The blueschists are intruded by Eocene granodiorite plutons and are unconformably overlain by Miocene continental deposits [29].

From the north to the south, Anatolides consist of regions with decreasing metamorphic pressure and temperature. The presence of jadeite, glaucophane and lawsonite in the blueschists in the Orhaneli area provides P-T conditions of 20 ± 2 kbar and 430 ± 30 °C [57]. The P-T conditions were later modified to 24 ± 3 kbar and 430 ± 30 °C [4]. Based on carpholite-bearing assemblages, P-T conditions on the greenschists

were estimated as minimum 6-9 kbar and 350 °C in Afyon Zone [5].

1.3.2. Temporal Constraints

Ar/Ar laser probe analyses of the blueschist samples from the Orhaneli area gives a weighted mean age of 87 ± 3 Ma for the age of metamorphism. It is important to note that the data has a variation of 20 Ma and there is no direct evidence for the depositional age of the pre-metamorphic blueschist sequence [29]. The metamorphic rocks from Afyon Zone (Ören - Afyon Zone) was dated to between 70 - 65 Ma [58].

2. EXPERIMENTS AND RESULTS

2.1. Explanation of The Numerical Model

2.1.1. The Principle Equations

We conducted a series of thermo-mechanical numerical experiments with an arbitrary Eulerian-Lagrangian finite element code named SOPALE [59]. This numerical code is useful for observing surface response of tectonic systems and tracking specific particles in order to extract their P-T-t paths [60] in order to compare with natural data.

In experimental sets, we advanced by increasing the complexity of the models by starting from the simplest case. A step by step approach to the problem has given us the opportunity to discuss the effect of many parameters to the system as a whole at the expense of computational time.

By considering the case of incompressible flow, the governing equations for thermo-mechanical computation consist of conservation of mass, momentum and internal energy in 2-D implied as follows:

$$\nabla \cdot (\rho \mathbf{v}) = 0, \quad (2.1)$$

$$\nabla \cdot \sigma_{ij} + \rho g = 0, \quad (2.2)$$

$$\rho c_P \left(\frac{\partial T}{\partial t} + \mathbf{v} \cdot \nabla T \right) = k \nabla^2 T + \rho H, \quad (2.3)$$

The linearized equation of state is also implemented by the equation below:

$$\rho = \rho_0[1 - \alpha(T - T_0)], \quad (2.4)$$

In equations (2.1)-(2.4), ρ , T and v represent density, temperature and velocity fields respectively. Likewise, g , α , c_p , k , H and t are the variables representing gravitational acceleration (m^2/s), thermal expansivity (K^{-1}), heat capacity at constant pressure ($J/kg/K$), thermal conductivity ($W/m/K$), rate of internal heat production per unit mass (W/kg) and time respectively. The stress tensor in equation (2.2) is divided into two components:

$$\sigma_{ij} = \sigma'_{ij} - P\delta_{ij}, \quad (2.5)$$

where σ'_{ij} denote the deviatoric stress tensor and P is the pressure (for an incompressible fluid, $P = -\frac{1}{3}\sigma_{ii}$). It is also important to note that visco-plastic deformation is achieved by determination of the lesser value of either a yield stress σ_{yield} or viscous stress $\sigma_{viscous}$ at each computational node. This enables the material to deform at a stress level lowest possible. This relation can be shown below as follows:

$$\sigma'_{ij} = \min(\sigma_{yield}; \sigma_{viscous}), \quad (2.6)$$

Drucker-Prager yield criterion is used for frictional plastic yield stress which is identical to the Coulomb criterion in plane strain [59]:

$$\sigma_{yield} = P \sin\phi + c_0, \quad (2.7)$$

In equation (2.7) ϕ and c_0 stands for internal angle of friction and cohesion, respectively. The equation for viscous stress is shown below:

$$\sigma_{viscous} = 2\eta_e \dot{\epsilon} \quad (2.8)$$

The effective viscosity η_e for power-law creep is defined as:

$$\eta_e(\dot{\epsilon}, T) = GA^{-\frac{1}{n}} \dot{\epsilon}^{\frac{1-n}{n}} e^{\frac{Q}{nRT}}, \quad (2.9)$$

where

$$G = \left(3^{-\frac{(n+1)}{2n}} 2^{\frac{(1-n)}{n}} \right), \quad (2.10)$$

The variables $\dot{\epsilon}, A, Q, n, R$ represent strain rate, viscosity parameter, activation energy for uniaxial laboratory experiments, power law exponent, and ideal gas constant respectively. G is a constant used for the conversion of the uniaxial laboratory data to a state of stress which is independent of the choice of coordinate system.

2.1.2. Flow Parameters of Materials

The equations given in the previous section are the basic tools to assign any computational node the degree to which that node is supposed to deform. Although the formulas give a sense general principles of the mechanism, it is useful to derive some other relations by using these equations and interpret the results accordingly.

Given the non-linear power law creep, which is stated below:

$$\dot{\epsilon} = A\sigma^n e^{-\frac{Q}{RT}}, \quad (2.11)$$

It can be said that strain rate depends on the temperature of the material, power law exponent, applied stress, material parameter or creep parameter that is denoted as A , and activation energy of the rock. This type of deformation is called stress dependent viscosity, because the stress is directly dependent on strain rate, which in turn is related to viscosity or effective viscosity of the rock. In order to understand the importance of each parameter in these equations, it is useful to compile some of the important material properties from various sources in a short list as follows:

Table 2.1. Flow parameters of major rock types. Compiled from various sources [19–21].

Material	$A(MPa^{-n}s^{-1})$	n	Q(kJ/mol)	Reference
Quartz	1.0×10^{-3}	2	167	1
Plagioclase(An_{75})	3.3×10^{-4}	3.2	238	1
Granite	1.8×10^{-9}	3.2	123	1
Granite (wet)	2.0×10^{-4}	1.9	137	1
Quartzite	6.7×10^{-6}	2.4	156	1
Quartzite (wet)	3.2×10^{-4}	2.3	154	1
Diabase	2.0×10^{-4}	3.4	260	1
Felsic Granulite	8.0×10^{-3}	3.1	243	1
Mafic Granulite	1.4×10^4	4.2	445	1
Peridotite (dry)	2.5×10^4	3.5	532	1
Peridotite (wet)	2.0×10^3	4.0	471	1
Quartzite (wet)	1.1×10^{-4}	4.0	228	2
Aheim Dunite (wet)	4.16×10^2	4.48	498	3

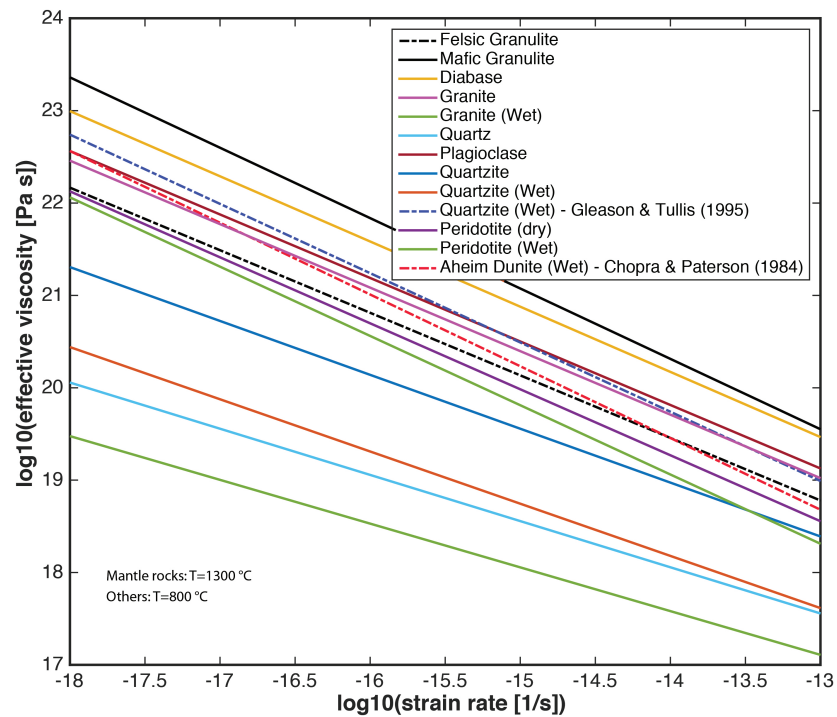


Figure 2.1. Effective viscosity vs. strain rate plot for the materials in Table (1.2).

Reference temperatures are shown on the lower left.

The plot of effective viscosity vs. strain rate is very informative when comparing their tendency to deform in various environments. At a given temperature and strain rate, we can compare their rate of flow by looking at their effective viscosity. Lesser value of viscosity means higher rate of flow or deformation. It can be seen from Figure (2.1) that mafic granulite is the least deforming rock among all the rocks at a given temperature and strain rate. The highest deforming rock is peridotite wet by having an effective viscosity about 10^{18} Pa s at a strain rate of $10^{-15} s^{-1}$.

The temperature of the mantle rocks of Peridotite, Peridotite (wet), Aheim Dunite (wet), were taken as 1300 °C in order to compare their rate of deformation in the mantle depths. Other rocks were based on a general granulite facies temperature corresponding to Moho temperatures of relatively hotter continental regions.

2.2. Rheology of Lithosphere

The strength of crust and lithospheric mantle is of crucial importance when dealing with long-term (>1 Myr) evolution and dynamics of earth processes. The concept of a strong lithosphere overlying a weak fluid asthenosphere was proposed in early 1900's. [61]. There are two contrasting strength profiles for the continental lithosphere: jelly sandwich and crème brûlée.

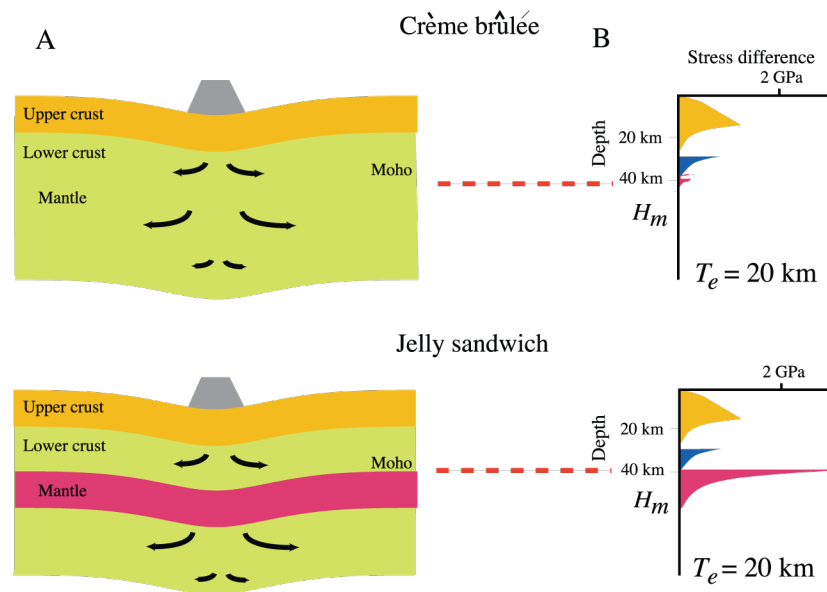


Figure 2.2. A) Models of deformation. B) Brace-Goetze failure envelopes for a thermotectonic age of 150 Ma, a weak, undried granulite lower crust, a uniform strain rate of $10^{-15} s^{-1}$ (Burov and Watts, (2006) [17]).

As it can be seen from Figure (2.2) (schematic diagram illustrating different models for the long-term strength of continental lithosphere) that in the crème brûlée model, the strength is confined to the uppermost brittle layer of the crust, and compensation is achieved mainly by flow in the weak upper mantle (H_m is the short-term mechanical thickness of the lithosphere; T_e is the long-term elastic thickness). In the jelly sandwich model, the mantle is strong and the compensation for surface loads occurs mainly in the underlying asthenosphere. The crème brûlée model was proposed by Jackson, (2002) [62] challenging the idea of jelly-sandwich model. The latter one has been favored, because it was proposed that the crème brûlée model is unable to explain either the persistence of mountain ranges or the integrity of the downgoing slab in collisional systems. Hence, it has been stated that the latter model is a more widely applicable one for many tectonic settings [17].

In this work, both models were tested in the context of continental plate subduction following ocean subduction. This was achieved by setting the deformation type of lithospheric mantle to plastic and viscous (newtonian if $n=1$, affective if $n>1$) rheology. In case of upper crust, the program chooses the lowest stress level to deform, which means that brittle-ductile transition in the lower crust is active in most cases.

2.3. Boundary Conditions

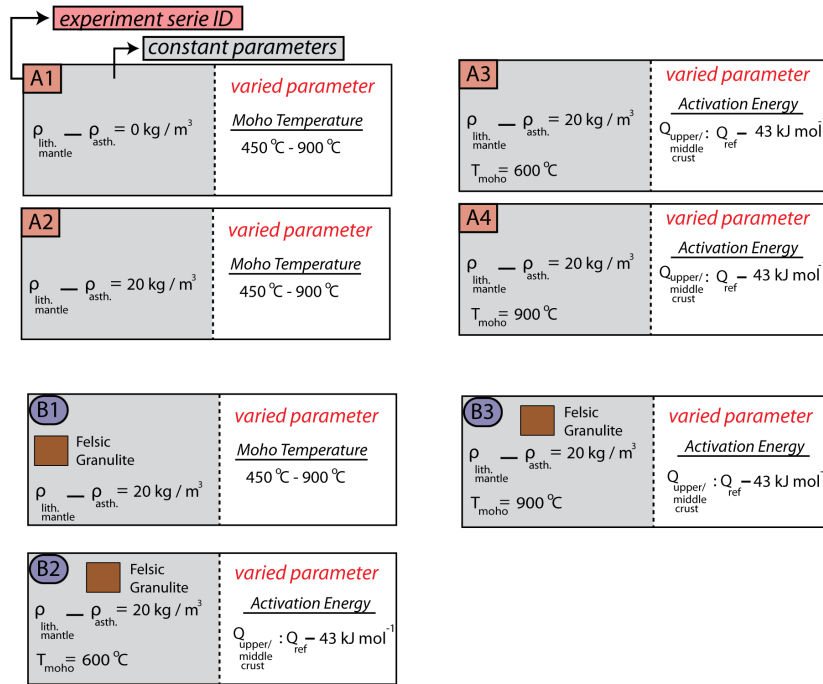
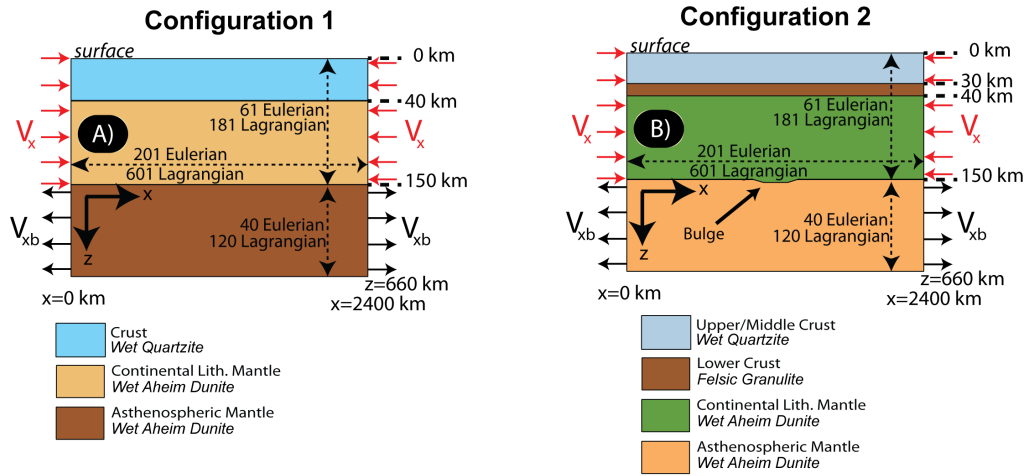


Figure 2.3. Initial model configurations. Each color represent a different layer.

Eulerian and Lagrangian partitioning are shown in the model box.

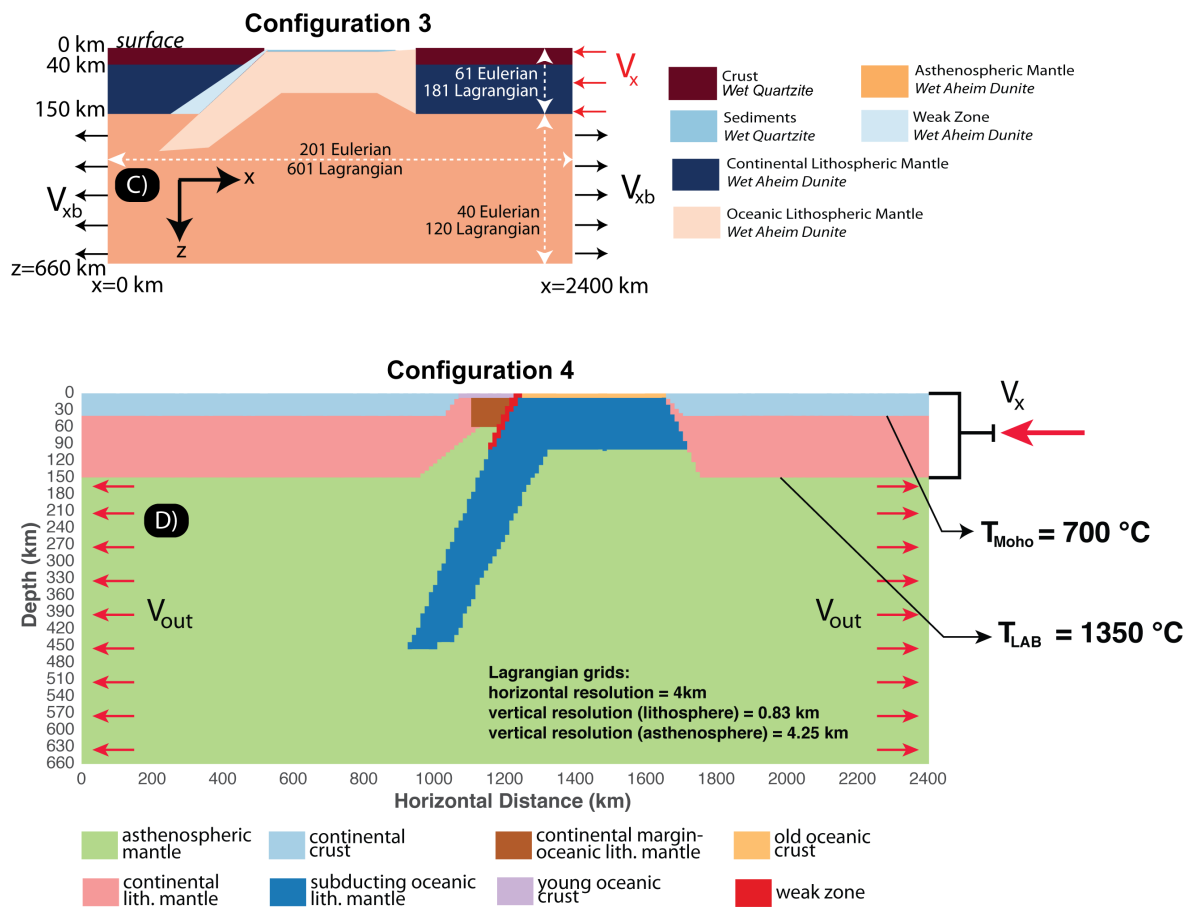


Figure 2.4. C) Oceanic plate subduction model. D) Intra-oceanic subduction model. Each colour represents a different layer. Eulerian and Lagrangian partitioning are shown in the model box.

The numerical experiments can be categorized in two sections. The first set of models were constructed and performed in order to investigate the effect of Rayleigh-Taylor instability on burial and exhumation of crustal rocks in post-collisional setting. This was achieved by starting with the simplest configuration which consisted of a total number of three layers covering crust and upper mantle. The upper mantle consist of two layers named as lithospheric mantle and asthenosphere or sub-lithospheric mantle. The main difference between the lithospheric mantle and asthenosphere is the density, added to which there might also be rheological difference in the sense that lithospheric mantle might deform in plastic rheology whereas asthenospheric mantle might be deforming mostly in viscous regime. Because the rheological behaviour of these layers are highly controversial [63,64], we tried to expand our parameter space as far as possible.

The second set of experiments were designed to observe the subduction dynamics in the context of dripping instability. The viscous or visco-plastic rheology was prescribed in continental lithospheric mantle.

In configuration A, crust of 40 km in thickness with flow parameters of wet quartzite [20], a layer of 110 km in thickness representative of lithospheric mantle with flow parameters of Aheim Dunite (wet) [21], and a hotter layer of 550 km in thickness with the same flow parameters as lithospheric mantle, representative of asthenospheric mantle was prescribed. The imposed convergence velocity was held constant as 3 cm/year from both sides. This convergence velocity was prescribed to the whole lithosphere along with a negative convergence from asthenosphere to the outer region of the box in order to preserve the conservation of mass in our models.

Configuration B has some differences from the previous one in the sense that it starts to evolve with a bulge prescribed in the lithospheric mantle to initiate the drip mechanism. The reasoning behind starting with such a configuration is due to the fact that the thickening in the crust and mantle was not achieved in the center of the domain without imposing a bulge. The other reason was that it is appropriate to make the assumption that there might have been a non-uniform region in the lithospheric mantle which is possible in the context of post-collision. However, it is also safe to assume that the perturbation at an appropriate wavelength might have been sufficient to initiate the Rayleigh-Taylor instability in configuration B.

The next configuration (C) was arranged to compare the post-collision scheme with subduction dynamics. A pre-existing oceanic lithosphere was introduced between two continental plates of same rheology. A weak zone between the oceanic plate and retro-plate and a very thin layer of sediments were prescribed and added to the model geometry.

The last configuration (D) simulates an intra-oceanic subduction system. It was based on a proposed model in the literature [29]. This configuration includes more layers than the previous ones, which makes it more complicated one indeed.

The solution space had a free top surface and free slip conditions on the right, but no slip condition on the left boundary. Material was not permitted to penetrate the lower boundary of the box. This arrangement was not highly restrictive in the sense that the influence of the bottom boundary had not a significant effect on the deformation of the lithosphere.

Eulerian and lagrangian grids were limited to 201x101 and 601x301 respectively. These numbers represent the resolution of the deformation in our models. It is important to note that more than half of the eulerian grids and 60% of the lagrangian grids were concentrated in the lithosphere to increase the resolution in the upper parts of the numerical model.

The initial temperature profiles were arranged to comply with the values in nature and be more representative. For all experiments, the temperature of the lithosphere-asthenosphere boundary (LAB) and lower boundary of the box was set as 1350 °C [64, 65] and 1525 °C ,respectively. Thermal properties (thermal conductivity $k=2.25$ W/m/K, heat capacity $c_P = 1250$ J/kg/K) are the same for all materials and we ignored radioactive heat production and shear heating and erosion in the numerical models.

The viscosities was kept in the range of 5×10^{19} Pa s - 10^{22} Pa s. At a specific node of computation, if the deformation in that region is below or higher than the allowed viscosity range, then the effective viscosity of that material is set as the lowest or highest one to provide continuous deformation in the allowed range.

2.4. Post-collision

2.4.1. Experimental Set A1

In experimental set A1, we started with the simplest case which consisted of 3 layers: crust, lithospheric mantle and sub-lithospheric mantle (asthenosphere). Moho temperature was increased starting from 450 °C with 150 °C increments up to 900 °C. The temperature at lithosphere-asthenosphere boundary (LAB) was set as 1350 °C. The lower boundary of the box had an initial temperature of 1575 °C. The densities of crust, lithospheric mantle and asthenospheric mantle were set as 2800 kg/m^3 , 3300 kg/m^3 and 3300 kg/m^3 respectively. The deformation in the upper crust is visco-plastic, in other words, the numerical code chooses the possible lowest stress level (viscous or plastic) throughout the crust. The same type of deformation was prescribed for the mantle as well.

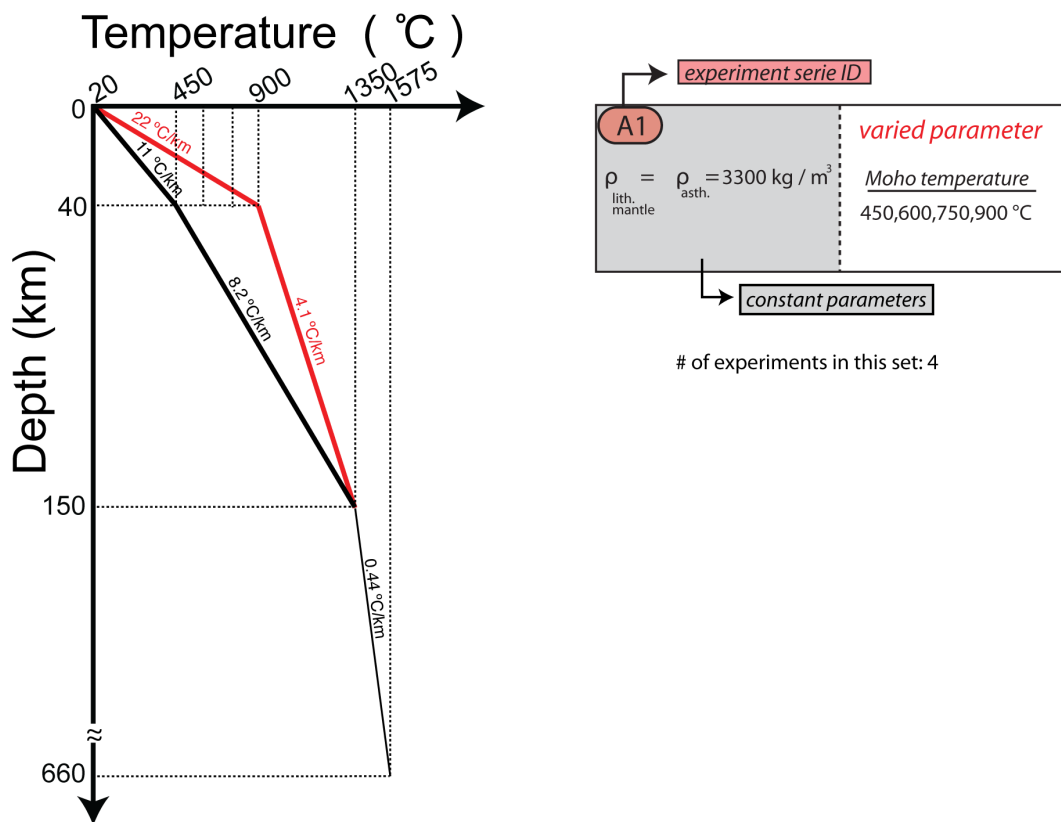
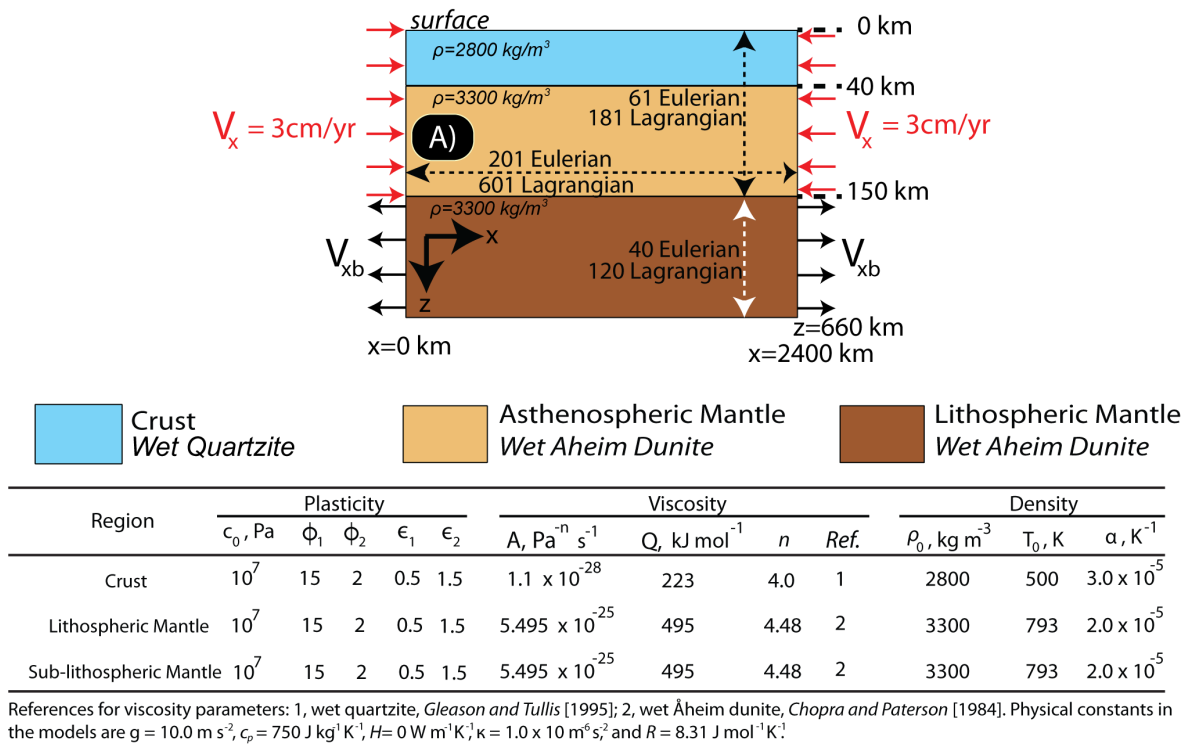


Figure 2.5. Model configuration and flow parameters for the materials of experimental set A1.

2.4.2. Results of A1

When the Moho temperature was set as 450 °C, as it can be seen from Fig. 2.6 that two synchronous drips develop at both boundaries. The root of the drip does not reach above the 120 km depth. The crust is in the process of thickening. The lithostatic pressure of rocks tracked from middle crust increase about half kilobar. After 12.8 Ma, the number of drips increase by initiating another one from the centre of the model domain, because the drips on the sides can not respond well enough to the thickening and the stress is accumulated in the centre. The pressure values of rocks reach to 6 kbar by increasing 1 kbar. No exhumation is observed, because the drip mechanism does not have significant effect to the upper levels.

If the Moho temperature is increased to 600 °C, though similar type of drips develop, the root of them reach higher than the previous case (100 km). After 12.8 Ma, the crust continues to thickening and the thickness of the lithosphere reaches about 180 km depth in the centre of the model domain. The pressure of rocks increase by about 1kbar and there is no increase in temperature values. No exhumation is observed.

Increasing the Moho temperature to 750 °C provides a similar increase in the root of the drips at sides of the model domain (35 km). The drip rate is faster than the previous cases by reaching to depth of 500 km in 6.4 Ma (drip rate is about 5.47 cm/yr). After 12.8 Ma, the thickness of the lithosphere is about the same as it was at the beginning of the numerical model (t=0 Ma). The thickness of the lithosphere decreases to about 90 km at sides. It can be said that the drip rate is close enough to the total convergence and this provides not a third drip in the lithospheric mantle that is observed in the previous cases. The pressure of the rocks increase about 1 kbar and the temperature does not change much.

When the Moho temperature is set to 900 °C, which is the highest level in this experimental set (upper boundary for granulite facies rocks that might exist in lower crustal levels), the drips evolve with higher rate (about 7.03 cm/yr) and higher amount. The root of the drip reaches to middle crust level. Interestingly, after 12.8 Ma, the

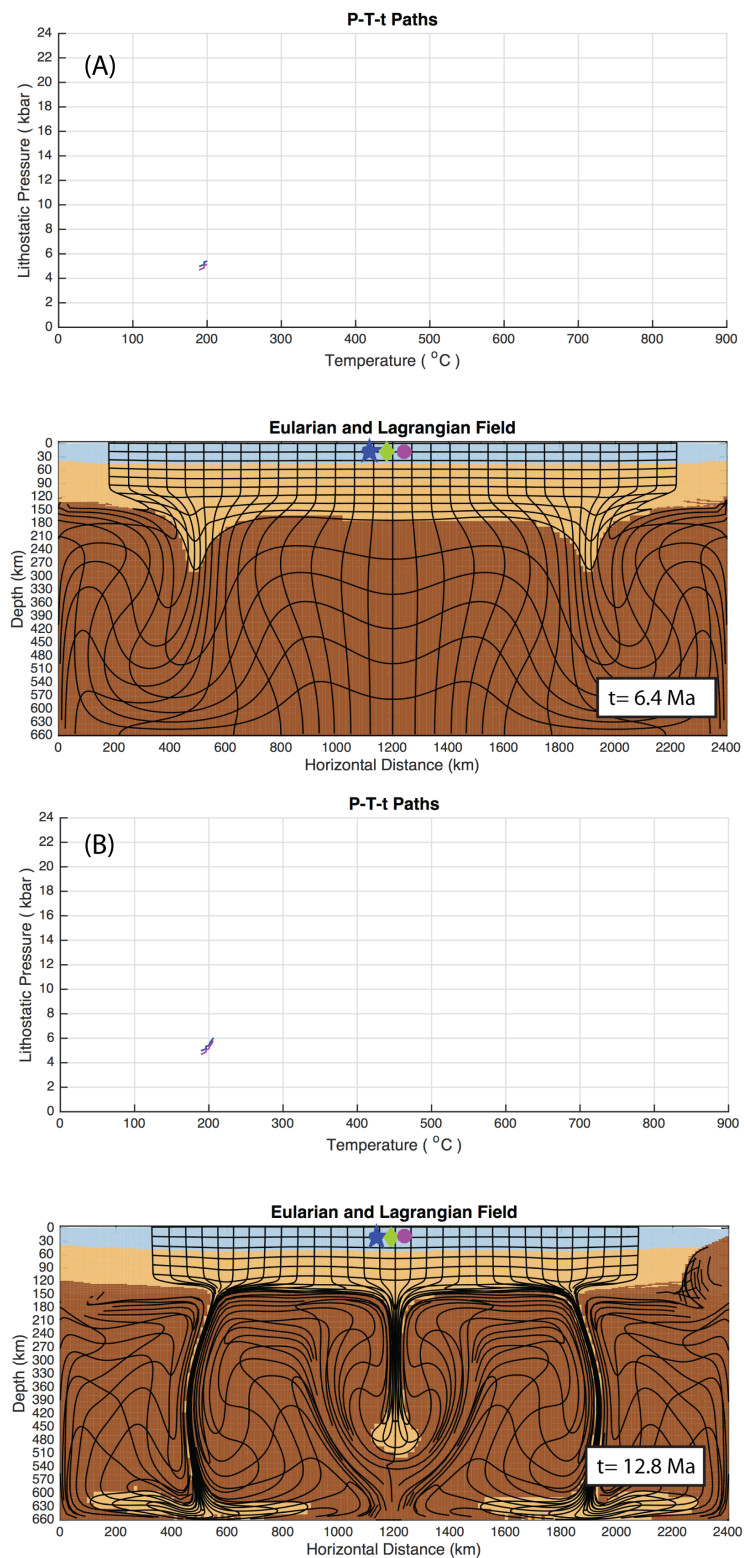


Figure 2.6. Model development and P-T-t paths of tracked particles of experiment A1 with Moho temperature of 450°C (A) after 6.4 Ma, (B) after 12.8 Ma. Blue: crust, Orange: lithospheric mantle, Brown: asthenosphere.

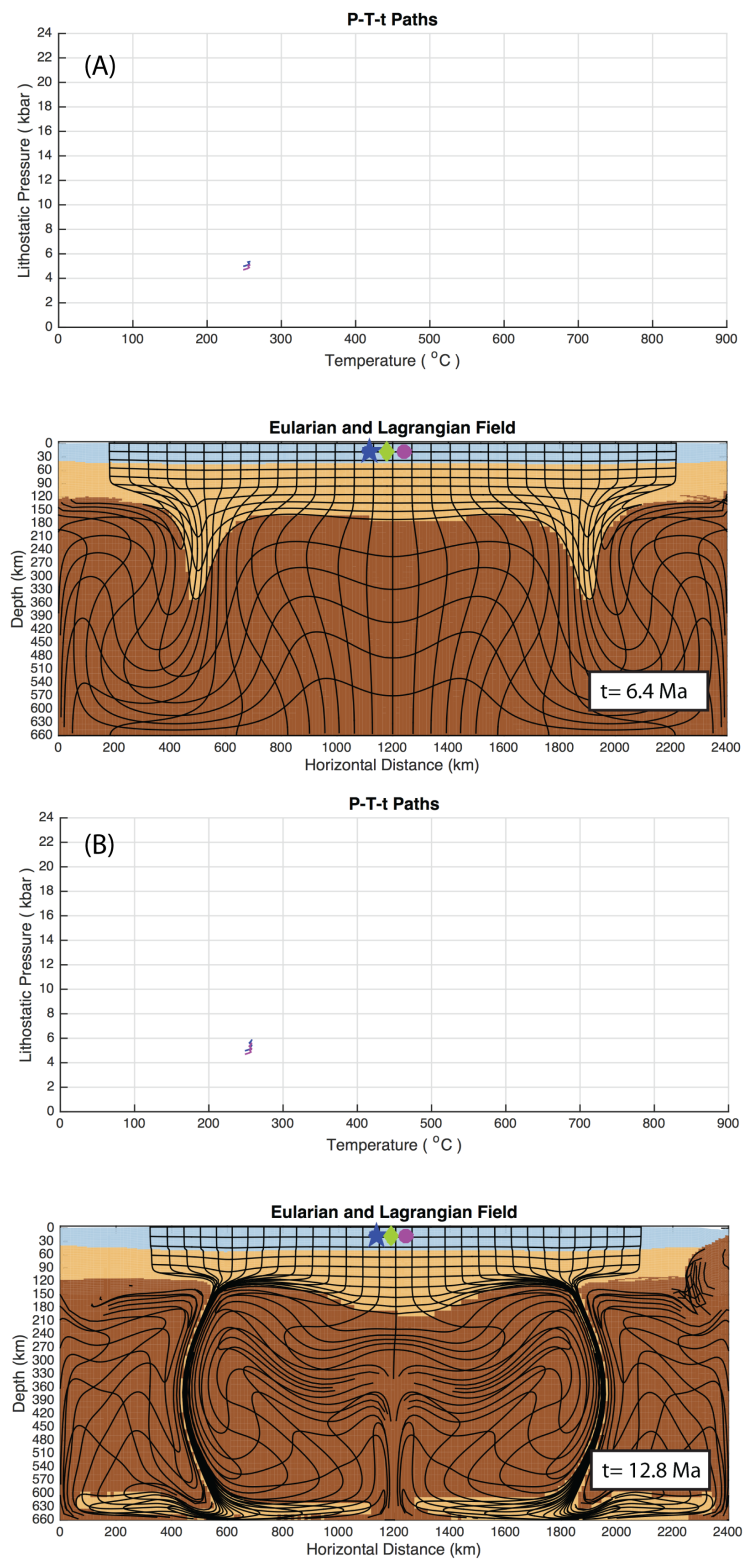


Figure 2.7. Model development and P-T-t paths of tracked particles of experiment A1 with Moho temperature of 600°C (A) after 6.4 Ma, (B) after 12.8 Ma. Blue: crust, Orange: lithospheric mantle, Brown: asthenosphere.

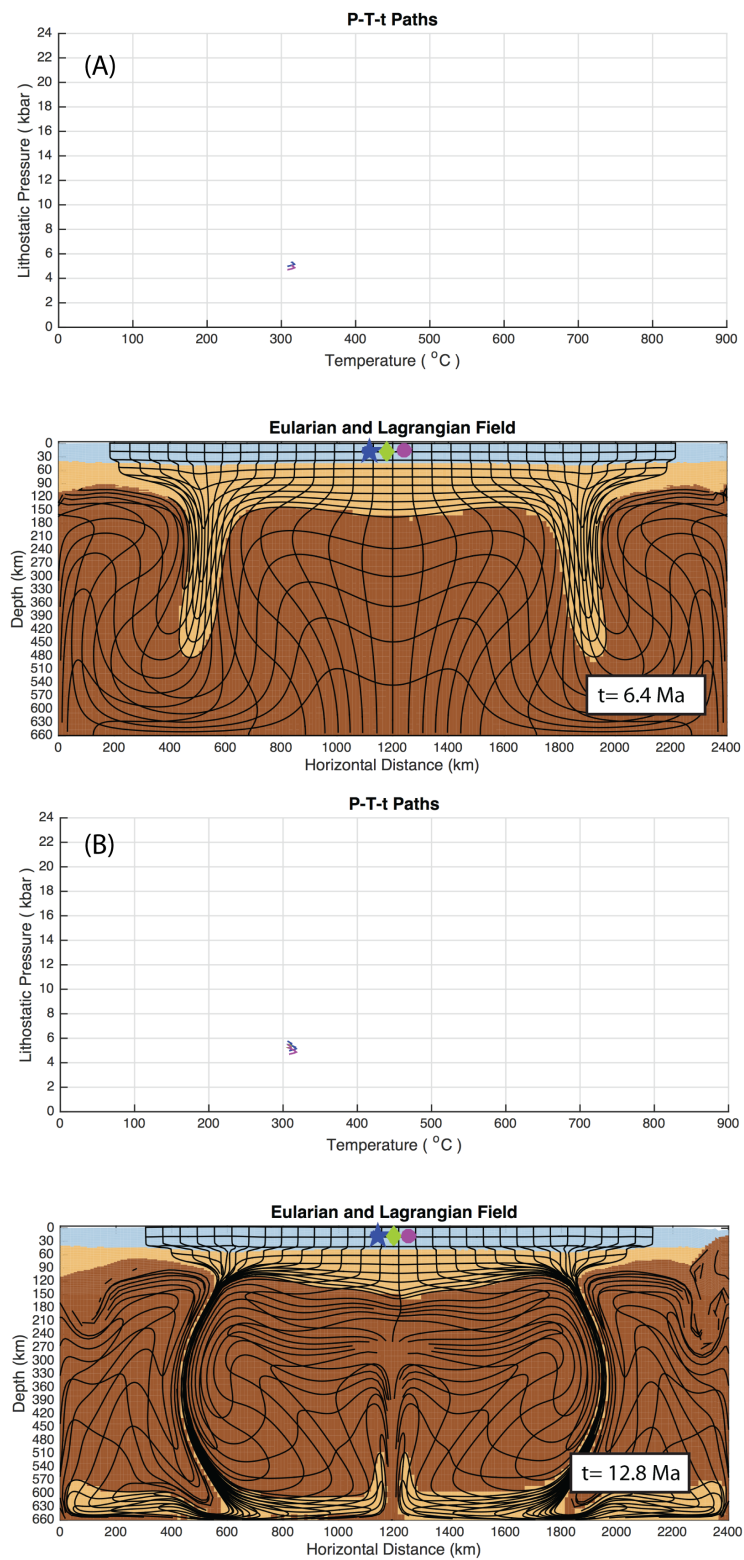


Figure 2.8. Model development and P-T-t paths of tracked particles of experiment A1 with Moho temperature of 750°C (A) after 6.4 Ma, (B) after 12.8 Ma. Blue: crust, Orange: lithospheric mantle, Brown: asthenosphere.

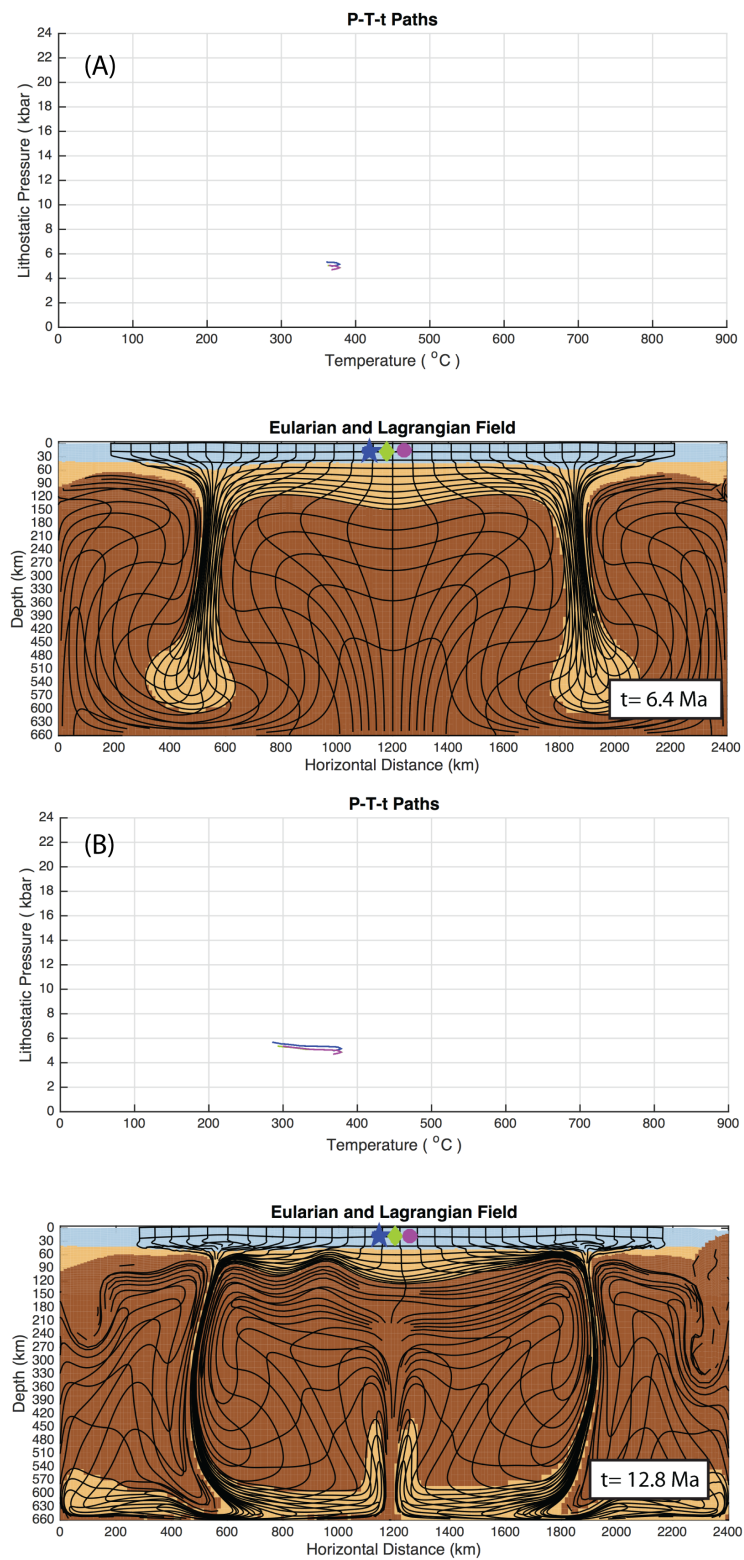
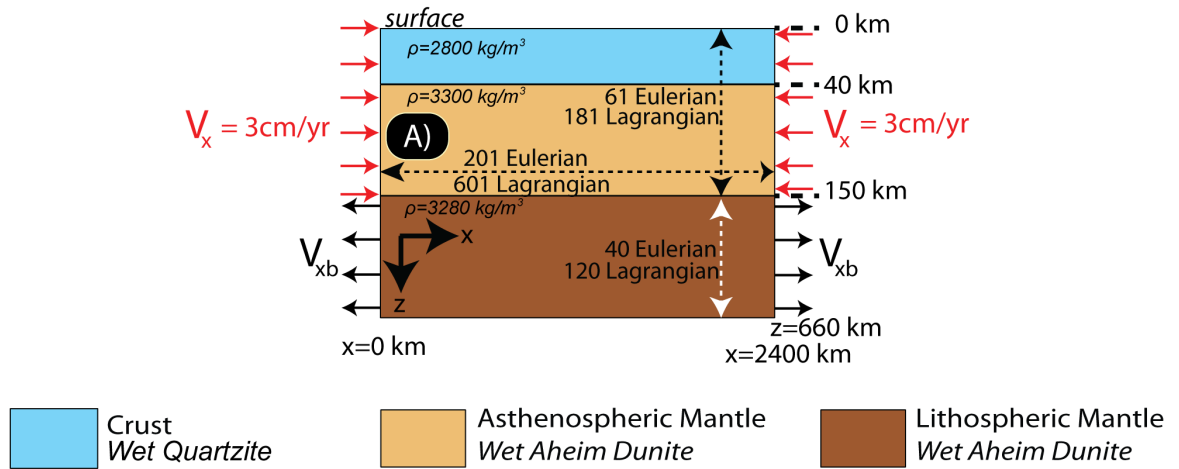


Figure 2.9. Model development and P-T-t paths of tracked particles of experiment A1 with Moho temperature of 900°C (A) after 6.4 Ma, (B) after 12.8 Ma. Blue: crust, Orange: lithospheric mantle, Brown: asthenosphere.

rocks cool about 60 °C and their pressures increase about 1 kbar . One explanation for the cooling is that the geotherm for this model is the steepest one, and this provides rapid changes in temperature when the depth of rock changes. The thickness of the lithosphere decreases to about 110 km in the centre and 60 km at sides of the model domain. Similarly, no exhumation is observed in this model.

2.4.3. Experimental Set A2

In experimental set A2, the same type of configuration was preserved except a density difference between lithospheric mantle and sub-lithospheric mantle is prescribed. Moho temperature was increased starting from 450 °C with 150 °C increments up to 900 °C. The temperature at lithosphere-asthenosphere boundary (LAB) was set as 1350 °C. The lower boundary of the box had an initial temperature of 1575 °C. The densities of crust , lithospheric mantle and asthenospheric mantle were set as 2800 kg/m^3 , 3300 kg/m^3 and 3280 kg/m^3 respectively. The deformation in the upper crust is visco-plastic, in other words, the numerical code chooses the possible lowest stress level (viscous or plastic) throughout the crust. The same type of deformation was prescribed for the mantle as well.



Region	Plasticity					Viscosity				Density		
	c_0, Pa	Φ_1	Φ_2	ϵ_1	ϵ_2	$A, \text{Pa}^{-n} \text{s}^{-1}$	$Q, \text{kJ mol}^{-1}$	n	Ref.	$\rho_0, \text{kg m}^{-3}$	T_0, K	α, K^{-1}
Crust	10^7	15	2	0.5	1.5	1.1×10^{-28}	223	4.0	1	2800	500	3.0×10^{-5}
Lithospheric Mantle	10^7	15	2	0.5	1.5	5.495×10^{-25}	495	4.48	2	3300	793	2.0×10^{-5}
Sub-lithospheric Mantle	10^7	15	2	0.5	1.5	5.495×10^{-25}	495	4.48	2	3280	793	2.0×10^{-5}

References for viscosity parameters: 1, wet quartzite, *Gleason and Tullis* [1995]; 2, wet Aheim dunite, *Chopra and Paterson* [1984]. Physical constants in the models are $g = 10.0 \text{ m s}^{-2}$, $c_p = 750 \text{ J kg}^{-1} \text{ K}^{-1}$, $H = 0 \text{ W m}^{-1} \text{ K}^{-1}$, $\kappa = 1.0 \times 10^{-6} \text{ s}^{-2}$ and $R = 8.31 \text{ J mol}^{-1} \text{ K}^{-1}$.

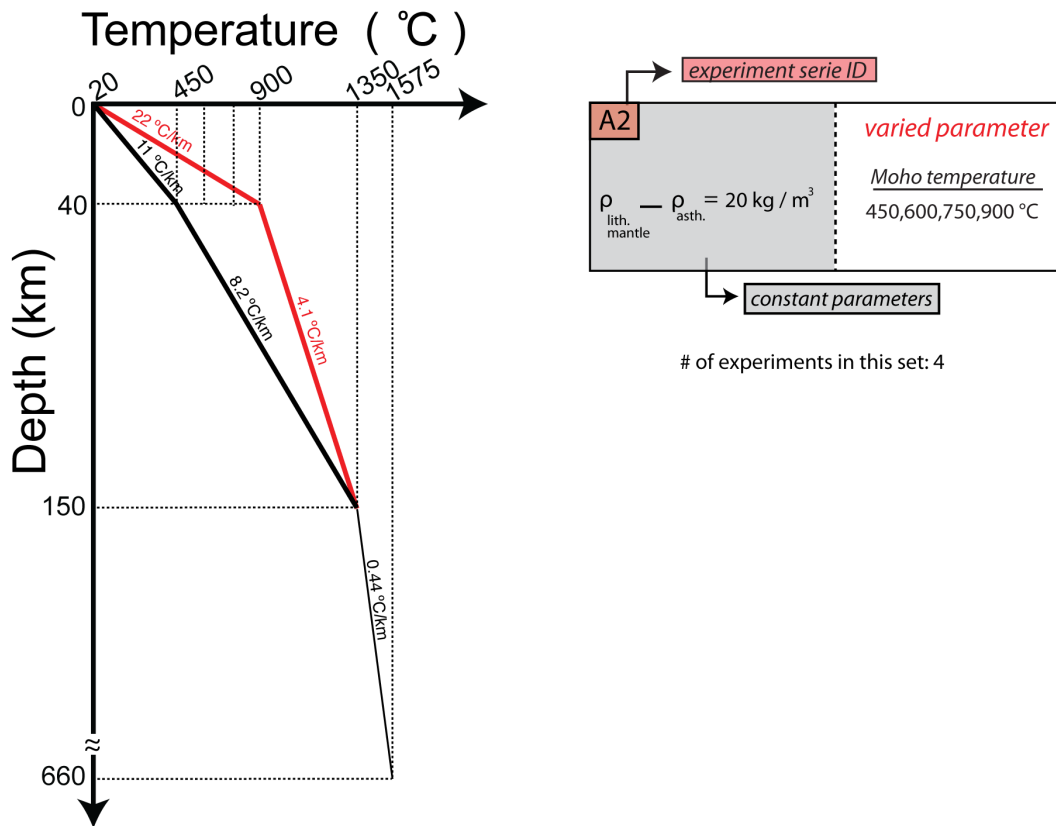


Figure 2.10. Model configuration and flow parameters for the materials of experimental set A2.

2.4.4. Results of A2

When the Moho temperature is set as 450 °C, the similar type of drips with Figure 2.6, but the drips are not evolved as a unified structure, because the density difference between lithospheric mantle and asthenosphere adds extra downward force. This force is well exposed when any part of lithospheric mantle is disturbed by convergence. As it can be seen that, the density contrast increased the drip rate as well. After 12.8 Ma, multiple non-uniform, random drips evolve and reach the bottom. The pressure of rocks from middle crust increase about 1 kbar and there is significant change in temperature. At that stage, the thickness of lithosphere is about 130 km at sides. No exhumation is observed.

If we increase the Moho temperature to 600 °C, the drips reach to the bottom level before 6.4 Ma. The non-uniform drips are well observed. After 12.8 Ma, the pressure of rocks increase about 1 kbar and there is no significant change of temperature. The thickness of lithosphere is about 120 km at sides. No exhumation is observed.

Increasing the Moho temperature to 750 °C promotes the drip rate and amount. After about 12.8 Ma, much of the lithospheric mantle drips down into the asthenosphere. The pressure values of rocks increase by about 1kbar, and the rocks cool about 25 °C. No exhumation is observed.

When the Moho temperature is set to 900 °C, the drips evolve more coherently than the previous cases. The rapid drips affect the lower crust levels. After 12.8 Ma, the pressure values of rocks increase by 1 kbar and the temperature decrease about 60 °C. No exhumation is observed.

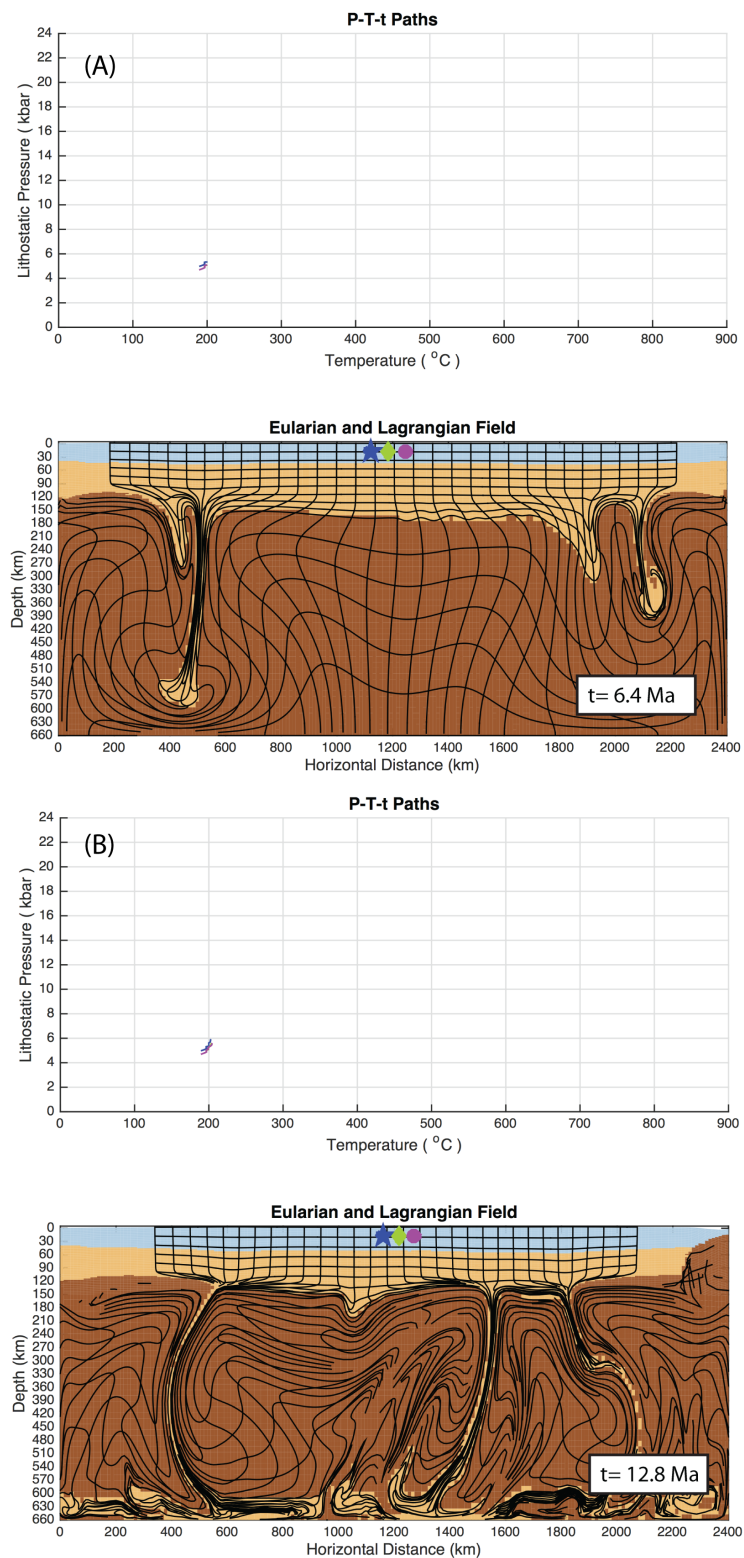


Figure 2.11. Model development and P-T-t paths of tracked particles of experiment A2 with Moho temperature of 450°C (A) after 6.4 Ma, (B) after 12.8 Ma. Blue: crust, Orange: lithospheric mantle, Brown: asthenosphere.

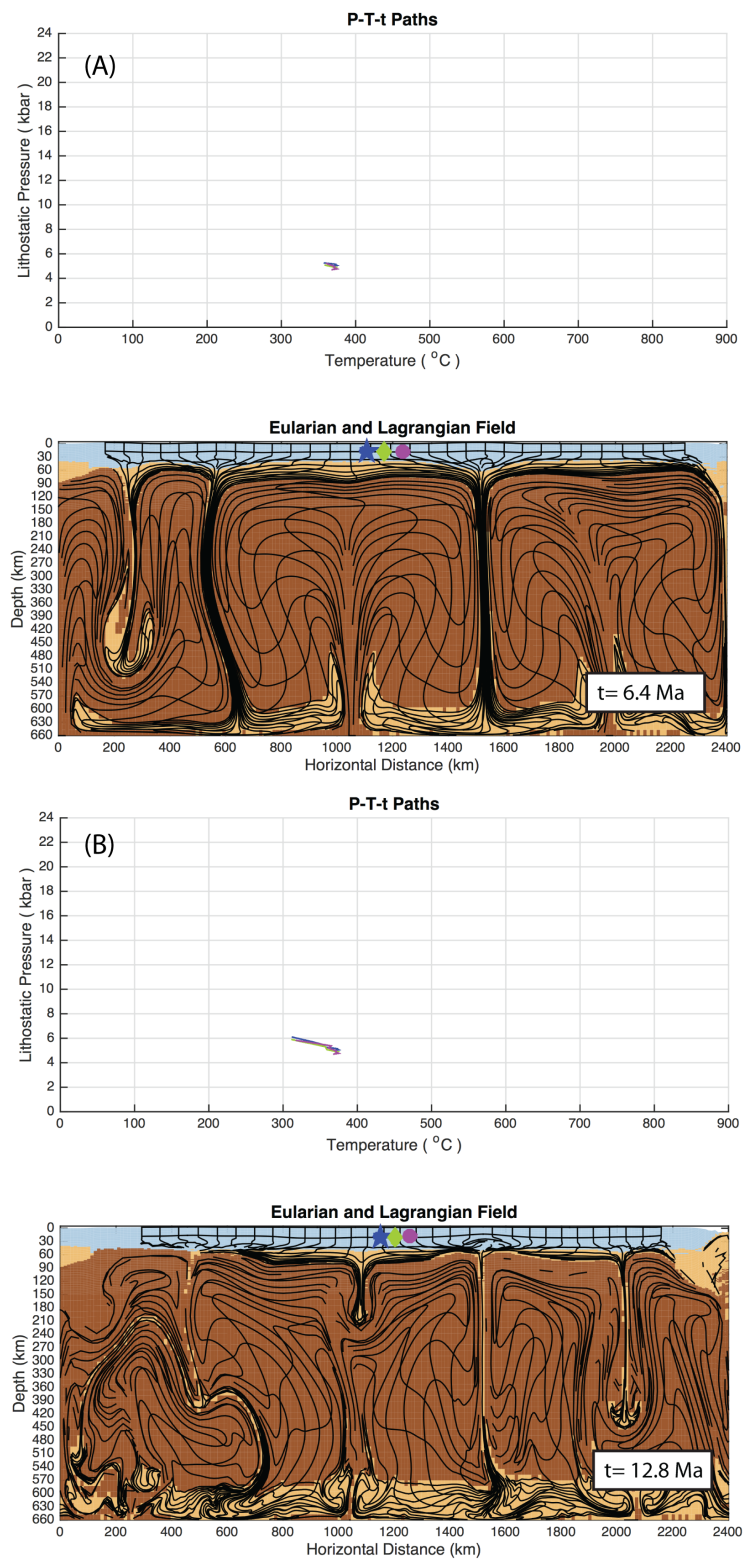


Figure 2.12. Model development and P-T-t paths of tracked particles of experiment A2 with Moho temperature of 600°C (A) after 6.4 Ma, (B) after 12.8 Ma. Blue: crust, Orange: lithospheric mantle, Brown: asthenosphere.

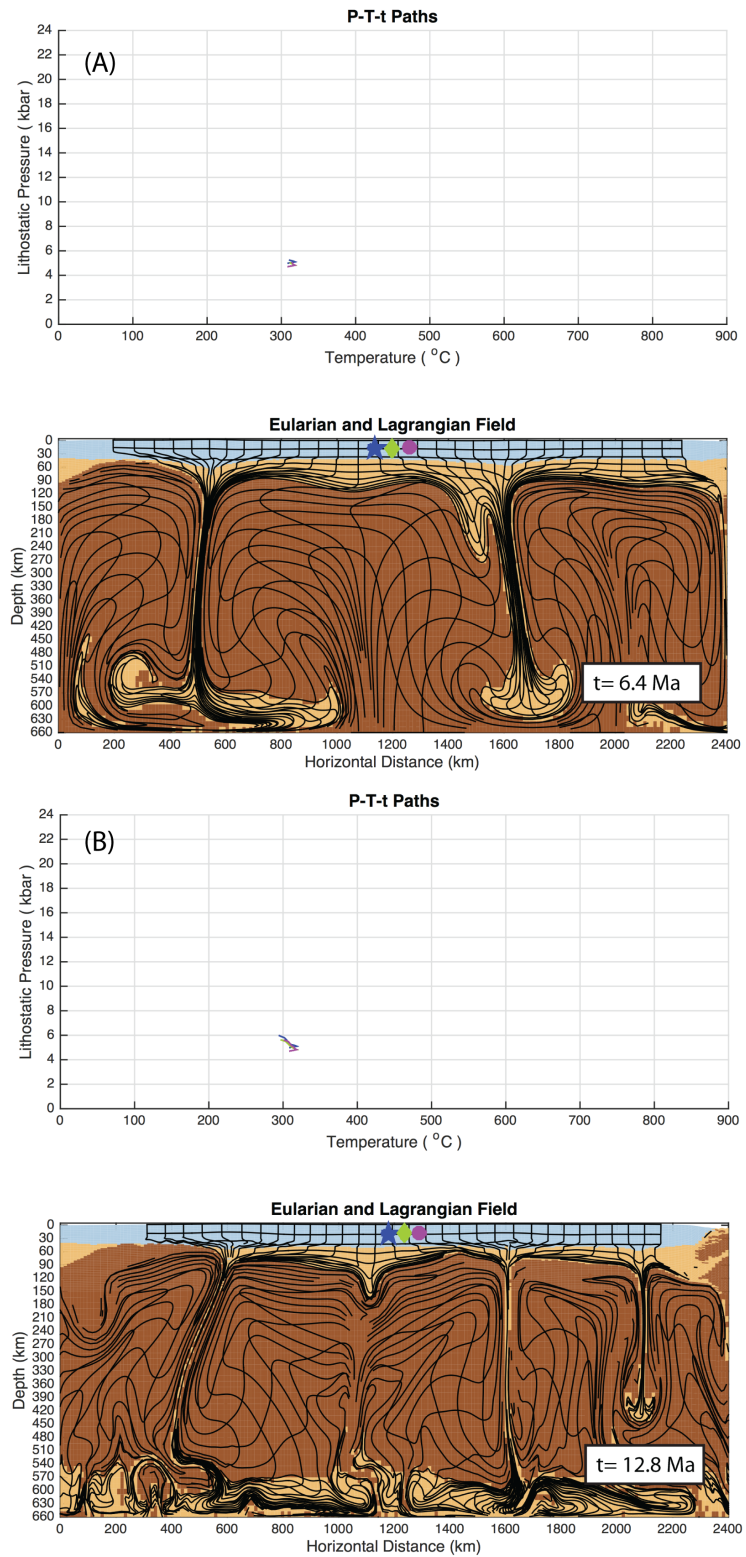


Figure 2.13. Model development and P-T-t paths of tracked particles of experiment A2 with Moho temperature of 750°C (A) after 6.4 Ma, (B) after 12.8 Ma. Blue: crust, Orange: lithospheric mantle, Brown: asthenosphere.

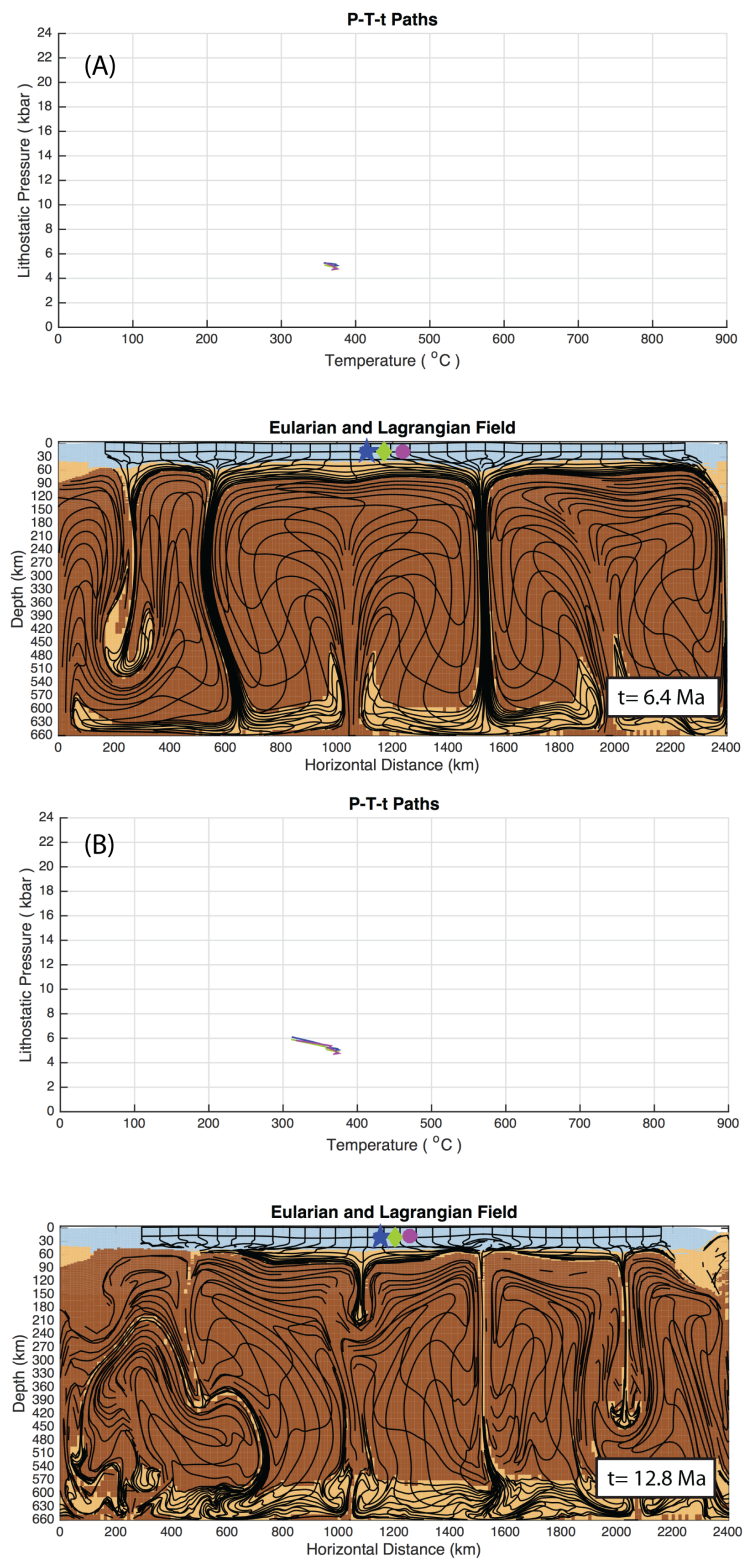
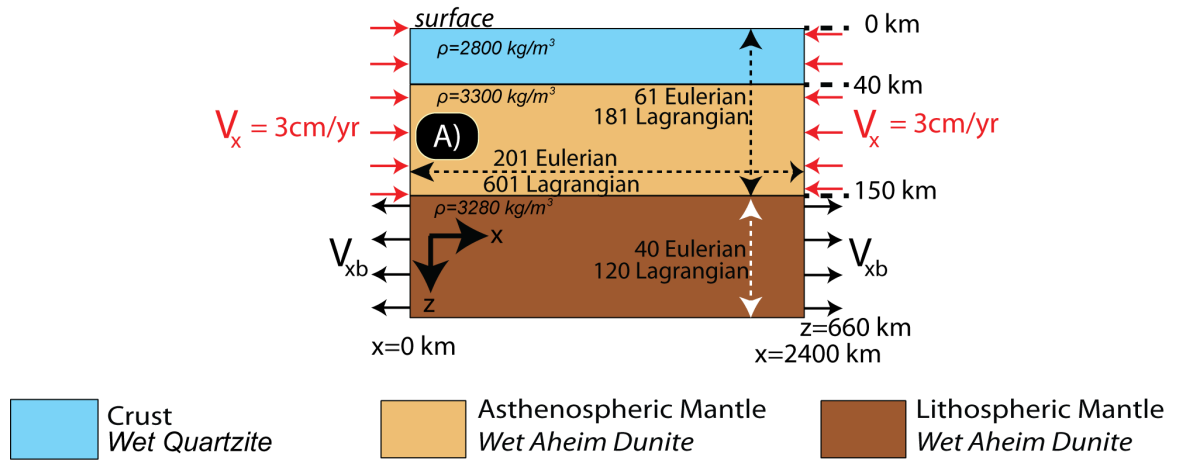


Figure 2.14. Model development and P-T-t paths of tracked particles of experiment A2 with Moho temperature of 900°C (A) after 6.4 Ma, (B) after 12.8 Ma. Blue: crust, Orange: lithospheric mantle, Brown: asthenosphere.

2.4.5. Experimental Set A3

In experimental set A3, the same type of configuration was preserved with the same density difference between lithospheric mantle and sub-lithospheric mantle. Moho temperature was kept constant at 600 °C. The activation energy of crust was decreased from 223 kJ/mol to 133 kJ/mol and 43 kJ/mol. The temperature at lithosphere-asthenosphere boundary (LAB) was set as 1350 °C. The lower boundary of the box had an initial temperature of 1575 °C. The densities of crust, lithospheric mantle and asthenospheric mantle were set as 2800 kg/m^3 , 3300 kg/m^3 and 3280 kg/m^3 respectively. The deformation in the upper crust is visco-plastic, in other words, the numerical code chooses the possible lowest stress level (viscous or plastic) throughout the crust. The same type of deformation was prescribed for the mantle as well.



Region	Plasticity					Viscosity				Density		
	c_0, Pa	ϕ_1	ϕ_2	ϵ_1	ϵ_2	$A, \text{Pa}^{-n} \text{s}^{-1}$	$Q, \text{kJ mol}^{-1}$	n	Ref.	$\rho_0, \text{kg m}^{-3}$	T_0, K	α, K^{-1}
Crust	10^7	15	2	0.5	1.5	1.1×10^{-28}	223	4.0	1	2800	500	3.0×10^{-5}
Lithospheric Mantle	10^7	15	2	0.5	1.5	5.495×10^{-25}	495	4.48	2	3300	793	2.0×10^{-5}
Sub-lithospheric Mantle	10^7	15	2	0.5	1.5	5.495×10^{-25}	495	4.48	2	3280	793	2.0×10^{-5}

References for viscosity parameters: 1, wet quartzite, *Gleason and Tullis* [1995]; 2, wet Aheim dunite, *Chopra and Paterson* [1984]. Physical constants in the models are $g = 10.0 \text{ m s}^{-2}$, $c_p = 750 \text{ J kg}^{-1} \text{ K}^{-1}$, $H = 0 \text{ W m}^{-1} \text{ K}^{-1}$, $\kappa = 1.0 \times 10^{-6} \text{ s}^{-2}$, and $R = 8.31 \text{ J mol}^{-1} \text{ K}^{-1}$.

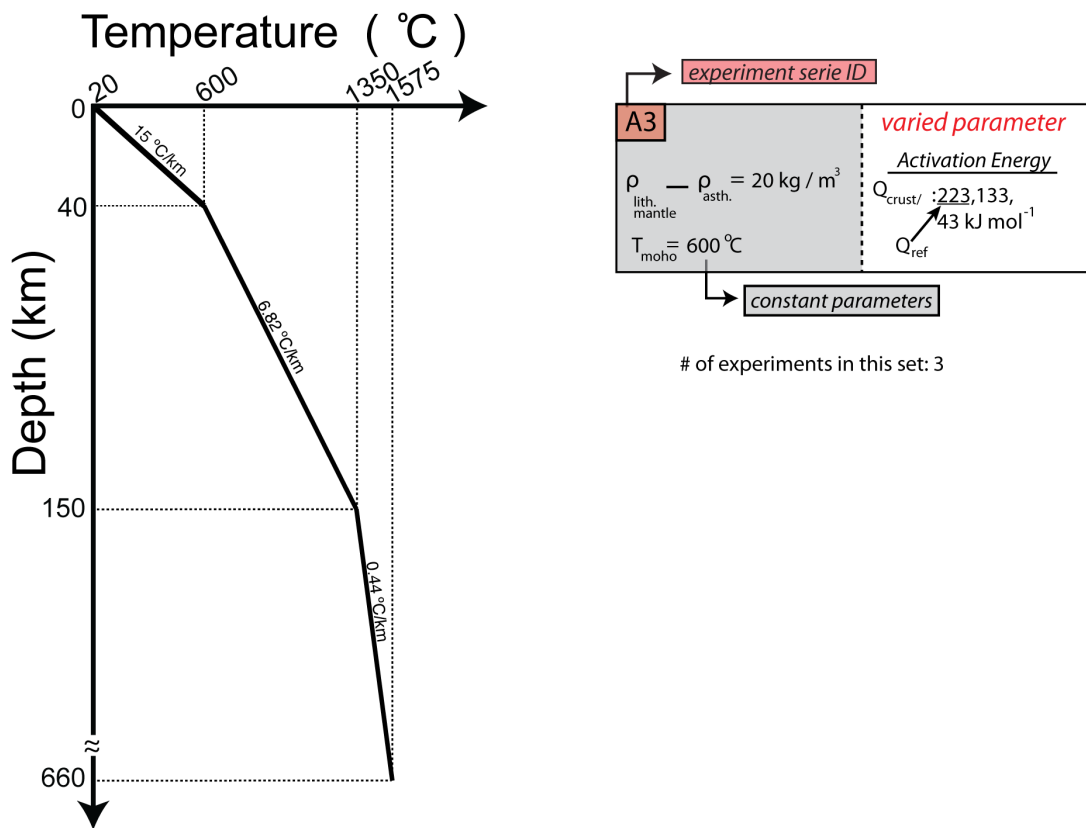


Figure 2.15. Model configuration and flow parameters for the materials of experimental set A3.

2.4.6. Results of A3

When the activation energy of the crust is set to its reference value (223 kJ/mol) the model development is the same with Figure 2.17 and 2.18. At the top of the model, there is continued thickening of the crustal layer in the collision zone. The Rayleigh-Taylor instability is well observed and this instability evolve as more like multiple non-uniform drips.

When the activation energy of the crust is decreased to 133 kJ/mol, the deformation of lagrangian mesh at boundaries suggests that the stress that is supposed to be transferred to the centre of the model domain is mostly distributed through the sides and this can result in less thickening in the crust compared to the previous model. The pressure of the rocks are increased smaller than 1 kbar and this supports the idea of less thickened crust.

If the activation energy of the crust is decreased to 43 kJ/mol, the deformation of the lagrangian mesh suggests extension in the right half of the model due to high deformation in the crust on the sides. This is observed in the left half of the model close the boundary. Due to extension, the rocks start to exhume to the surface, and their pressures decrease about 1 - 2 kbar.

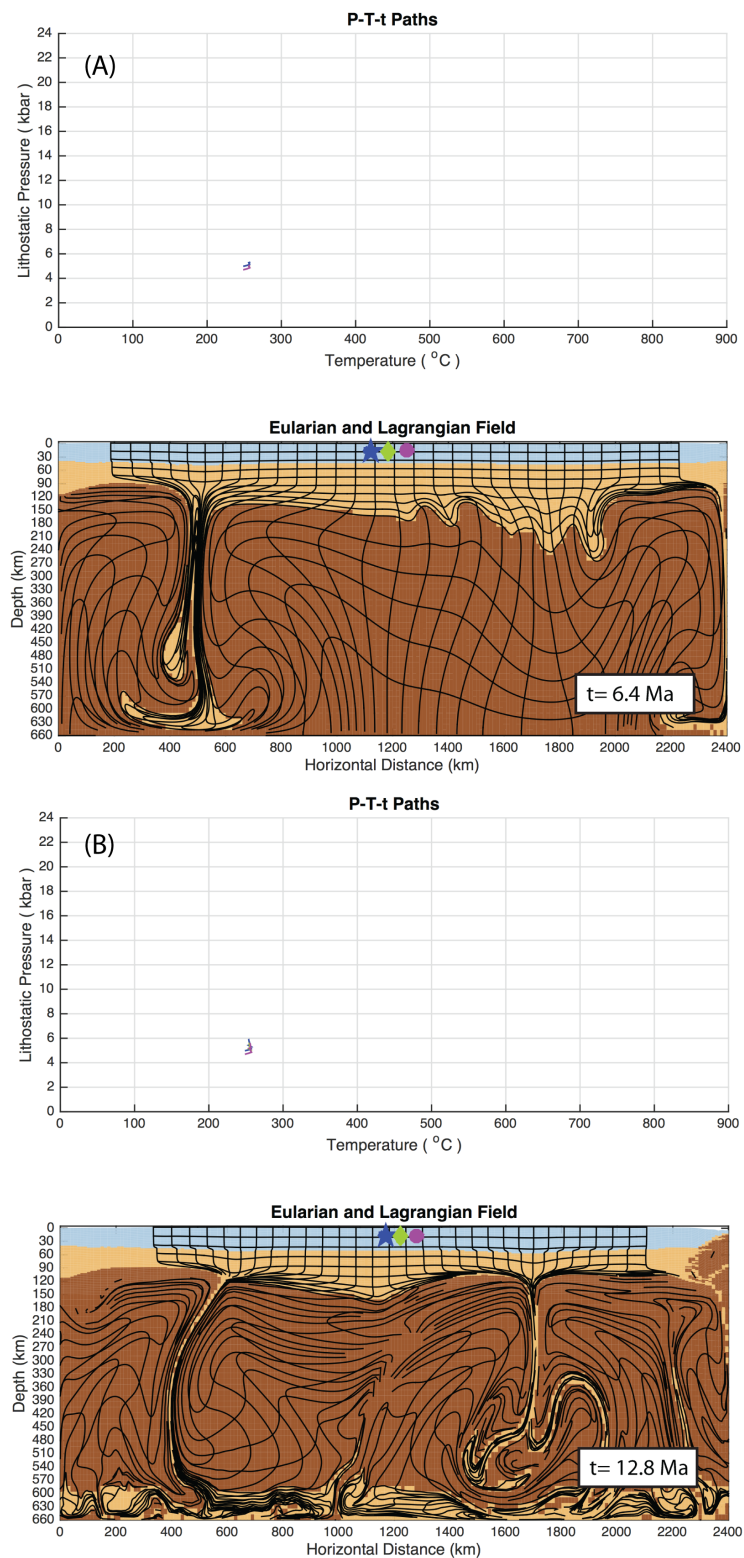


Figure 2.16. Model development and P-T-t paths of tracked particles of experiment A3 with activation energy of 223 kJ/mol in the crust (A) after 6.4 Ma, (B) after 12.8 Ma. Blue: crust, Orange: lithospheric mantle, Brown: asthenosphere.

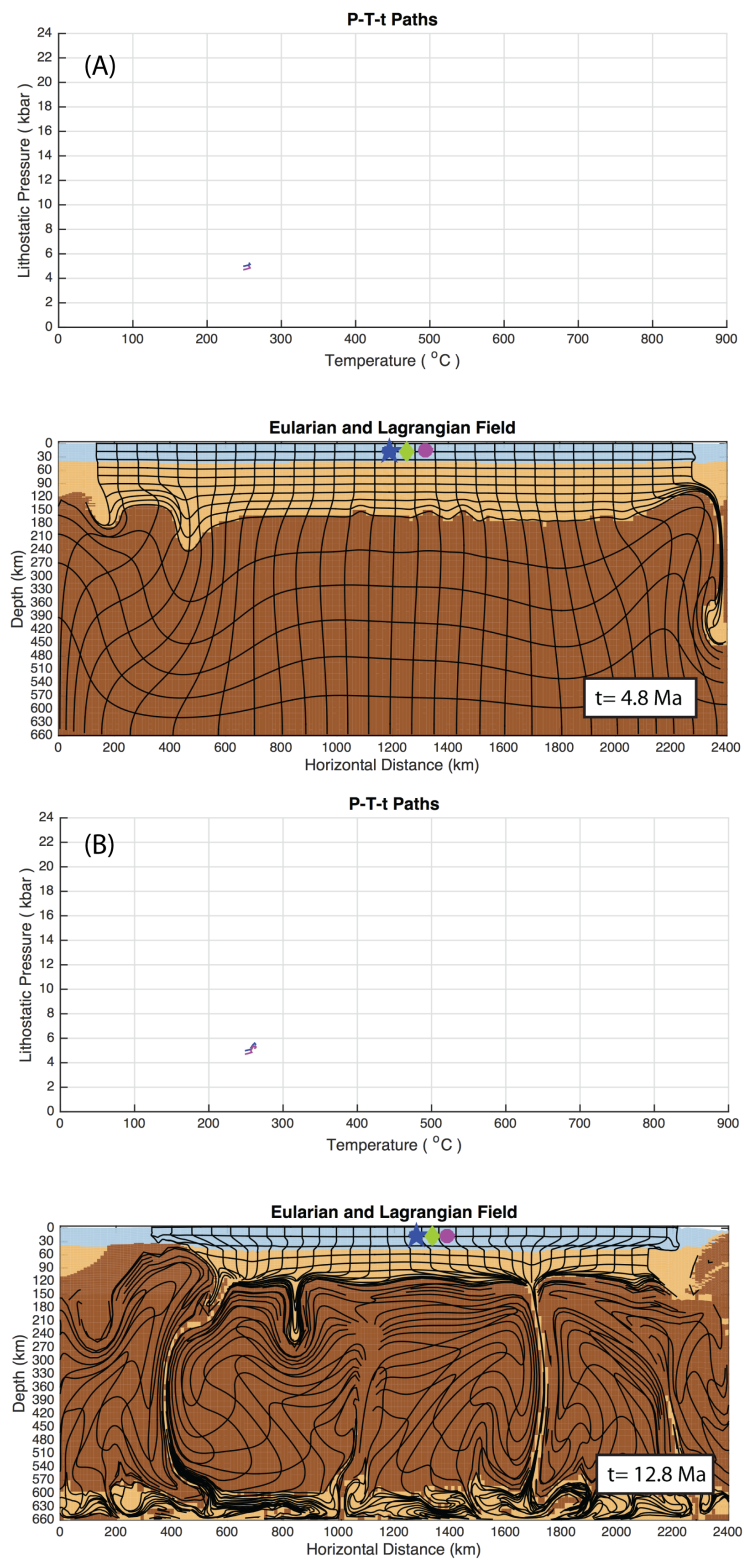


Figure 2.17. Model development and P-T-t paths of tracked particles of experiment A3 with activation energy of 133 kJ/mol in the crust (A) after 4.8 Ma, (B) after 12.8 Ma. Blue: crust, Orange: lithospheric mantle, Brown: asthenosphere.

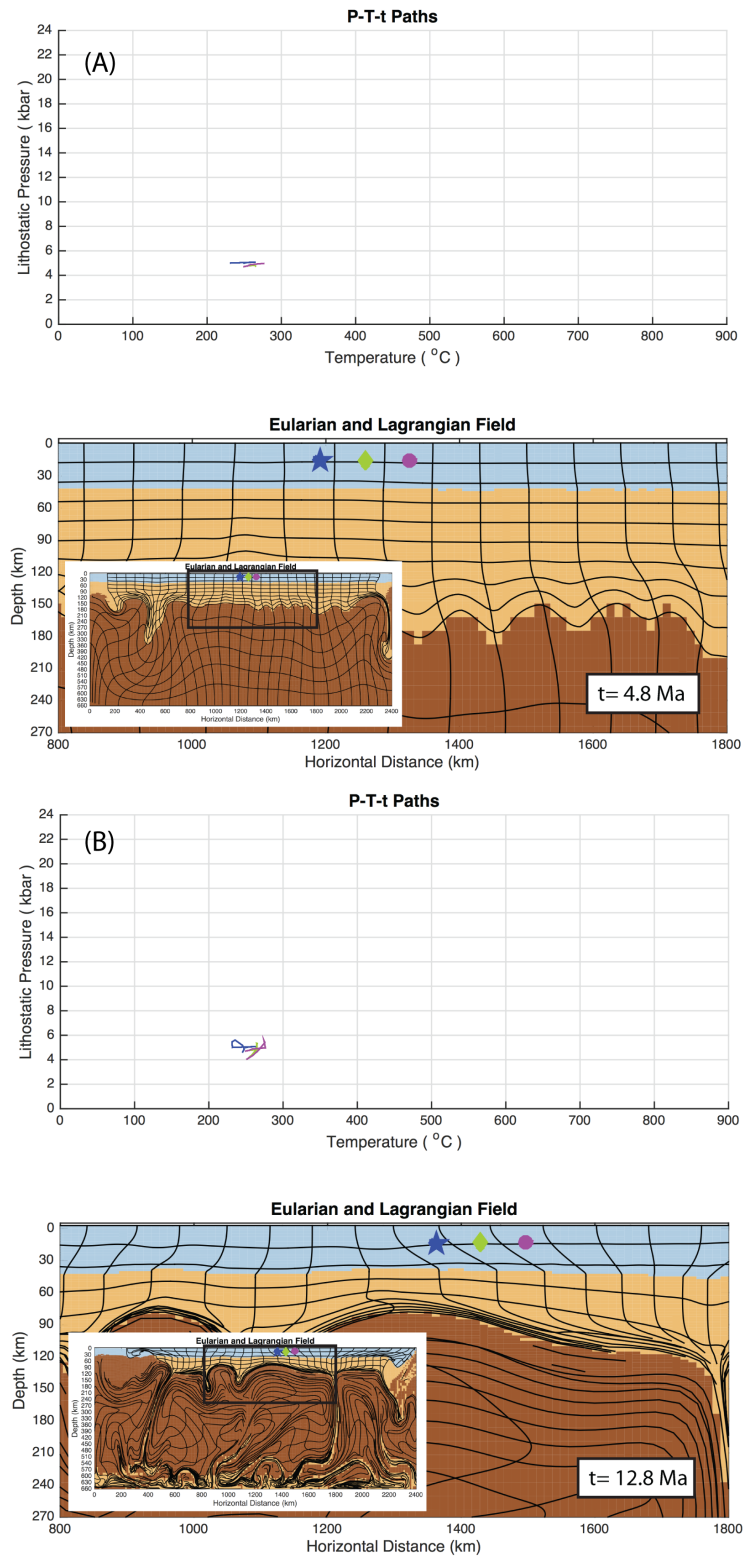


Figure 2.18. Model development and P-T-t paths of tracked particles of experiment A3 with activation energy of 43 kJ/mol in the crust (A) after 4.8 Ma, (B) after 12.8 Ma. Blue: crust, Orange: lithospheric mantle, Brown: asthenosphere.

2.4.7. Experimental Set A4

In experimental set A4, the same type of configuration was preserved with experimental set A3 except the Moho temperature was increased to 900 °C for all models in this set. The activation energy of crust was decreased from 223 kJ/mol to 133 kJ/mol and 43 kJ/mol. The temperature at lithosphere-asthenosphere boundary (LAB) was set as 1350 °C. The lower boundary of the box had an initial temperature of 1575 °C. The densities of crust, lithospheric mantle and asthenospheric mantle were set as 2800 kg/m^3 , 3300 kg/m^3 and 3280 kg/m^3 respectively. The deformation in the upper crust is visco-plastic, in other words, the numerical code chooses the possible lowest stress level (viscous or plastic) throughout the crust. The same type of deformation was prescribed for the mantle as well.

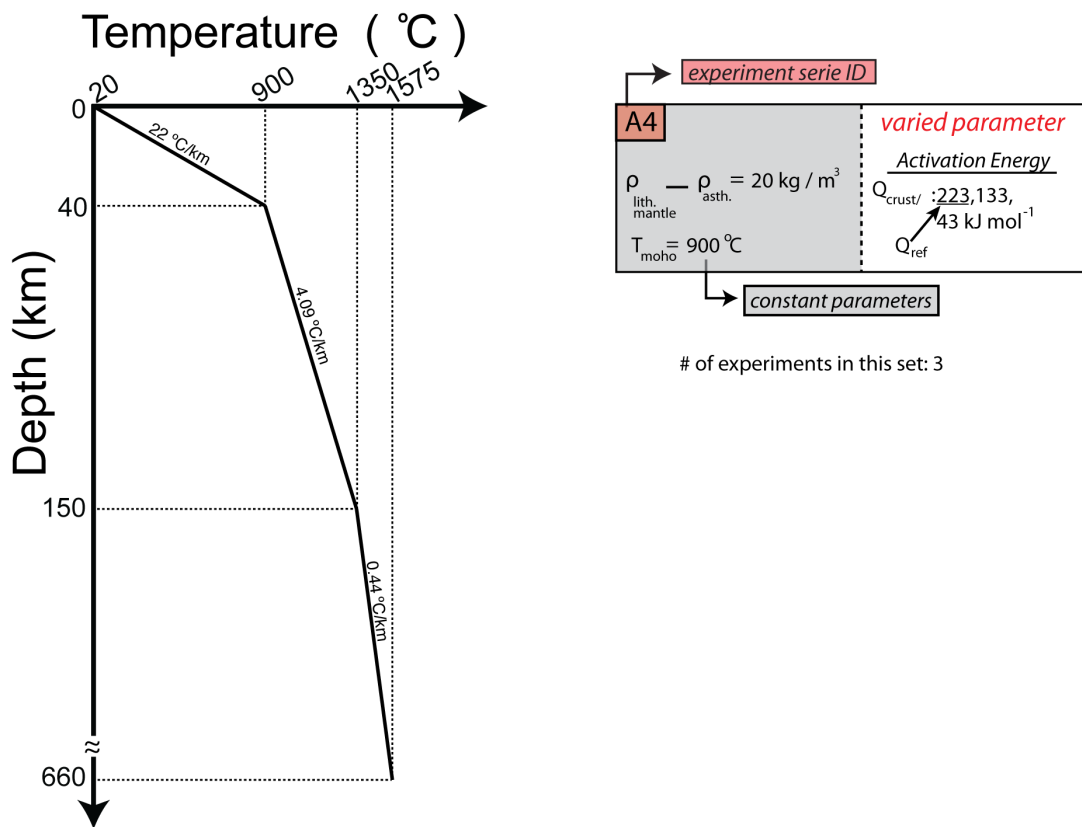
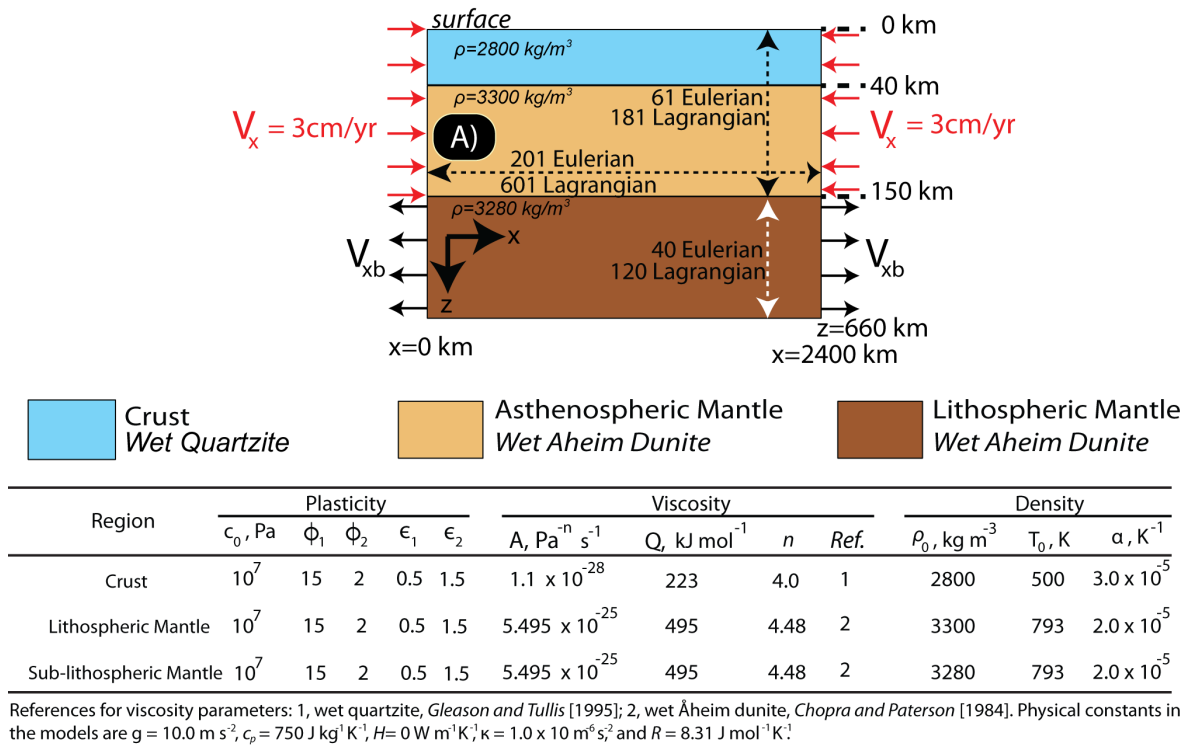


Figure 2.19. Model configuration and flow parameters for the materials of experimental set A4.

2.4.8. Results of A4

When the activation energy of crust is at its reference value (223 kJ/mol), after 14.5 Ma, most of the lithospheric mantle drips down into the asthenosphere. The pressure of rocks increase about 1 kbar and the temperature decrease by 70 °C.

If we decrease the activation energy of the crust to 133 kJ/mol, right at the axis of dripping instability, the crust is affected by downward pull during dripping instability, and force release after the detachment of the lithospheric mantle. This is well exposed as a plume like exhumation of middle crust from the centre of the model domain to the sides. Though there is not significant increase in pressure levels, the exhumation of middle crustal rocks are clearly seen.

When the activation energy of crust is decreased down to 43 kJ/mol, the non-symmetric drip initiates on the right half of the model domain. This is clearly seen in Figure 2.35. Expectedly, the pressure of middle crustal rocks increase by about 2 kbar at most due to significant pull force by the dripping lithospheric mantle. There is also cooling about 90 °C during the burial of these rocks. After 14.5 Ma, the rocks are exhumed to the surface in the crust with an asymmetric deformation.

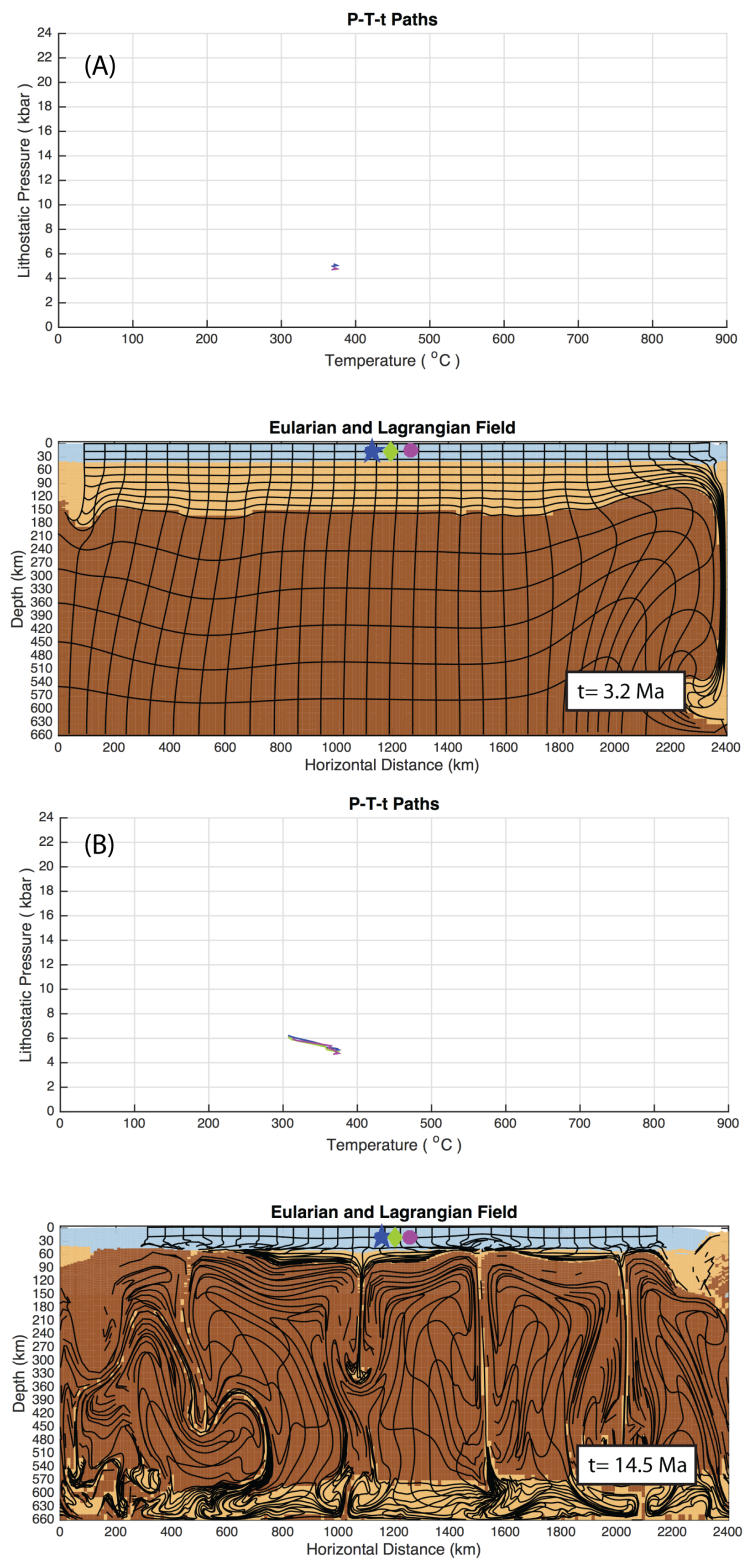


Figure 2.20. Model development and P-T-t paths of tracked particles of experiment A4 with activation energy of 223 kJ/mol in the crust (A) after 3.2 Ma, (B) after 14.5 Ma. Blue: crust, Orange: lithospheric mantle, Brown: asthenosphere.

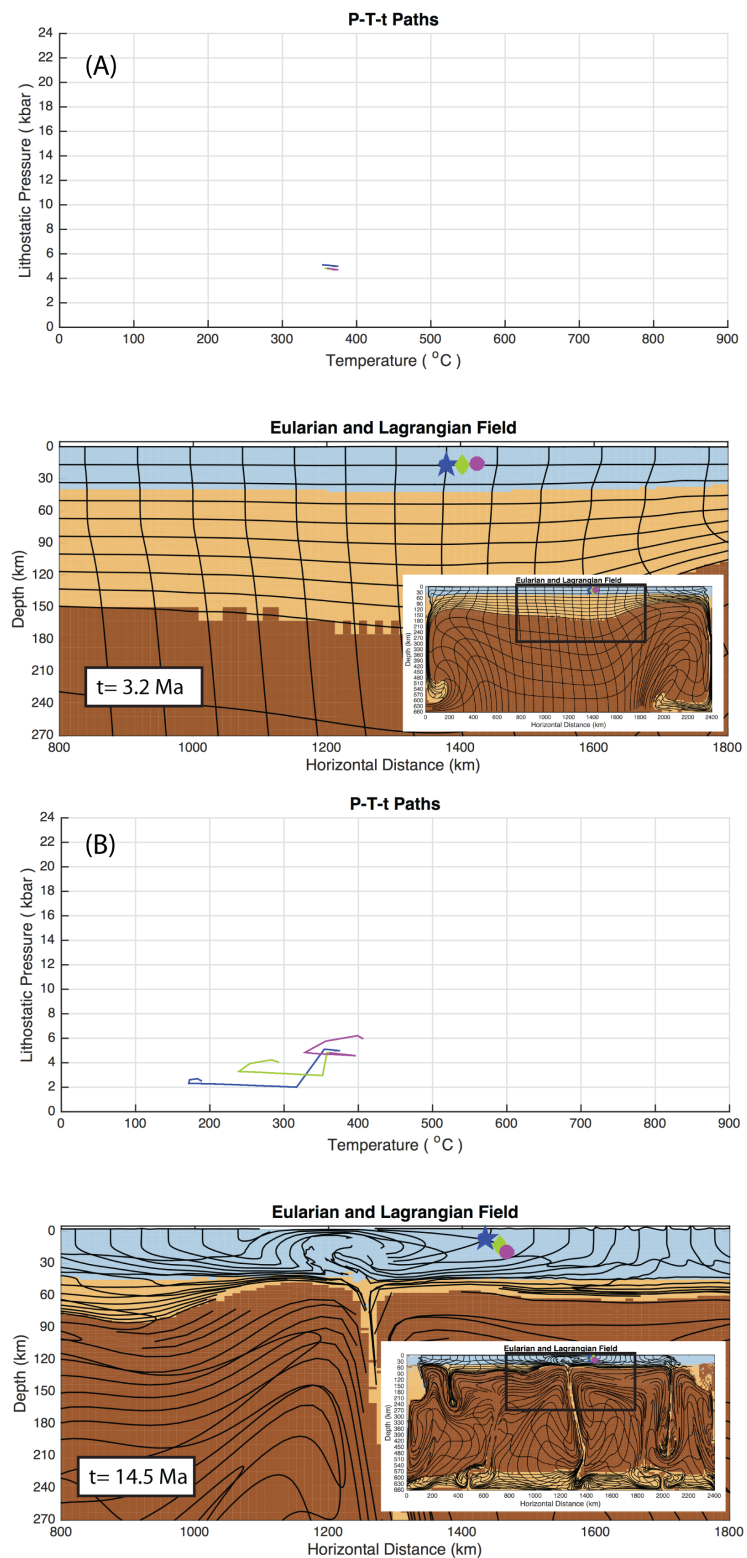


Figure 2.21. Model development and P-T-t paths of tracked particles of experiment A4 with activation energy of 133 kJ/mol in the crust (A) after 3.2 Ma, (B) after 14.5 Ma. Blue: crust, Orange: lithospheric mantle, Brown: asthenosphere.

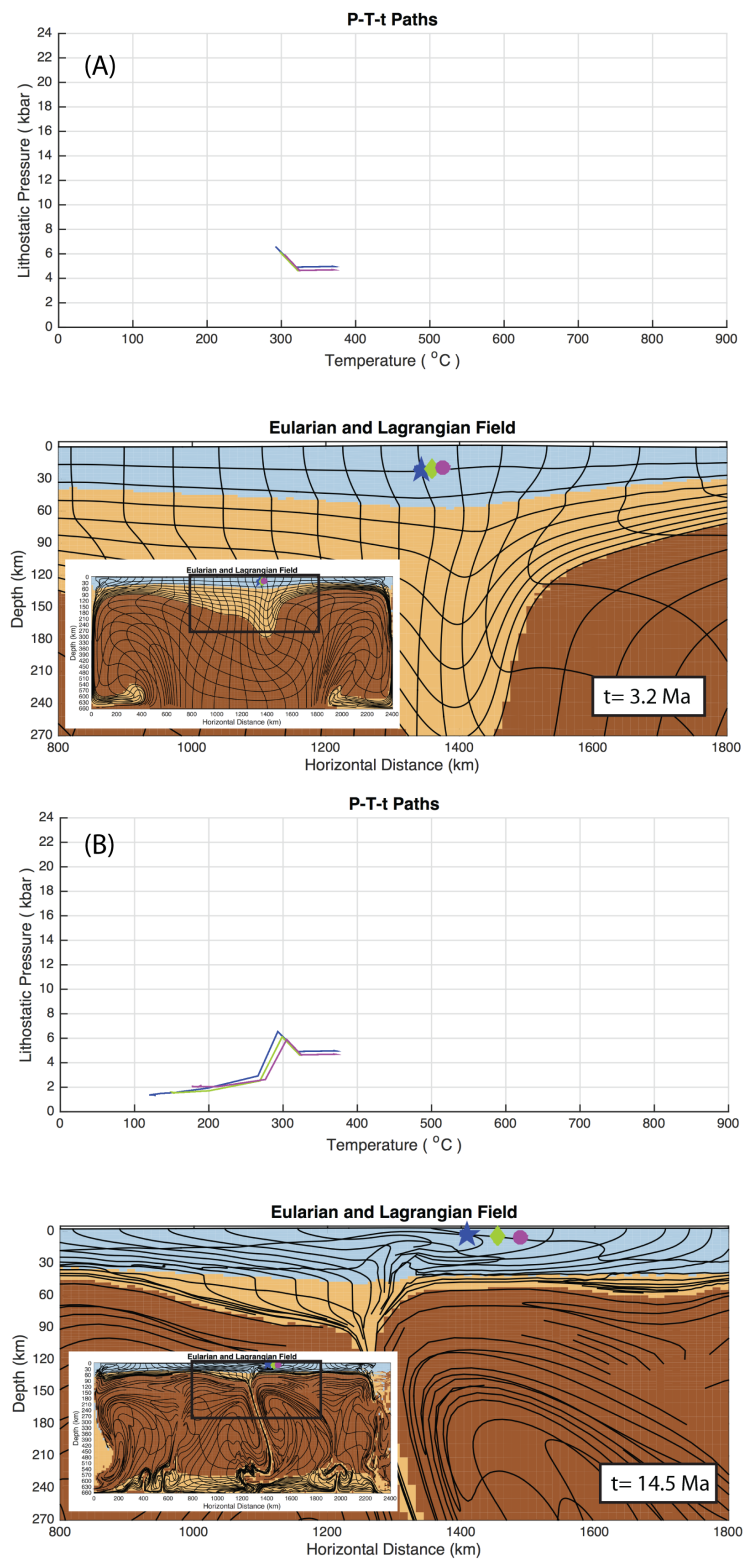


Figure 2.22. Model development and P-T-t paths of tracked particles of experiment A4 with activation energy of 43 kJ/mol in the crust (A) after 3.2 Ma, (B) after 14.5 Ma. Blue: crust, Orange: lithospheric mantle, Brown: asthenosphere.

2.4.9. Experimental Set B1

In experimental set B1, a distinctive felsic granulite lower crust and a bulge in the lithospheric mantle was prescribed. The density difference between lithospheric mantle and asthenosphere was kept the same as previous models. Moho temperature was increased starting from 450 °C with 150 °C increments up to 900 °C. The temperature at lithosphere-asthenosphere boundary (LAB) was set as 1350 °C. The lower boundary of the box had an initial temperature of 1575 °C. The densities of upper/middle crust, lower crust, lithospheric mantle and asthenospheric mantle were set as 2800 kg/m^3 , 2900 kg/m^3 , 3300 kg/m^3 and 3280 kg/m^3 respectively. The deformation in the upper crust is visco-plastic, in other words, the numerical code chooses the possible lowest stress level (viscous or plastic), however, the lower deformation in the lower crust is viscous. Material properties of the mantle were kept the same.

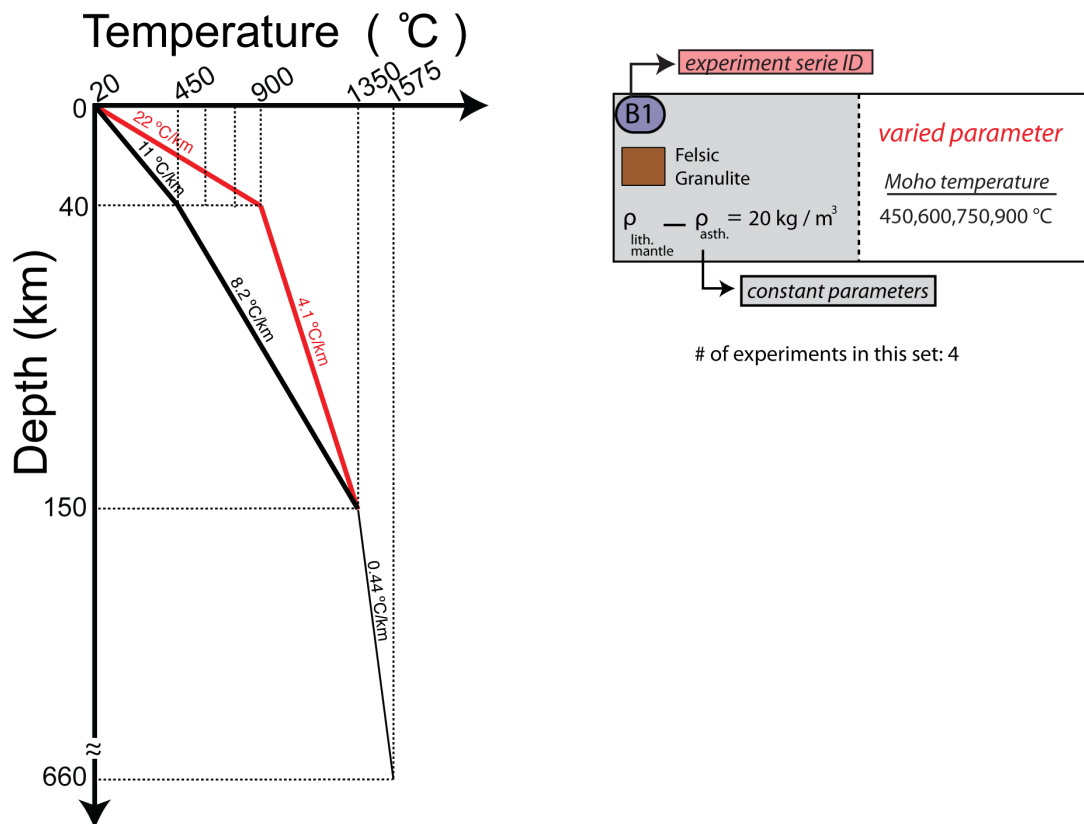
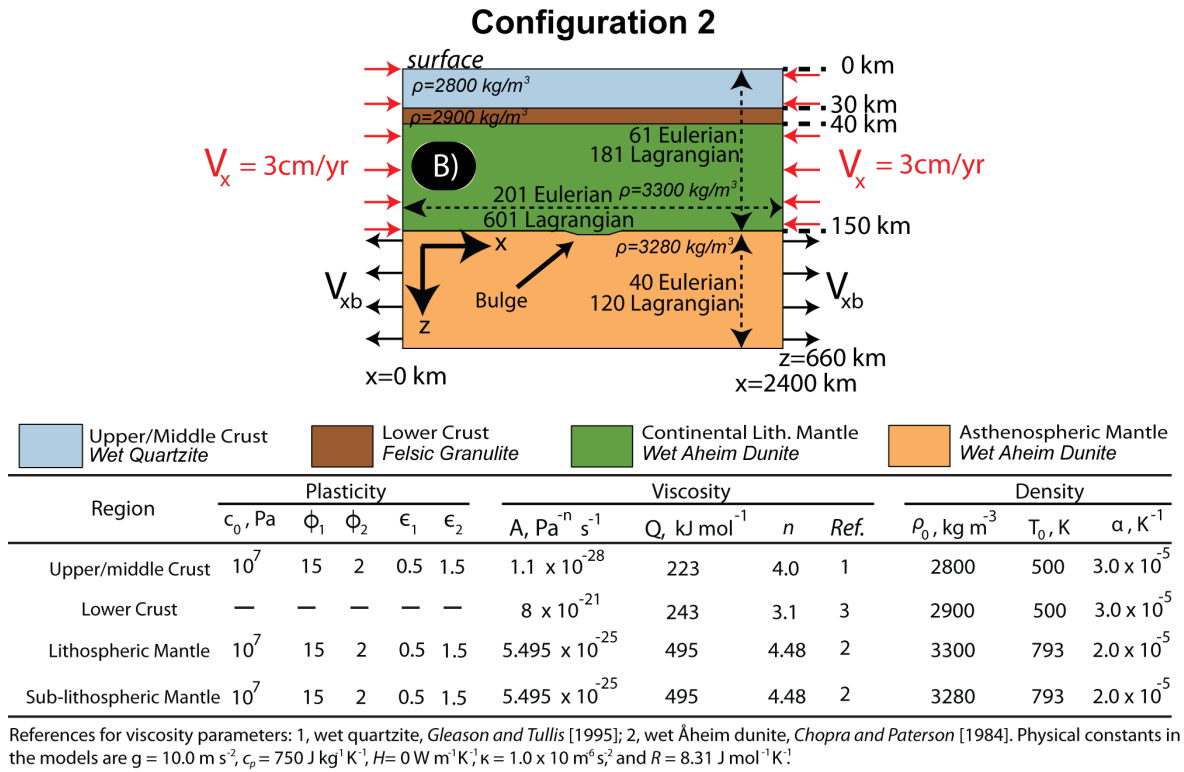


Figure 2.23. Model configuration and flow parameters for the materials of experimental set B1.

2.4.10. Results of B1

When the Moho temperature is set to 450 °C, there initiates a single drip right on the axis of the bulge, and the root of that drip does not extend above 100 km depth. After 11.3 Ma, the pressure of rocks tracked from lower crust increase by about 3 kbar, but there is no significant change in temperature.

If we increase the Moho temperature to 600 °C, after 11.3 Ma, larger area of the lithospheric mantle is removed. The thickness of the lithosphere decreases to about 110 km in the centre. The pressures of the rocks increase by 2-3 kbar and the temperatures decreases by about 50 °C.

If the Moho temperature is set to 750 °C, Rayleigh-Taylor instability evolves as a strong and more rapid drip. This affects the lower crust by pulling some part of it as shown in Figure 2.42. The pressures of the rocks increase by about 2 kbar and their temperatures decrease by about 30 °C. After 11.3 Ma, the dripping lithospheric mantle already detaches from the upper part. Due to continued convergence in the collision zone, the lower crust is accumulated right on the top of dripping instability, and applies some stress to the upper levels. Though pressures of the tracked rocks decrease about 2 kbar at most, they can not achieve to exhume to the surface, because the crust is strong enough so that it can not deform significantly when acted upon such level of stress.

When the the Moho temperature is set to 900 °C, the plume like exhumation is discernible, and there is no connection with lithospheric mantle in the centre of model domain. Because the lower crust is exposed to asthenospheric flow underneath, the temperature of the exhumed rocks starts to increase already before 11.3 Ma. The lower crust is not strong enough to force the upper crust and exhume.

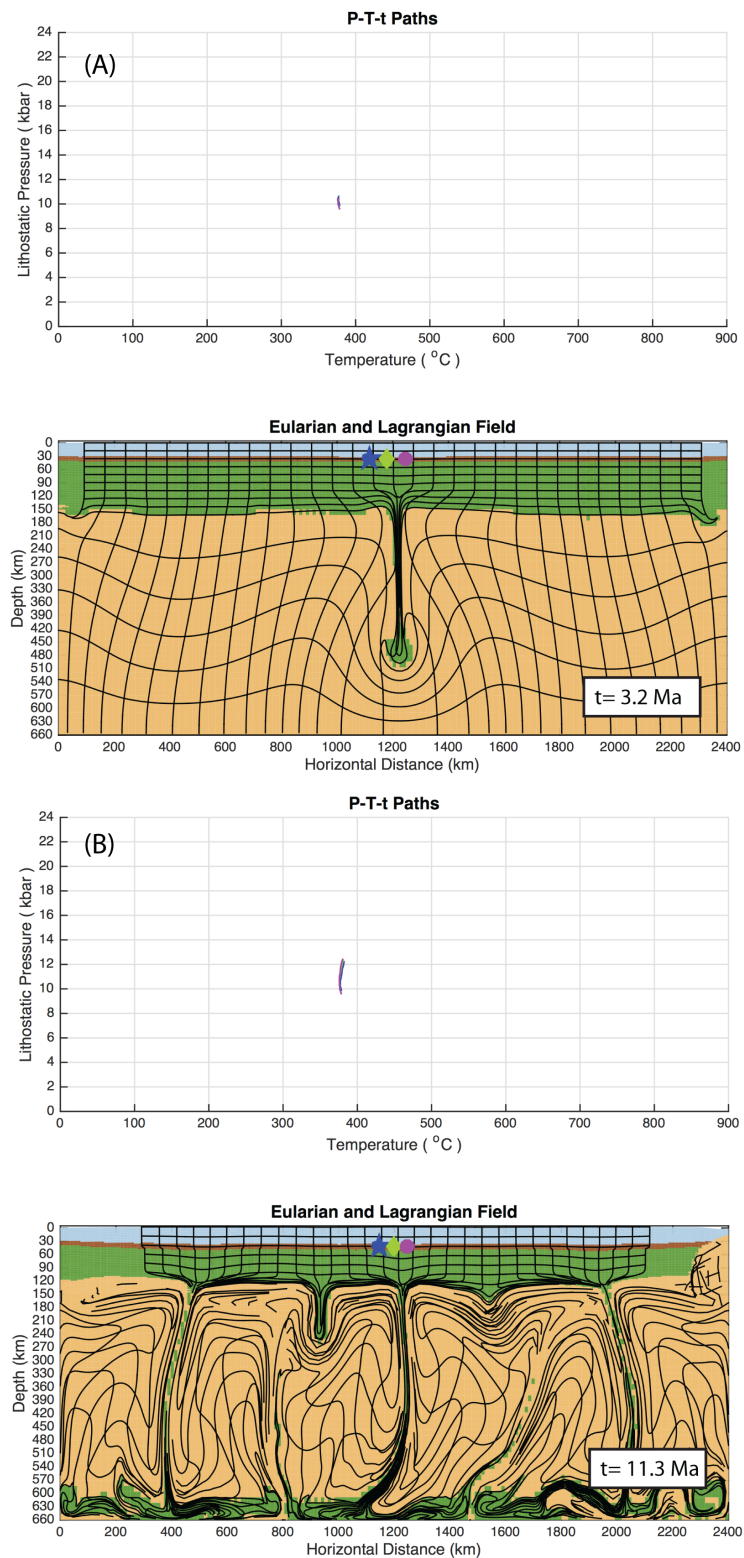


Figure 2.24. Model development and P-T-t paths of tracked particles of experiment B1 with Moho temperature of 450°C (A) after 3.2 Ma, (B) after 11.3 Ma. Blue: upper/middle crust, Brown: lower crust, Green: lith. mantle, Orange: asthenosphere.

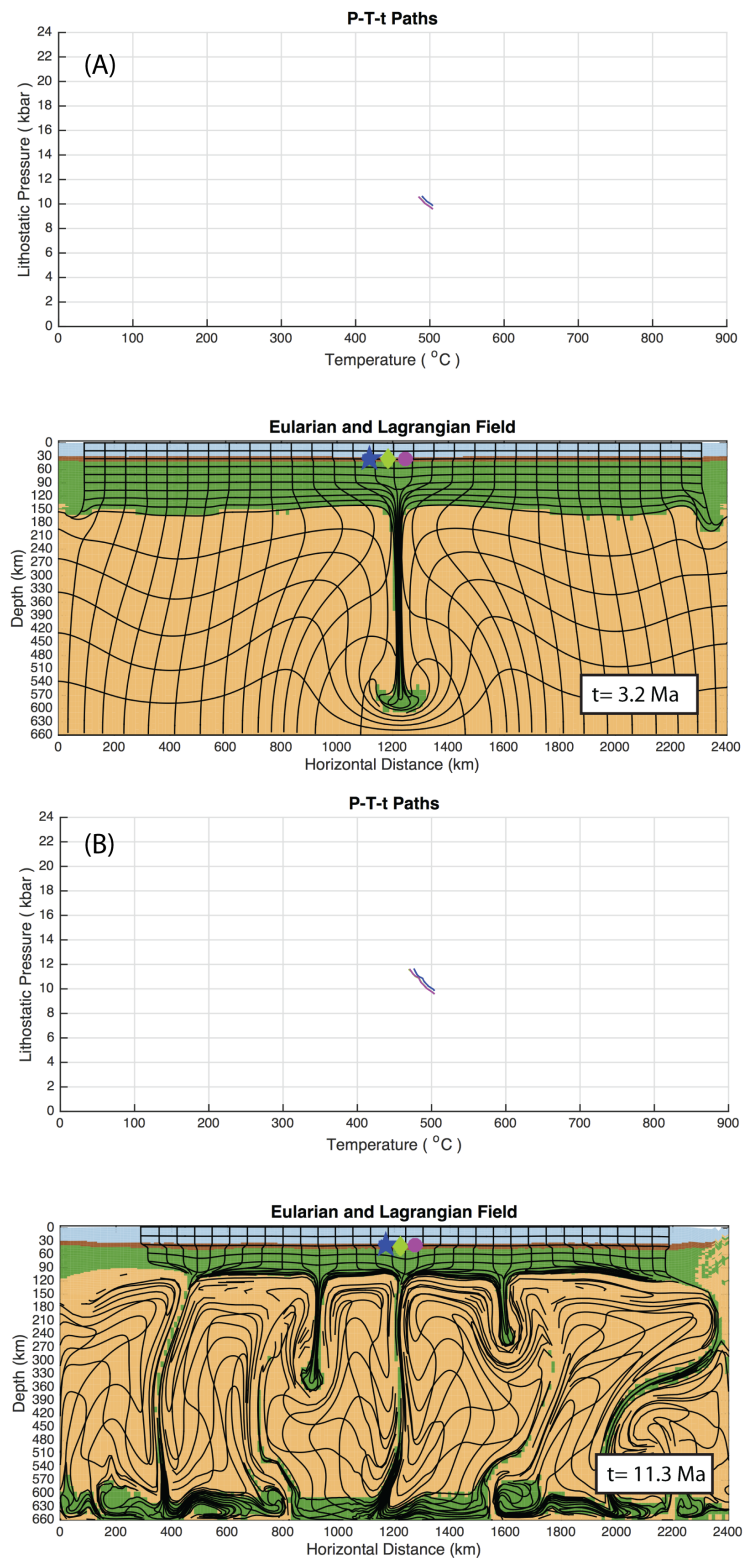


Figure 2.25. Model development and P-T-t paths of tracked particles of experiment B1 with Moho temperature of 600°C (A) after 3.2 Ma, (B) after 11.3 Ma. Blue: upper/middle crust, Brown: lower crust, Green: lith. mantle, Orange: asthenosphere.

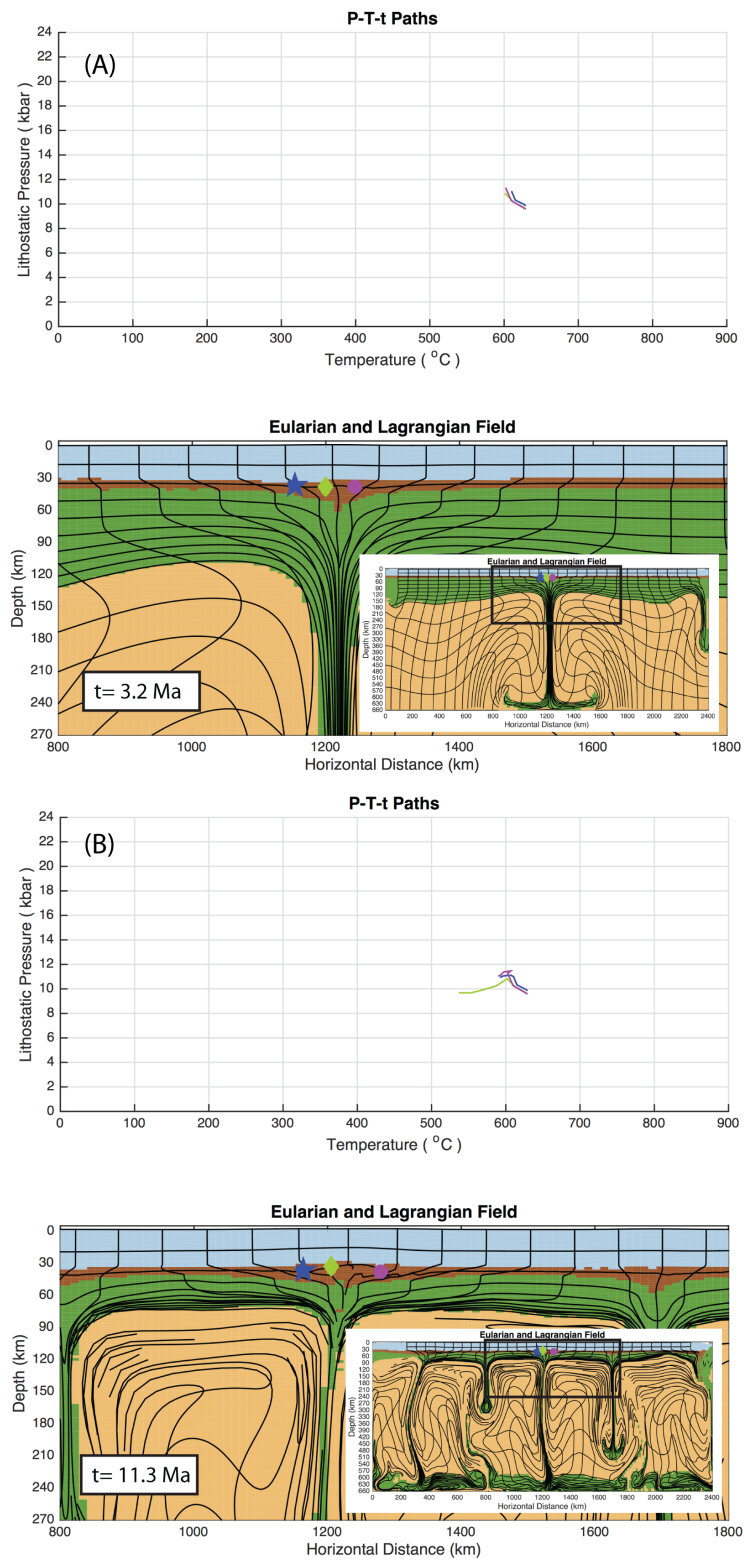


Figure 2.26. Model development and P-T-t paths of tracked particles of experiment B1 with Moho temperature of 750°C (A) after 3.2 Ma, (B) after 11.3 Ma. Blue: upper/middle crust, Brown: lower crust, Green: lith. mantle, Orange: asthenosphere.

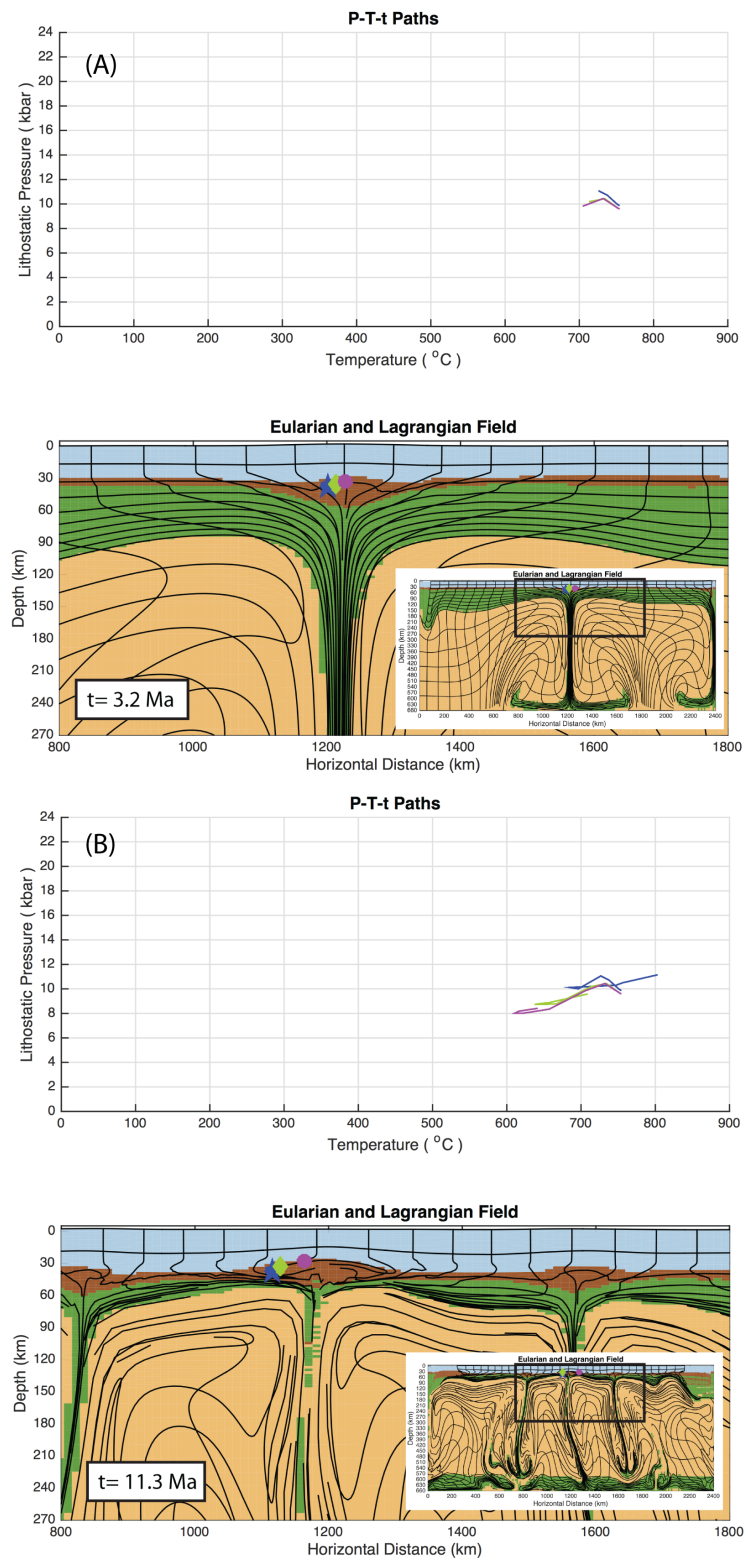
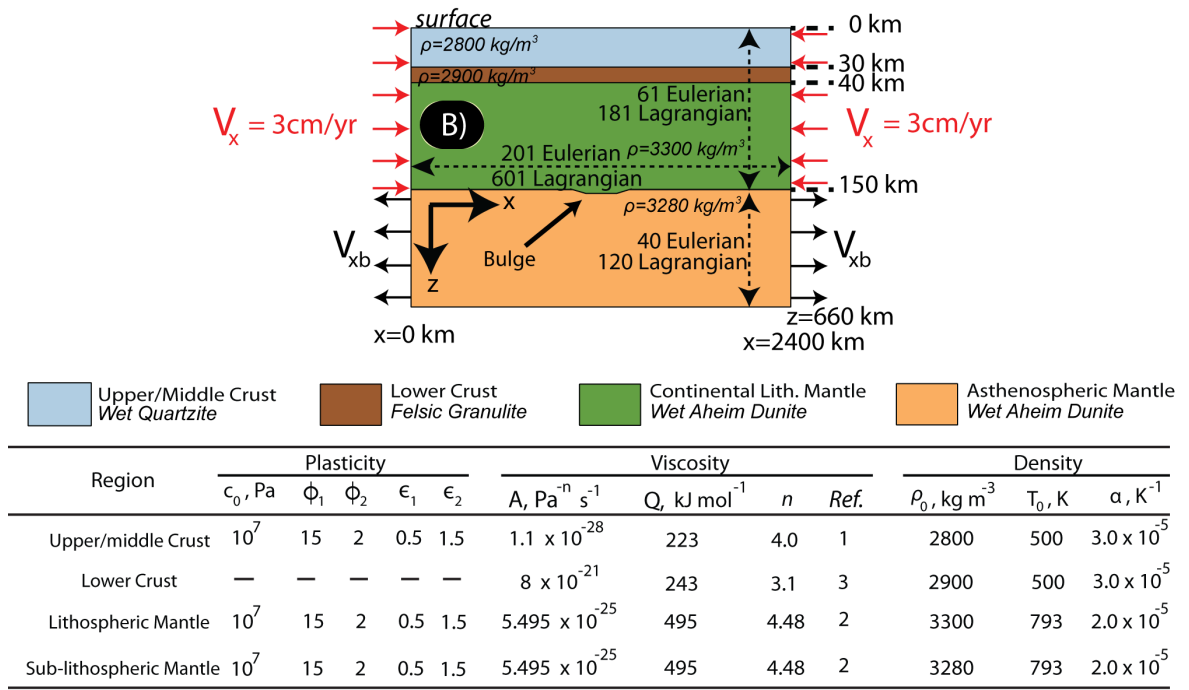


Figure 2.27. Model development and P-T-t paths of tracked particles of experiment B1 with Moho temperature of 900°C (A) after 3.2 Ma, (B) after 11.3 Ma. Blue: upper/middle crust, Brown: lower crust, Green: lith. mantle, Orange: asthenosphere.

2.4.11. Experimental Set B2

In experimental set B2, the model geometry was kept the same like experimental set B1. The aim of this experimental set is to identify the effect of activation energy in this configuration. The density difference between lithospheric mantle and asthenosphere was kept the same as previous models. Keeping the Moho temperature constant as 600 °C, the activation energy of upper/middle crust was decreased from 223 kJ/mol to 133 kJ/mol and down to 43 kJ/mol. The temperature at lithosphere-asthenosphere boundary (LAB) was set as 1350 °C. The lower boundary of the box had an initial temperature of 1575 °C. The densities of upper/middle crust, lower crust, lithospheric mantle and asthenospheric mantle were set as 2800 kg/m^3 , 2900 kg/m^3 , 3300 kg/m^3 and 3280 kg/m^3 respectively. The deformation in the upper crust is visco-plastic, in other words, the numerical code chooses the possible lowest stress level (viscous or plastic), however, the lower deformation in the lower crust is viscous. Material properties of the mantle were kept the same.



References for viscosity parameters: 1, wet quartzite, Gleason and Tullis [1995]; 2, wet Åheim dunite, Chopra and Paterson [1984]. Physical constants in the models are $g = 10.0 \text{ m s}^{-2}$, $c_p = 750 \text{ J kg}^{-1} \text{ K}^{-1}$, $H = 0 \text{ W m}^{-1} \text{ K}^{-1}$, $\kappa = 1.0 \times 10^{-6} \text{ s}^{-2}$ and $R = 8.31 \text{ J mol}^{-1} \text{ K}^{-1}$.

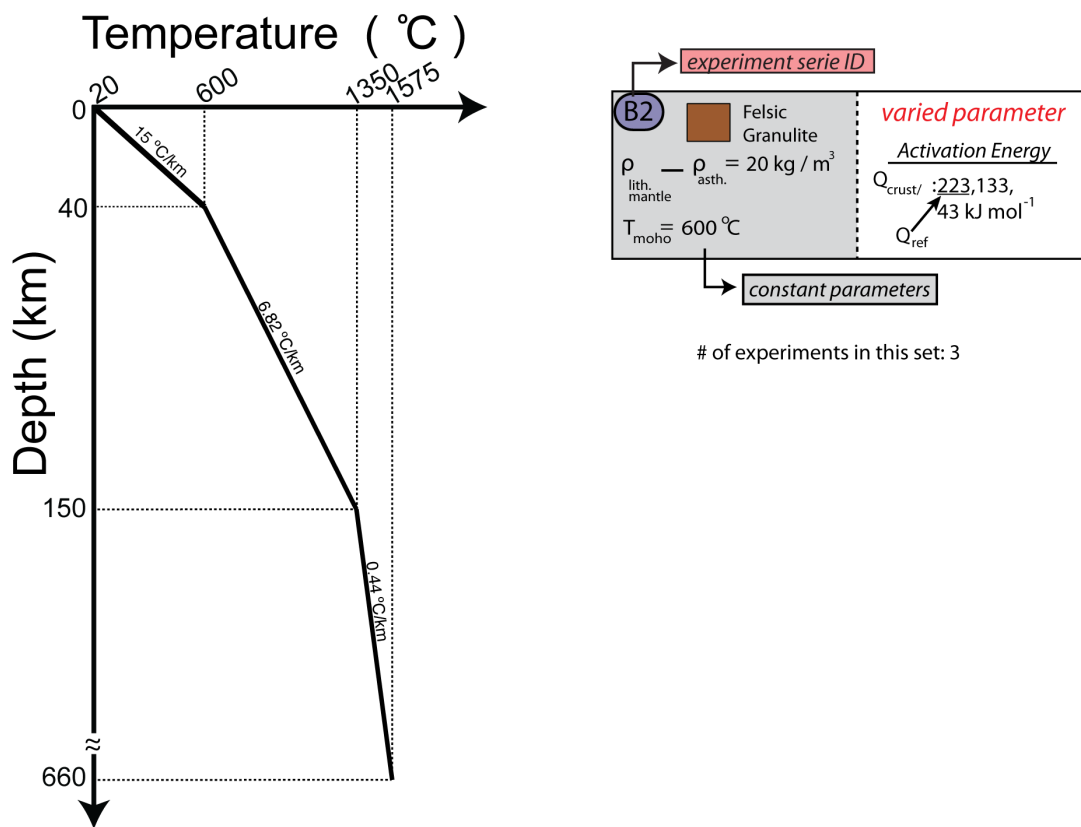


Figure 2.28. Model configuration and flow parameters for the materials of experimental set B2.

2.4.12. Results of B2

When the activation energy of upper/middle crust is at its reference value (223 kJ/mol) the P-T-t paths of tracked particles and Rayleigh-Taylor instability in the lithosphere develops in the same way we elaborated in model B1-600, Figure 2.40 and 2.41.

If the activation energy of the upper/middle crust is decreased to 133 kJ/mol, the pressures of tracked particles increase about 2 kbar and their temperatures decrease about 50 °C after 11.3 Ma. The deformation of lagrangian mesh suggests some weakness in the upper/middle crust, but because the dripping instability is not effective on the lower crust, it can not accumulate in specific regions along the model domain and there is no significant force acting upon the upper/middle crust by the lower crust. Therefore, no exhumation is observed.

Decreasing the activation energy of the lower crust down to 43 kJ/mol can not provide significant burial and exhumation, because even the crust is deforming high enough, the dripping instability is still not effective on the lower crust, and this is related to relatively lower temperatures in the Moho.

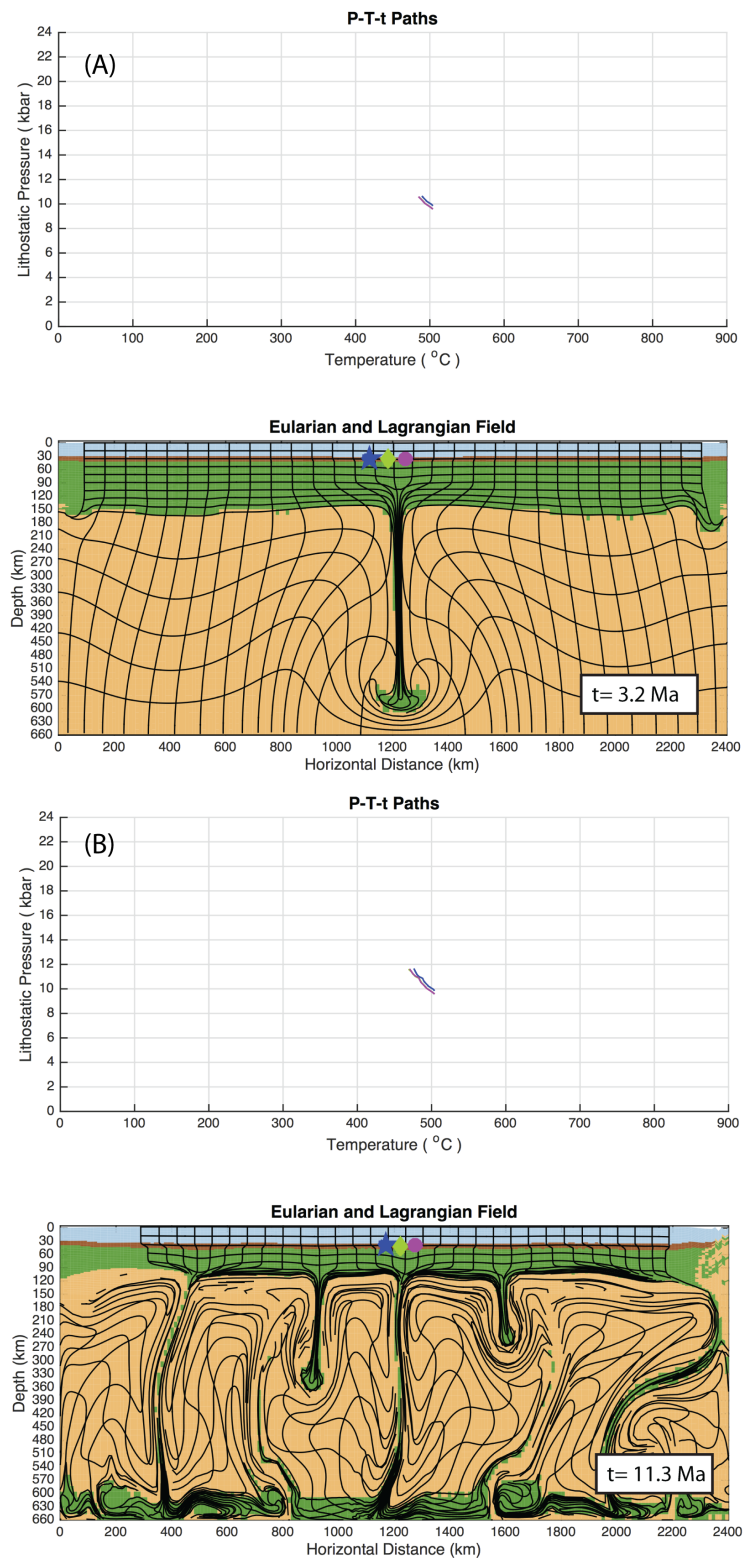


Figure 2.29. Model development and P-T-t paths of tracked particles of experiment B2 with activation energy of 223 kJ/mol in the u/m crust (A) after 3.2 Ma, (B) after 11.3 Ma. Blue: u/m crust, Brown: low. crust, Green: lith. mantle, Orange: asth.

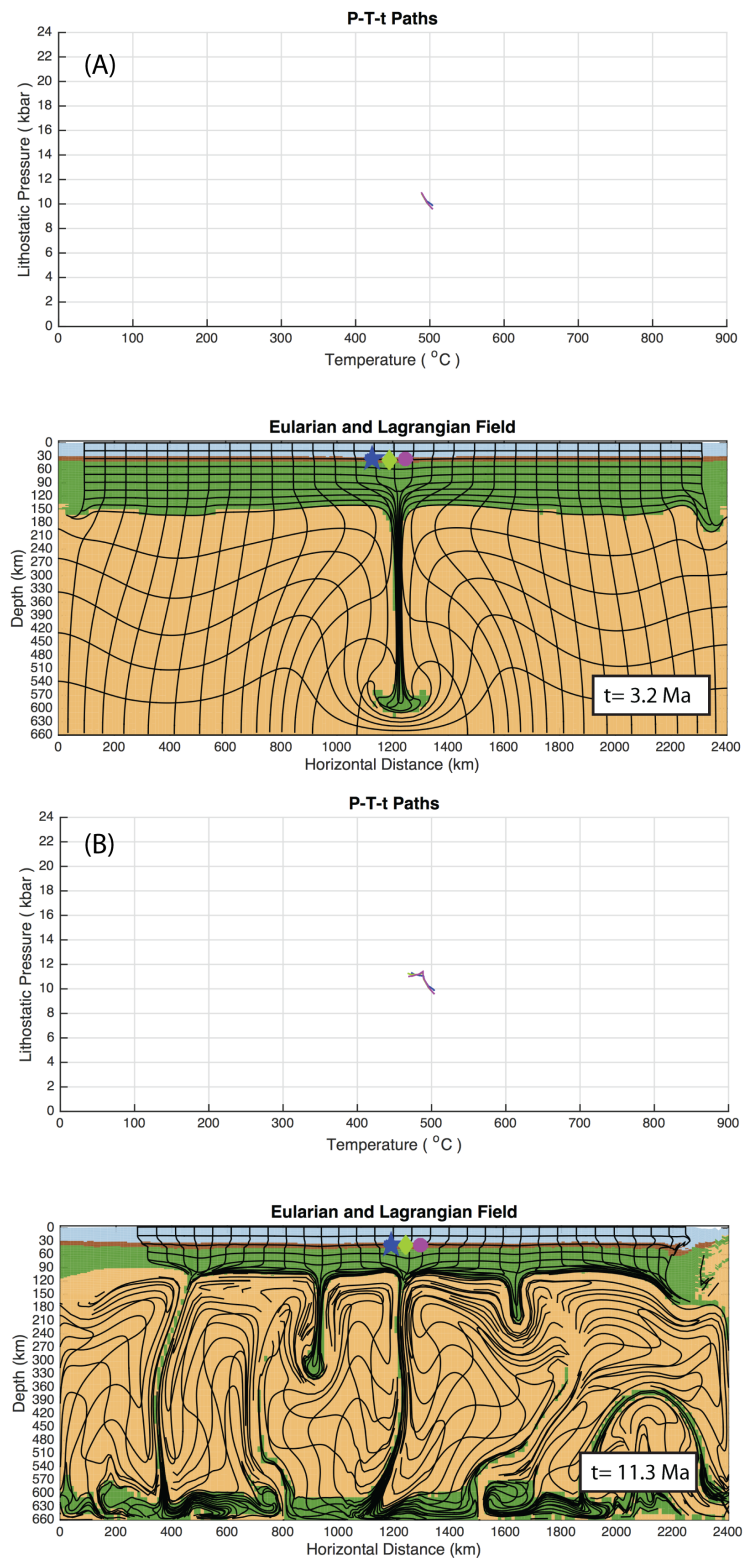


Figure 2.30. Model development and P-T-t paths of tracked particles of experiment B2 with activation energy of 133 kJ/mol in the u/m crust (A) after 3.2 Ma, (B) after 11.3 Ma. Blue: u/m crust, Brown: low. crust, Green: lith. mantle, Orange: asth.

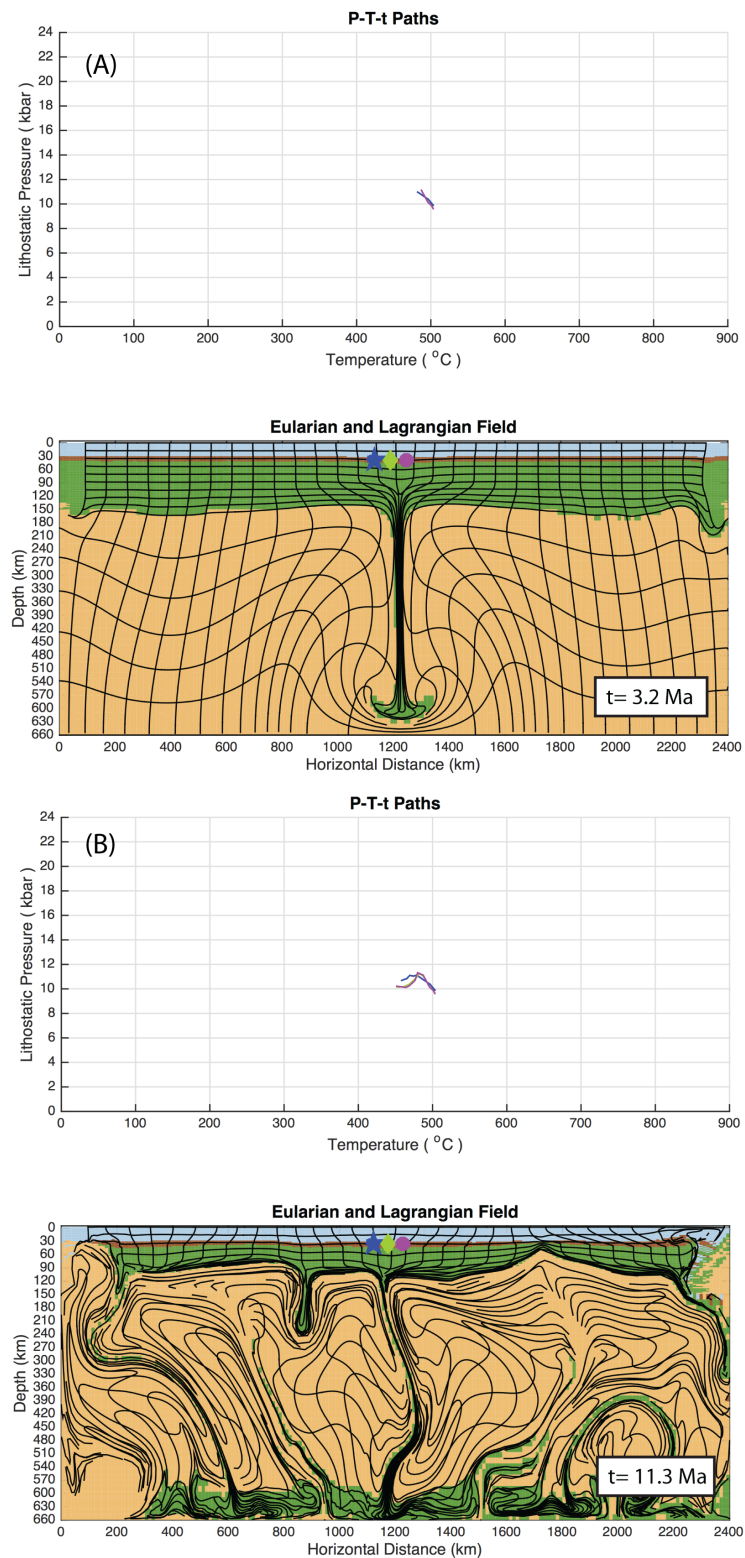
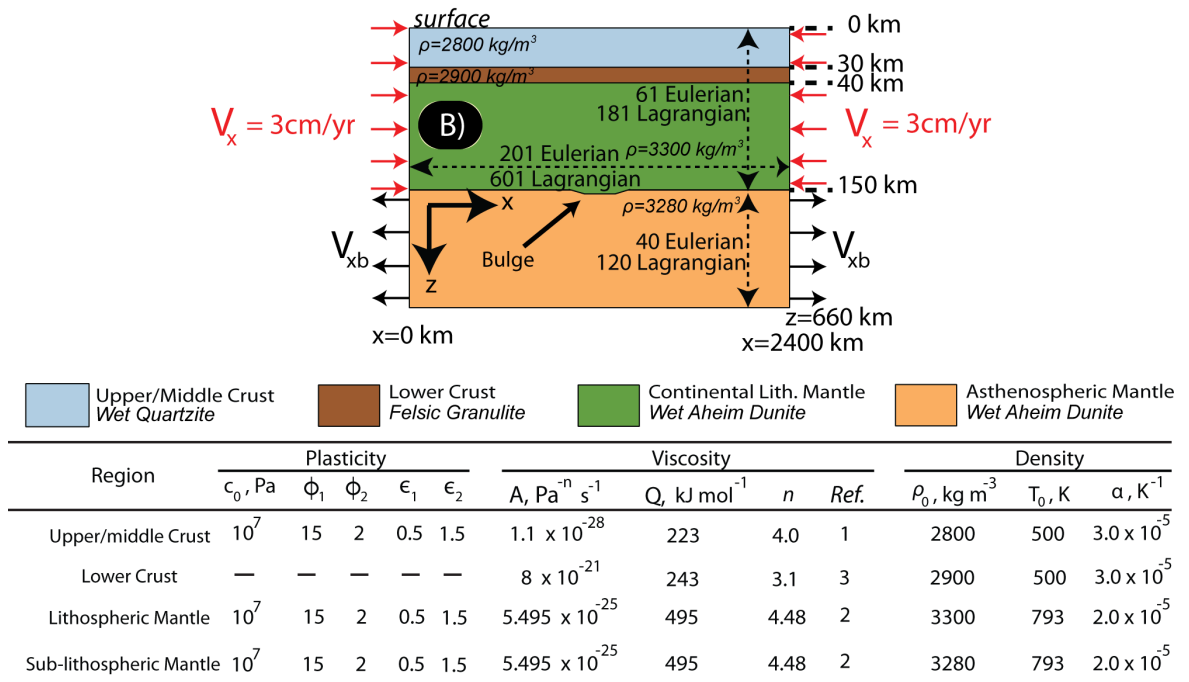


Figure 2.31. Model development and P-T-t paths of tracked particles of experiment B2 with activation energy of 43 kJ/mol in the u/m crust (A) after 3.2 Ma, (B) after 11.3 Ma. Blue: u/m crust, Brown: low. crust, Green: lith. mantle, Orange: asth.

2.4.13. Experimental Set B3

In experimental set B3, the model geometry was kept the same like experimental set B1 and B2. The aim of this experimental set is to identify the effect of activation energy in a hot orogeny. The density difference between lithospheric mantle and asthenosphere was kept the same as previous models. Keeping the Moho temperature constant as 900 °C, the activation energy of upper/middle crust was decreased from 223 kJ/mol to 43 kJ/mol. The temperature at lithosphere-asthenosphere boundary (LAB) was set as 1350 °C. The lower boundary of the box had an initial temperature of 1575 °C. The densities of upper/middle crust, lower crust, lithospheric mantle and asthenospheric mantle were set as 2800 kg/m^3 , 2900 kg/m^3 , 3300 kg/m^3 and 3280 kg/m^3 respectively. The deformation in the upper crust is visco-plastic, in other words, the numerical code chooses the possible lowest stress level (viscous or plastic), however, the lower deformation in the lower crust is viscous. Material properties of the mantle were kept the same.



References for viscosity parameters: 1, wet quartzite, Gleason and Tullis [1995]; 2, wet Aheim dunite, Chopra and Paterson [1984]. Physical constants in the models are $g = 10.0 \text{ m s}^{-2}$, $c_p = 750 \text{ J kg}^{-1} \text{K}^{-1}$, $H = 0 \text{ W m}^{-1} \text{K}^{-1}$, $\kappa = 1.0 \times 10^{-6} \text{ s}^{-2}$ and $R = 8.31 \text{ J mol}^{-1} \text{K}^{-1}$.

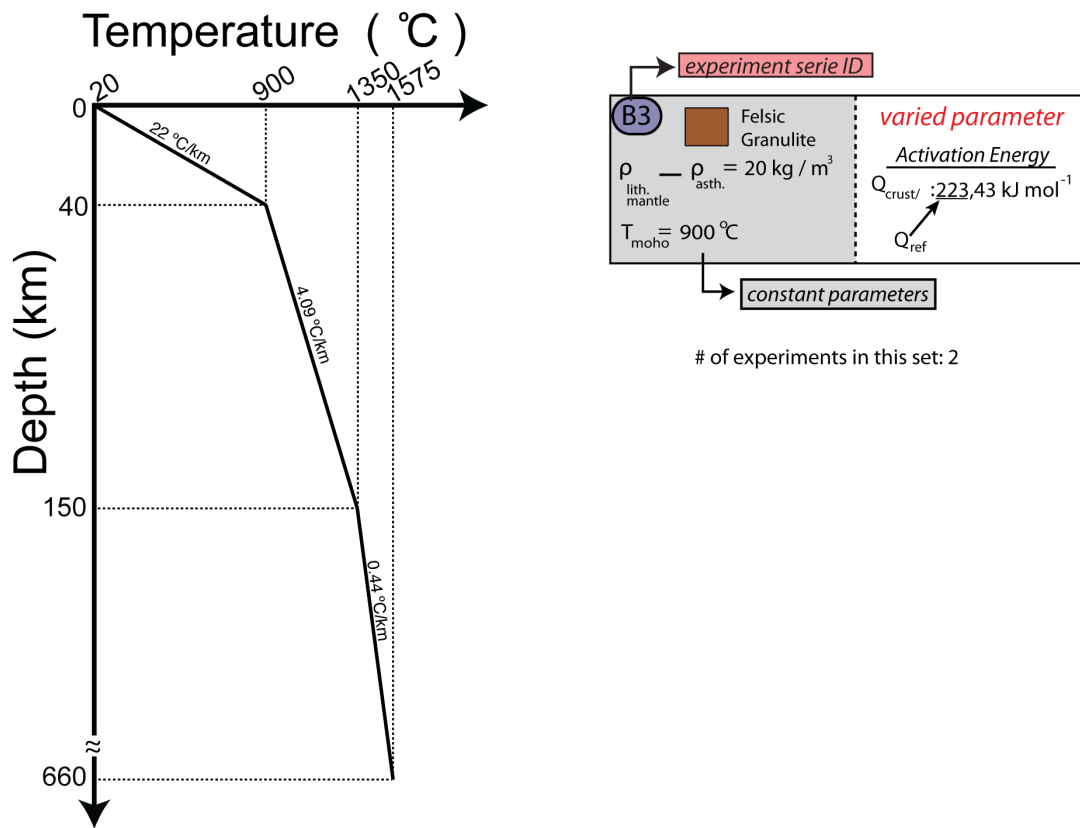


Figure 2.32. Model configuration and flow parameters for the materials of experimental set B3.

2.4.14. Results of B3

When the activation energy of the upper/middle crust is at its reference value (223 kJ/mol), though the lower crust is accumulated right on the axis of dripping instabilities, because the upper/middle crust is strong enough, the lower crust is not exhumed to the surface. The direct exposure to asthenospheric flow causes some heating of the lower crust in time. Most of the lithospheric mantle already drips down into the asthenospheric mantle.

If the activation energy of the upper/middle crust is decreased to 43 kJ/mol, the lower crust is accumulated in the centre of model domain during the dripping instability and continued convergence. After 1.6 Ma, the pressure of the rocks tracked from lower crust increase about 2 kbar at least and the temperature of these rocks decrease about 50 °C. The accumulation of lower crust is focused on the sides and centre of the model domain. This provides large amount of lower crust to be entrained by dripping lithospheric mantle in specific regions. After 6.4 Ma, the lower crust is exhumed to the surface well enough.

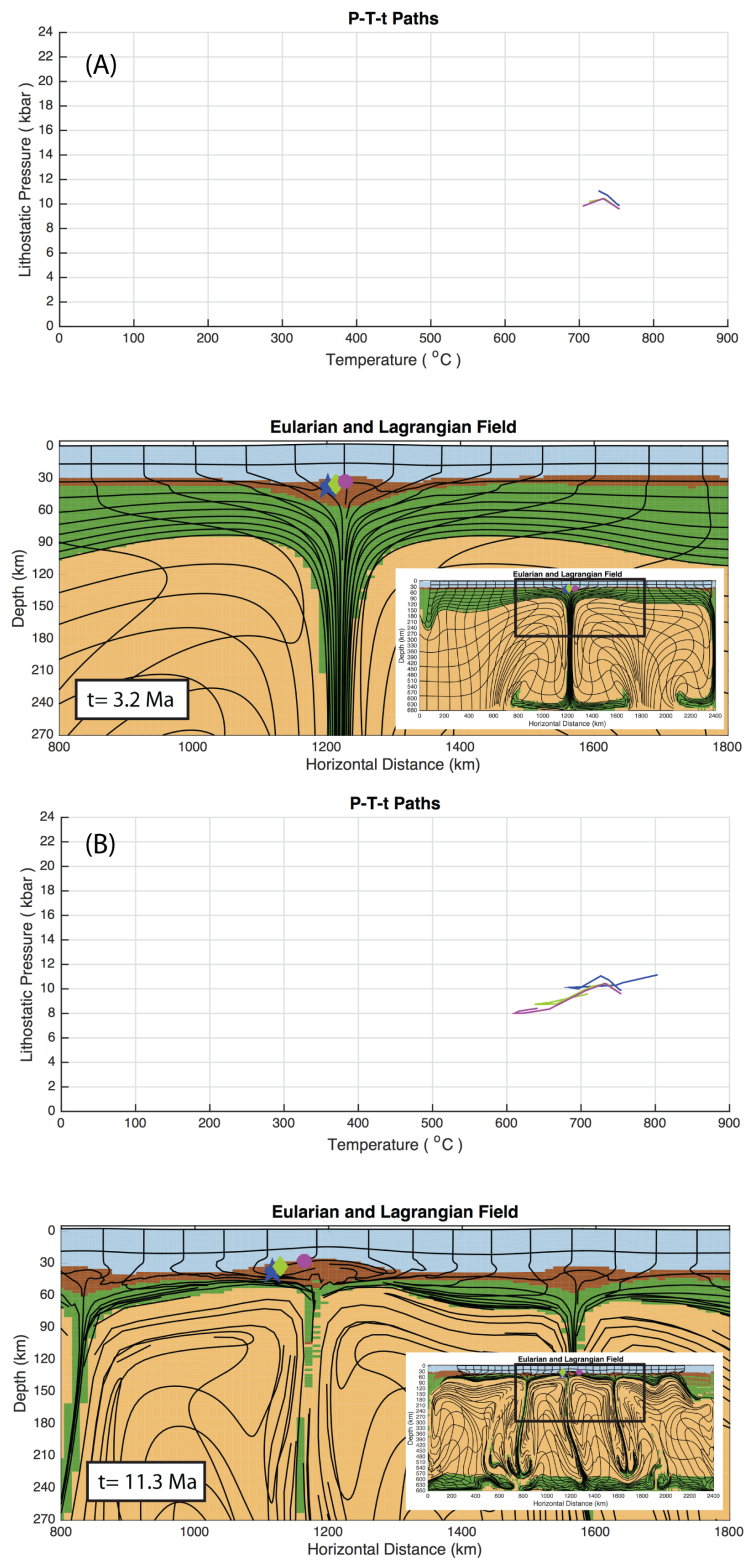


Figure 2.33. Model development and P-T-t paths of tracked particles of experiment B3 with activation energy of 223 kJ/mol in the u/m crust (A) after 3.2 Ma, (B) after 11.3 Ma. Blue: u/m crust, Brown: low. crust, Green: lith. mantle, Orange: asth.

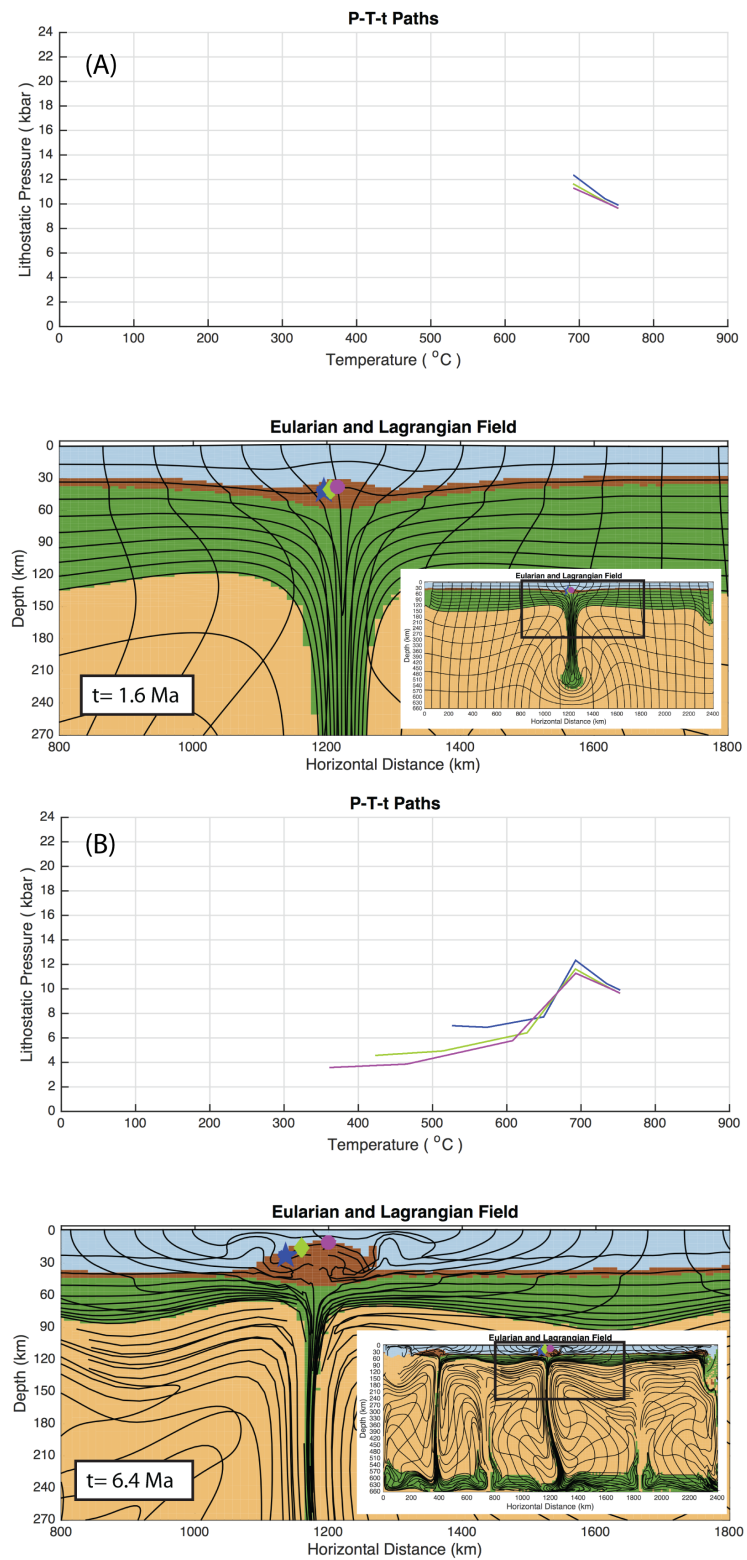


Figure 2.34. Model development and P-T-t paths of tracked particles of experiment B3 with activation energy of 43 kJ/mol in the u/m crust (A) after 1.6 Ma, (B) after 6.4 Ma. Blue: u/m crust, Brown: low. crust, Green: lith. mantle, Orange: asth.

2.5. Subduction of Oceanic Plate Under The Continental Margin

2.5.1. Experimental Set C1

In this set of experiments, the aim was to understand the dynamics of oceanic plate subduction and comprehend the connection between rheology, burial and exhumation of crustal rocks. As it can be seen from the configuration in Figure 2.58, an oceanic plate that has already started to subduct and two continental blocks were defined above the asthenospheric mantle. The convergence was given from right boundary. Oceanic and continental lithospheric mantle was imposed to deform in plastic rheology. The Moho temperature was set as 900 °C based on previous modelling experience and to simulate the upper limit for the temperature of granulite facies rocks. The convergence rate was increased from 0cm/yr with increments of 1cm/yr up to 5 cm/yr. The geotherms for oceanic and continental slabs were defined according to the thermal boundary level (LAB). The crust, asthenospheric mantle and weak zone deforms in visco-plastic rheology.

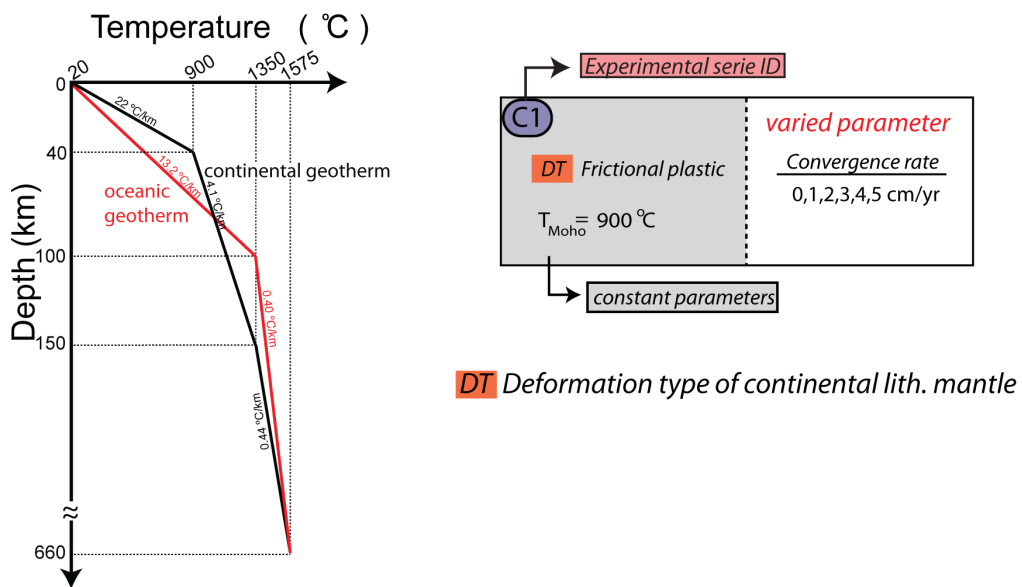
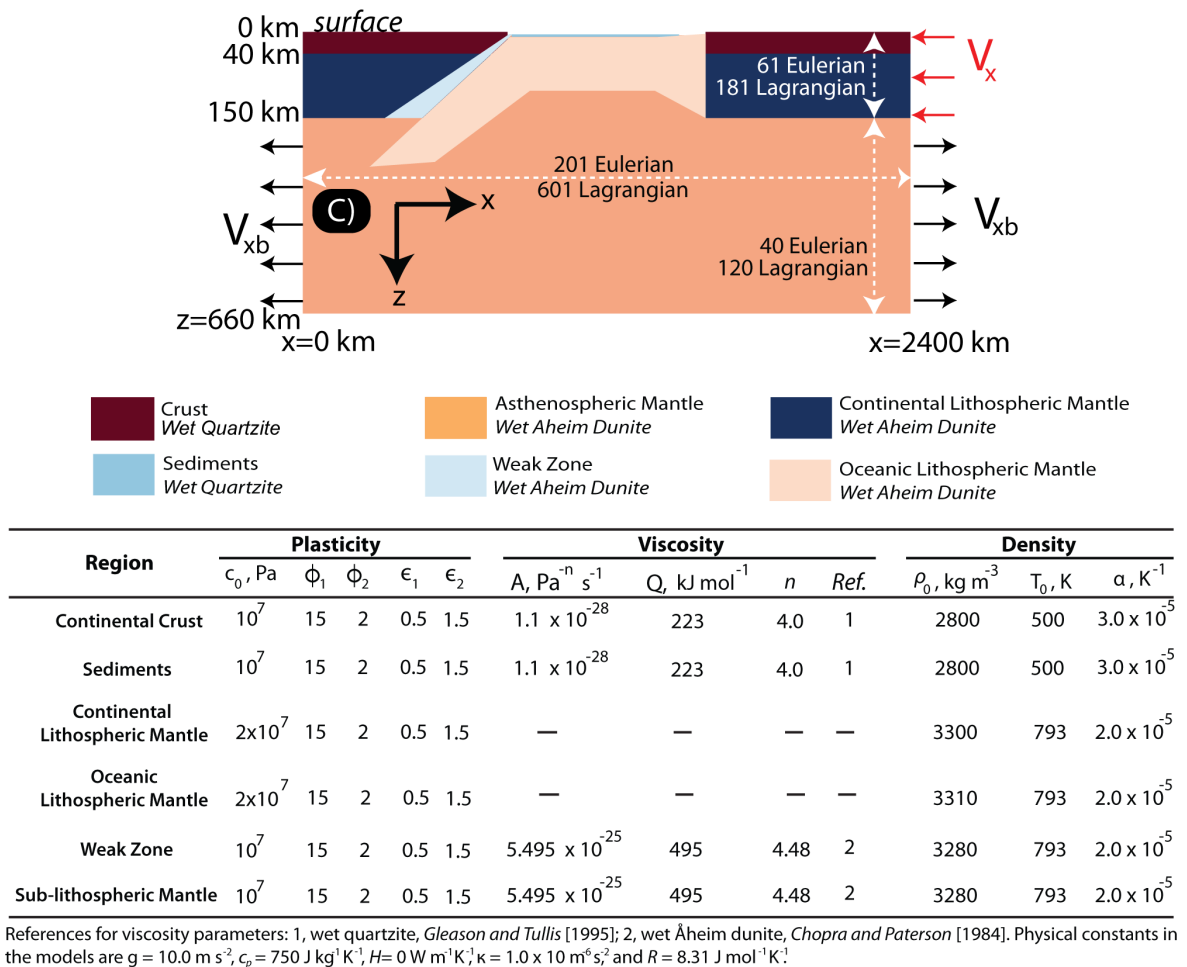


Figure 2.35. Model configuration and flow parameters for the materials of experimental set C1.

2.5.2. Results of C1

The rocks (lagrangian nodes in the numerical model) tracked from the pro-plate and retro-plate are shown with symbols of different colours in Figure 2.59.

When the convergence rate is 2 cm/yr, the rock originated from the lower crust of retro-plate is buried down to 60 km, and from the middle crust of retro-plate is buried to 30 km depths. The slab pull force applied by the denser oceanic lithosphere pulls the continental crust of the pro-plate to lower crustal depths, provided that these rocks are not buried into the subduction channel as for the rocks coming from retro-plate. After 25.7 Ma, the rocks originated from the retro- and pro-plates are not exhumed even though the oceanic slab detaches from the continental plate.

It is important to note that the rock designated by cyan diamond which originated from the retro-plate cools about 400 °C by advection of cold rocks on the surface of oceanic plate into the the subduction channel.

If the convergence rate is increased to 3 cm/yr, the rocks from retro- and pro-plate are buried to deeper levels in the same period of time compared to the previous numerical model. After 25.7 Ma, the rocks -except the ones designated by red, blue and black diamonds- exhume to the upper levels by the effect of buoyancy force. The subduction channel widens about 80 km, and asthenospheric intrusion is discerned from the model result in Figure 2.65.

Increasing the convergence rate to 4 cm/yr provides burial of crustal rocks from the retro-plate to depths of 93 km (red) and 75 km (cyan) in 12.9 Ma (Figure 2.67). The rocks from the pro-plate are buried to depths of 60 km (black), 54 km (green), 42 km (blue), and 32 km (orange). The positive buoyancy of crustal rocks push them to the middle-lower crustal levels after the opening of the subduction channel and subsequent intrusion of asthenospheric mantle into the subduction channel. The maximum pressure - temperature conditions for the rocks that are buried and exhumed to upper levels are: 29 kbar, 670 °C (red), 21 kbar, 660 °C (cyan), 18 kbar, 610 °C (black), 16

kbar, 550 °C (green), 13 kbar, 430 °C (blue) and 9 kbar, 350 °C (orange).

When the convergence rate is set as 5 cm/yr, not all of the rocks from the retro-plate are buried to deeper levels compared to the previous numerical model: 112 km for the rock designated with red diamond, and 66 km for the rock designated by cyan diamond. Some of the rocks from the pro-plate are also buried to higher depths. The model result show that the subduction channel widens about 100 km after 25.7 Ma. It is also important to note that delamination of continental crust from the lithospheric mantle develops in time after the exhumation of crustal rocks. The maximum pressure-temperature conditions for the rocks buried and exhumed to upper levels are: 35 kbar, 750 °C (red), 20 kbar, 660 °C (cyan), 13 kbar, 490 °C (green), 12 kbar, 440 °C (blue), and 10 kbar, 380 °C (orange).

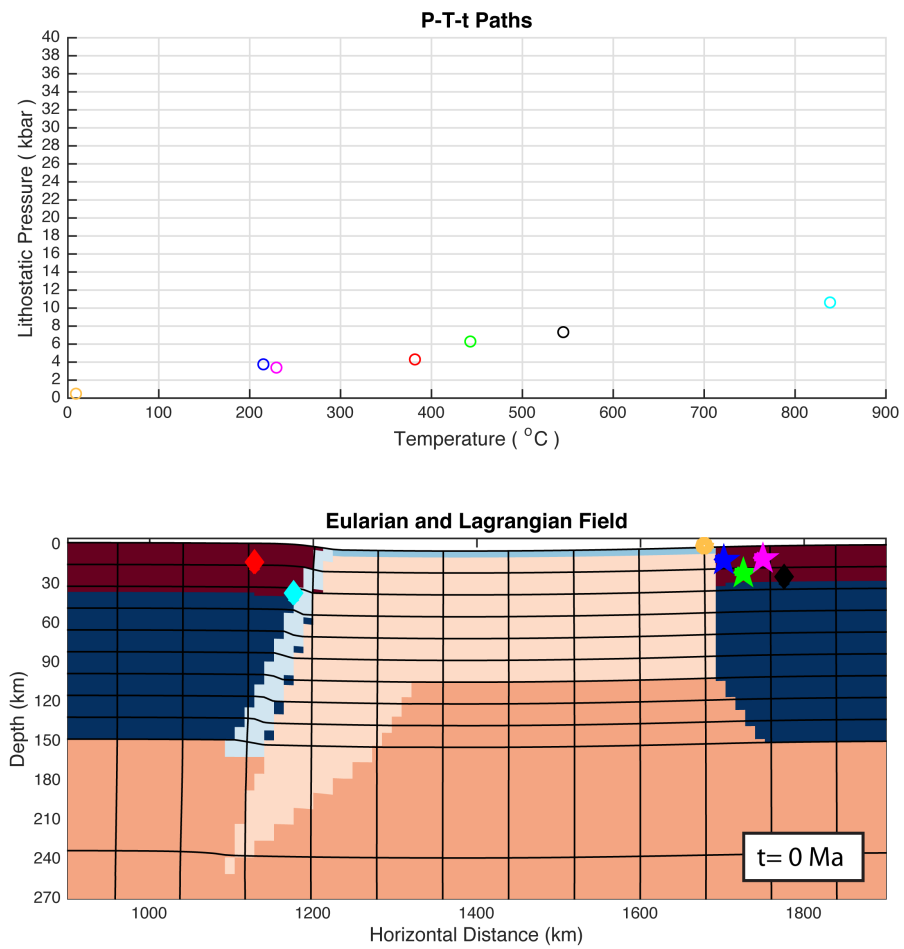


Figure 2.36. The positions of tracked lagrangian nodes (rocks) placed on the initial model configuration for the experimental set C1. Red: crust, Blue: continental lith. mantle, Yellow: oceanic lith. mantle, Orange: asthenosphere. Light Blue: weak zone.

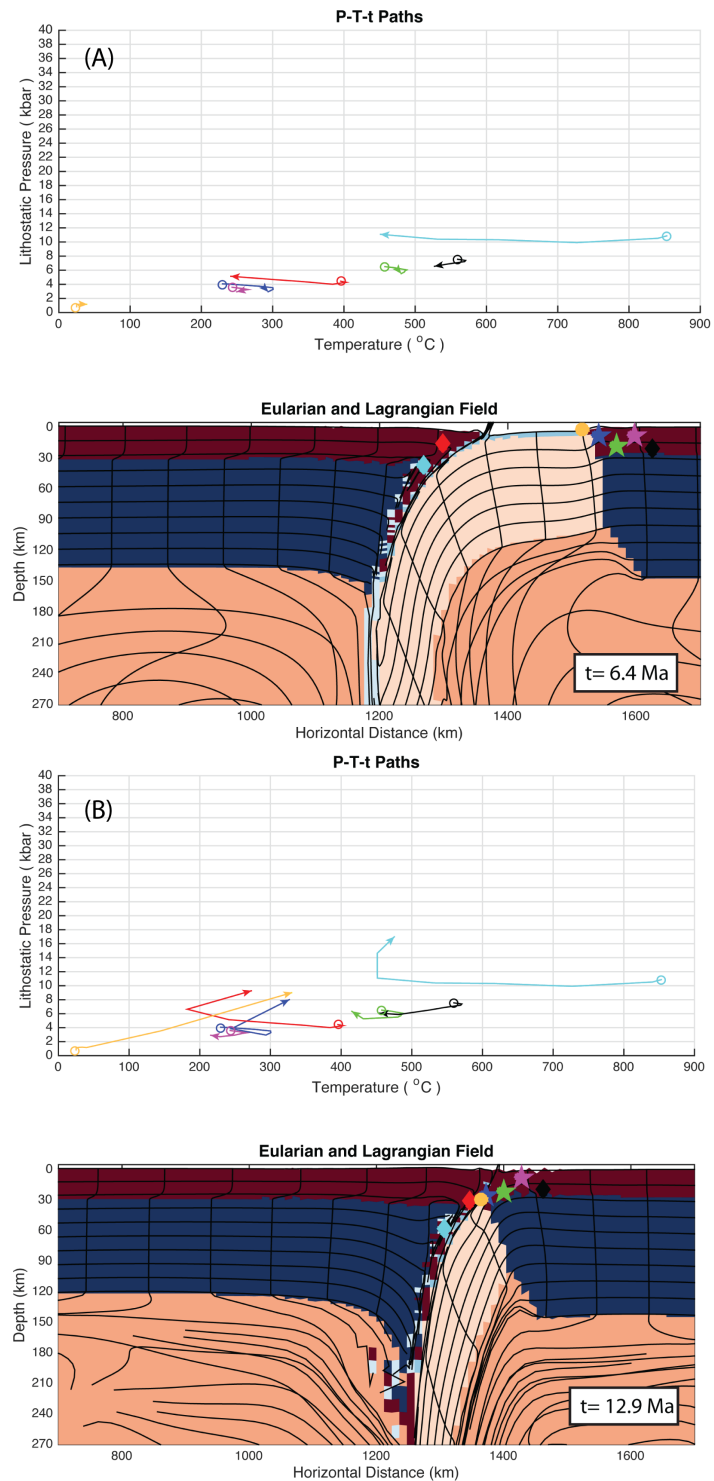


Figure 2.37. Model development and P-T-t paths of tracked particles of experiment C1 with convergence rate of 2 cm/yr (A) after 6.4 Ma, (B) after 12.9 Ma. Red: crust, Blue: continental lith. mantle, Yellow: oceanic lith. mantle, Orange: asthenosphere.

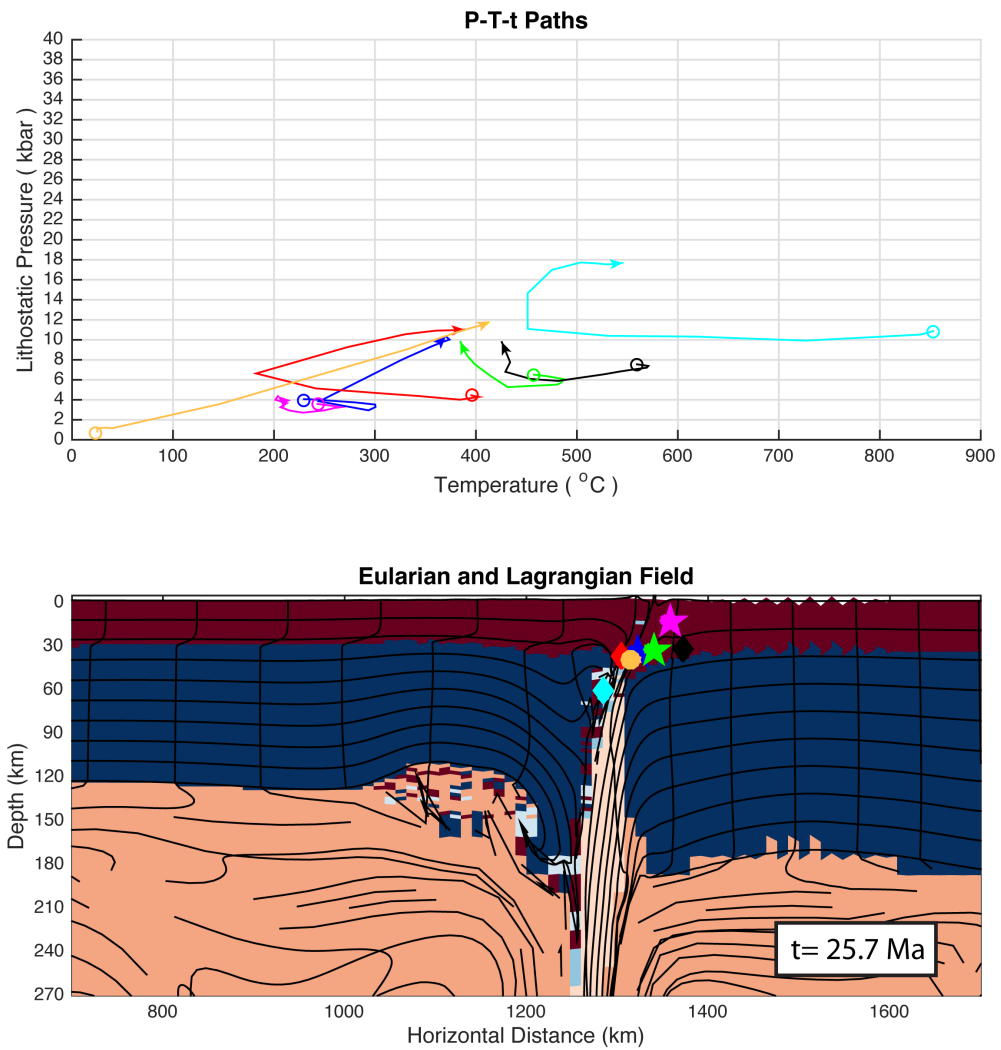


Figure 2.38. Model development and P-T-t paths of tracked particles of experiment C1 with convergence rate of 2 cm/yr after 25.7 Ma. Red: crust, Blue: continental lith. mantle, Yellow: oceanic lith. mantle, Orange: asthenosphere.

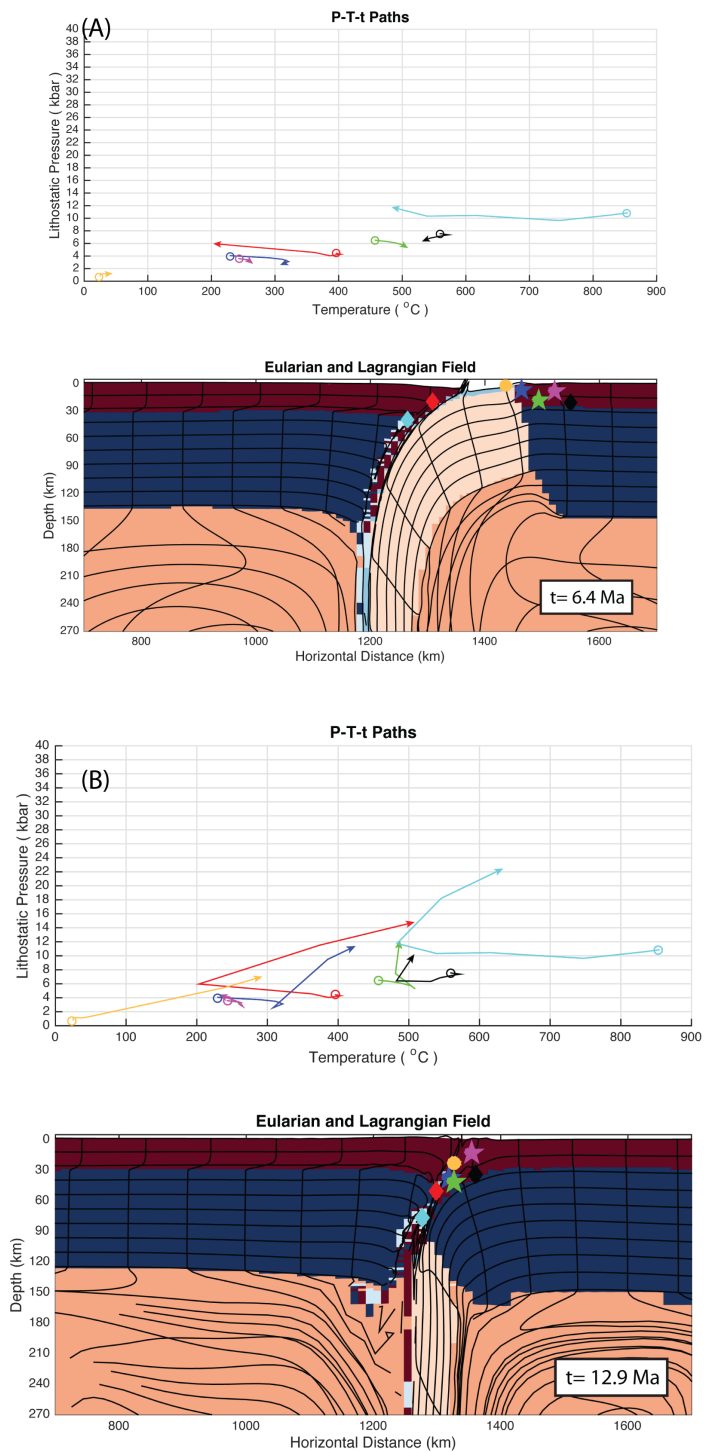


Figure 2.39. Model development and P-T-t paths of tracked particles of experiment C1 with convergence rate of 3 cm/yr (A) after 6.4 Ma, (B) after 12.9 Ma. Red: crust, Blue: continental lith. mantle, Yellow: oceanic lith. mantle, Orange: asthenosphere.

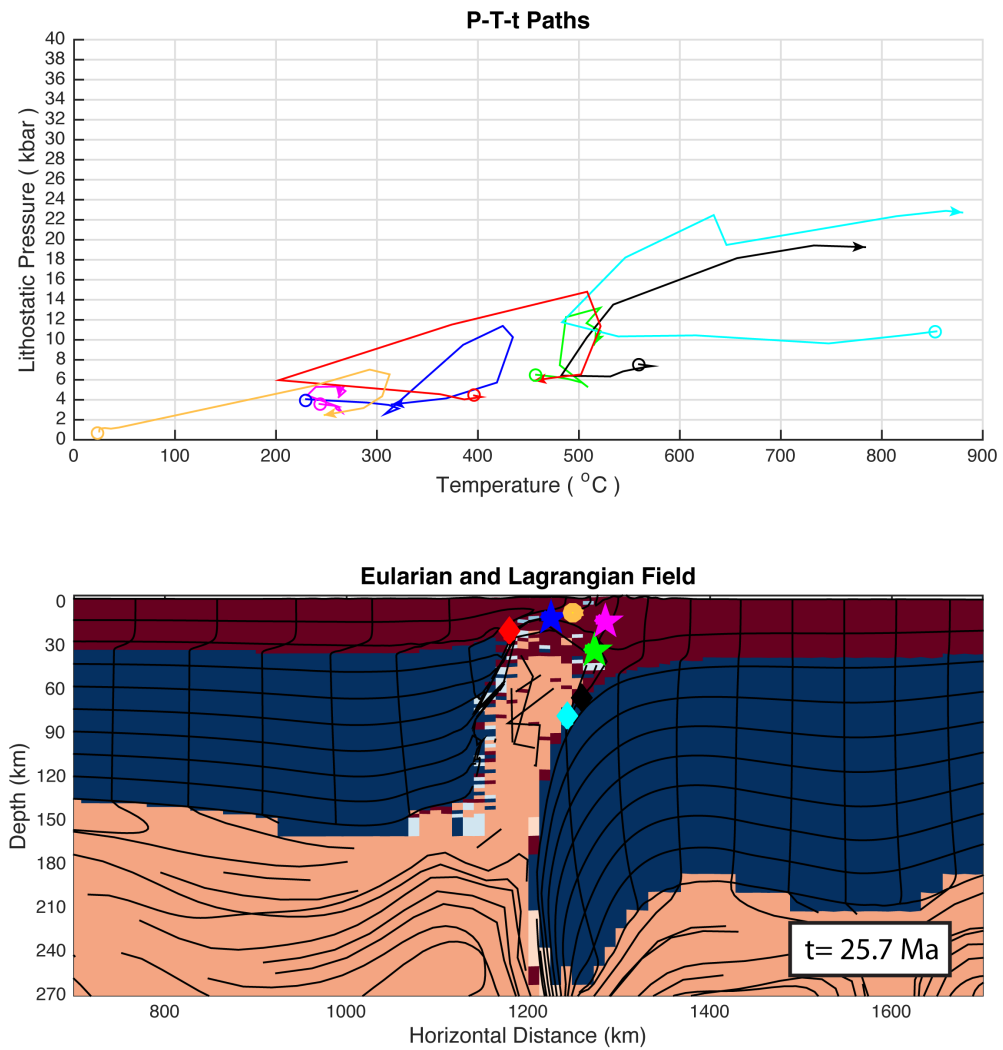


Figure 2.40. Model development and P-T-t paths of tracked particles of experiment C1 with convergence rate of 3 cm/yr after 25.7 Ma. Red: crust, Blue: continental lith. mantle, Yellow: oceanic lith. mantle, Orange: asthenosphere.

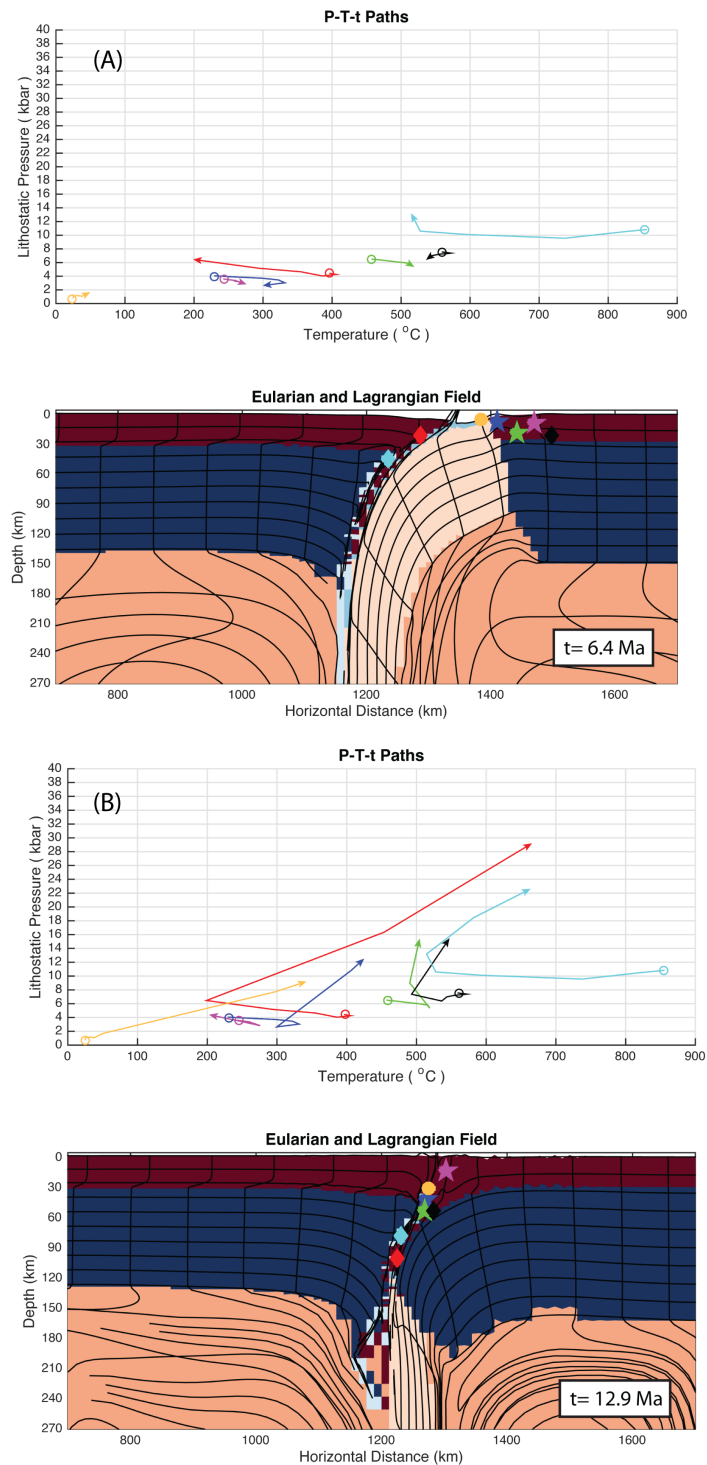


Figure 2.41. Model development and P-T-t paths of tracked particles of experiment C1 with convergence rate of 4 cm/yr (A) after 6.4 Ma, (B) after 12.9 Ma. Red: crust, Blue: continental lith. mantle, Yellow: oceanic lith. mantle, Orange: asthenosphere.

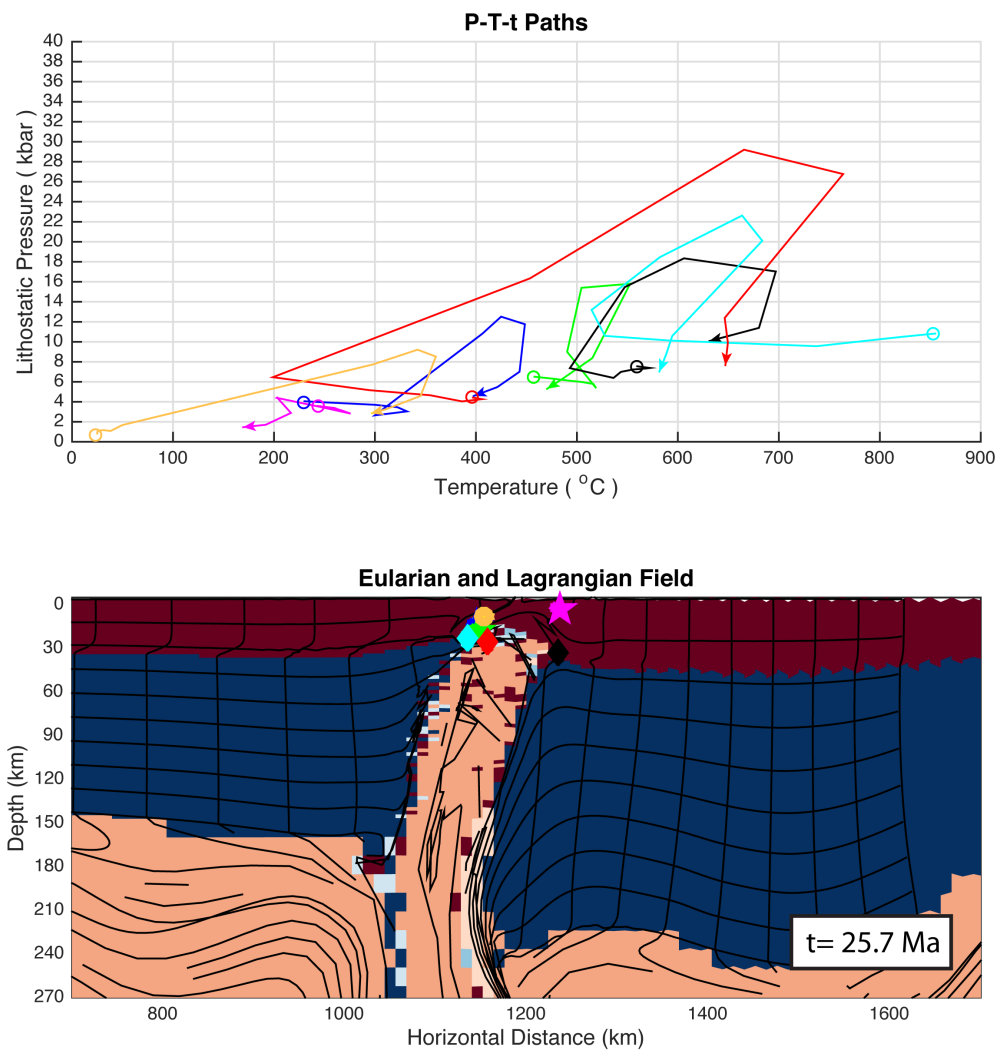


Figure 2.42. Model development and P-T-t paths of tracked particles of experiment C1 with convergence rate of 4 cm/yr after 25.7 Ma. Red: crust, Blue: continental lith. mantle, Yellow: oceanic lith. mantle, Orange: asthenosphere.

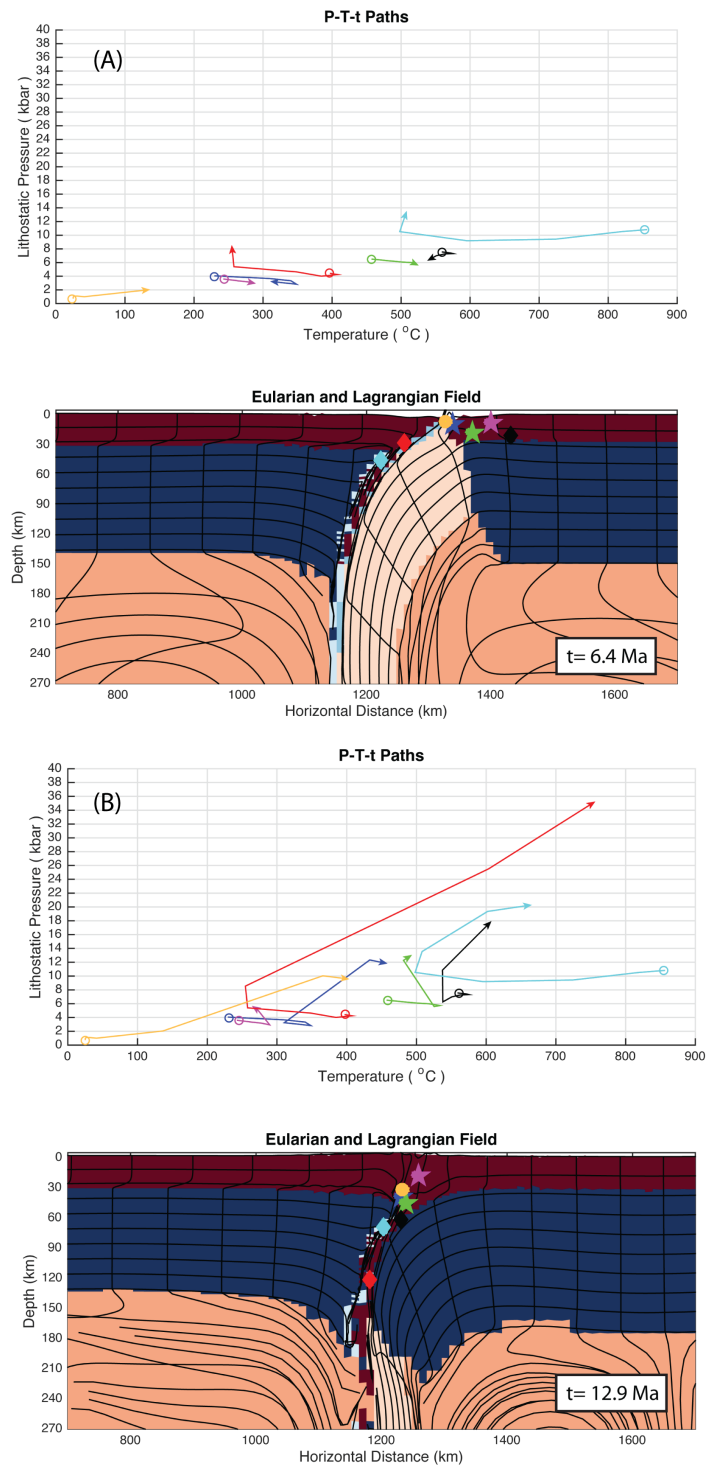


Figure 2.43. Model development and P-T-t paths of tracked particles of experiment C1 with convergence rate of 5 cm/yr (A) after 6.4 Ma, (B) after 12.9 Ma. Red: crust, Blue: continental lith. mantle, Yellow: oceanic lith. mantle, Orange: asthenosphere.

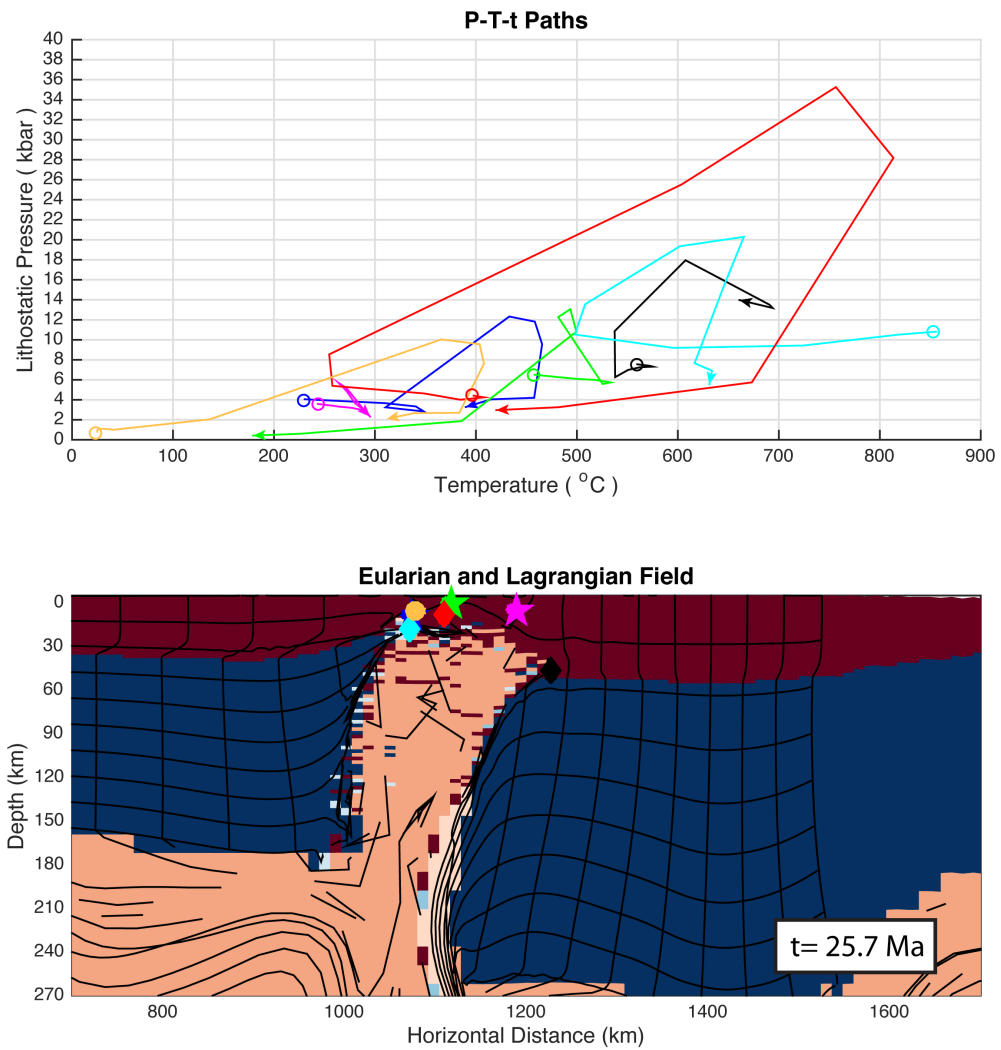


Figure 2.44. Model development and P-T-t paths of tracked particles of experiment C1 with convergence rate of 5 cm/yr after 25.7 Ma. Red: crust, Blue: continental lith. mantle, Yellow: oceanic lith. mantle, Orange: asthenosphere.

2.5.3. Experimental Set C2

In this configuration, the model geometry was kept the same as experimental set C1. The only difference is that the deformation type of continental lithospheric mantle was set as viscous (Newtonian) rather than frictional plastic. The convergence rate was increased starting from 0 cm/yr with 1cm/yr increments up to 3 cm/yr. The Moho temperature was kept the same as 900 °C.

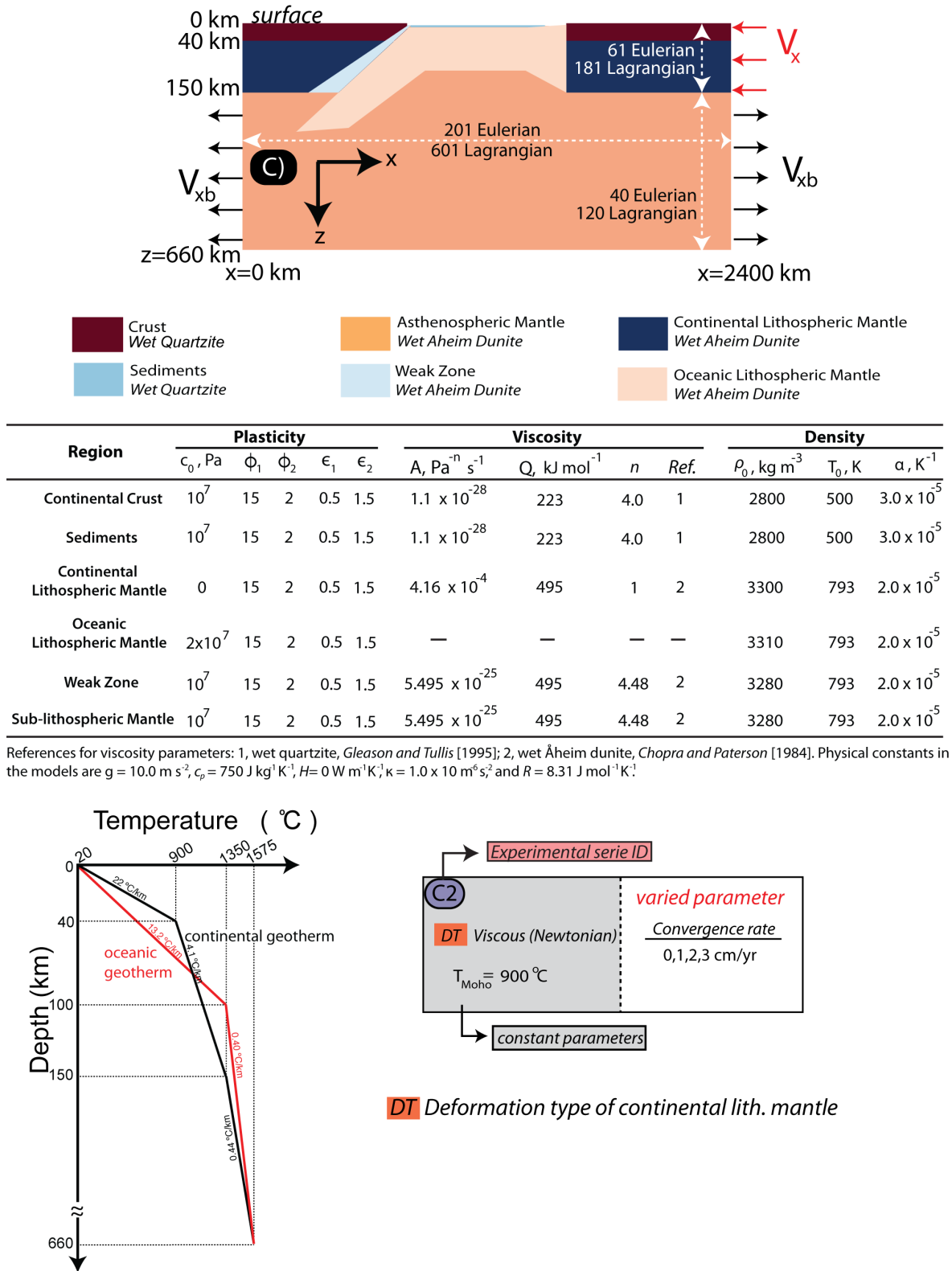


Figure 2.45. Model configuration and flow parameters for the materials of experimental set C2.

2.5.4. Results of C2

When the convergence rate is 0 cm/yr, there happens to be closure of subduction channel by flow of continental lithospheric mantle in the subduction channel. This is possible because of the nature of viscous rheology. In this tectonic setting, subduction channel flow is one of the major mechanism controlling the tectonics in crustal depths. The rocks from the retro-plate follow a circular path that can be discerned from the lagrangian mesh and P-T-t paths of rocks designated by black, cyan and red diamonds (Figure 2.75). Among the rocks originated from retro-plate, the rock designated by black diamond already exhumes to the surface at a time all other rocks are in the process of burial. This -polyphase exhumation- is one of the consequences of subduction channel flow process.

The rocks originated from the pro-plate are buried in a narrow channel, to the south of the thrust fault that formed during subduction process (Figure 2.75). The deeper rocks (originated from lower crust) are buried ahead of the other rocks (originated from upper/middle crust). After 9.7 Ma, the oceanic slab is still in connection with the continental lithospheric mantle. The rocks of pro-plate are buried to 72 km (green), 51 km (blue), 45 km (orange) and 32 km (magenta) depths. The maximum pressure - temperature conditions for these rocks are are: 22 kbar, 620 °C (green), 15 kbar, 470 °C (blue), 13 kbar, 380 °C (orange) and 9 kbar, 380 °C (magenta).

After detachment of the oceanic slab, the buried rocks exhume to the upper levels by force-release effect. The model results show that rocks originated from the retro-plate are exhumed more efficiently than the rocks coming from pro-plate. It is clear that the subduction channel flow process is more affective than slab break-off/eduction mechanism in the sense that rocks subjected to this mechanism are exhumed to higher levels than the others. However, in this tectonic setting, burial depth is higher when rocks are subjected to slab-pull force rather than subduction channel flow mechanism.

When the convergence rate is 1 cm/yr, the rock coming from the pro-plate is buried to 130 km depth, but at later stages, this rock can not exhume back to the

upper levels. Some of the rocks of pro-continent are buried to higher depths compared to the previous numerical model: 54 km (blue), 35 km (magenta). The sedimentary rock designated by orange circle is not buried to significant depths, because it was thrust on the surface of the continental crust just after the closure of the ocean. After detachment of the oceanic slab, though there is still ongoing continental subduction, the rocks are exhumed to the upper levels by the force-release mechanism. The recorded maximum pressure - temperature conditions for the rocks buried and exhumed are: 16 kbar, 490 °C (blue), 13 kbar, 680 °C (black), 11 kbar, 380 °C (magenta), 9 kbar, 360 °C (red), and 8 kbar, 380 °C (cyan).

If the convergence rate is increased to 2 cm/yr, the burial depth of some of the pro-plate rocks increase as well. The rock designated by green star is buried down to 160 km depth, but this rock can not achieve to exhume to the upper levels. The rocks originated from retro-plate shows similar P-T-t paths with previous numerical model. It is important to note that though the maximum pressure values are similar for the rocks originated from pro-plate, the temperature values are lower about 60 °C. This shows that the amount of rocks buried into the channel was higher in this numerical model compared to the previous one. After the detachment of the oceanic slab from the continental lithosphere, the rocks exhume to the upper levels. The recorded maximum pressure - temperature conditions for these rocks are as follows: 16 kbar, 430 °C (blue), 12 kbar, 690 °C (black), 11 kbar, 350 °C (magenta), 10 kbar, 320 °C (red), and 9 kbar, 390 °C (cyan).

When the convergence rate is 3 cm/yr, most of the rocks originated from pro-plate are buried to lower depths than the previous numerical model. On the other hand, the rock designated by green star is buried down to 170 km depth, but this rock can not achieve to exhume back to the upper levels. The higher depth burial of this rock is the fingerprint for higher convergence rate, whereas increasing the convergence rate does not have similar results for the upper/middle crust. In other words, for convergence rate greater than 2 cm/yr, the lower crust is the only part of pro-plate that is continuously being buried down to mantle depths. The recorded maximum pressure - temperature conditions for the rocks buried and exhumed to the upper levels are as follows: 13

kbar, 430 °C (blue), 11 kbar, 720 °C (black), 9 kbar, 360 °C (magenta), 7 kbar, 280 °C (red), and 7 kbar, 410 °C (cyan).

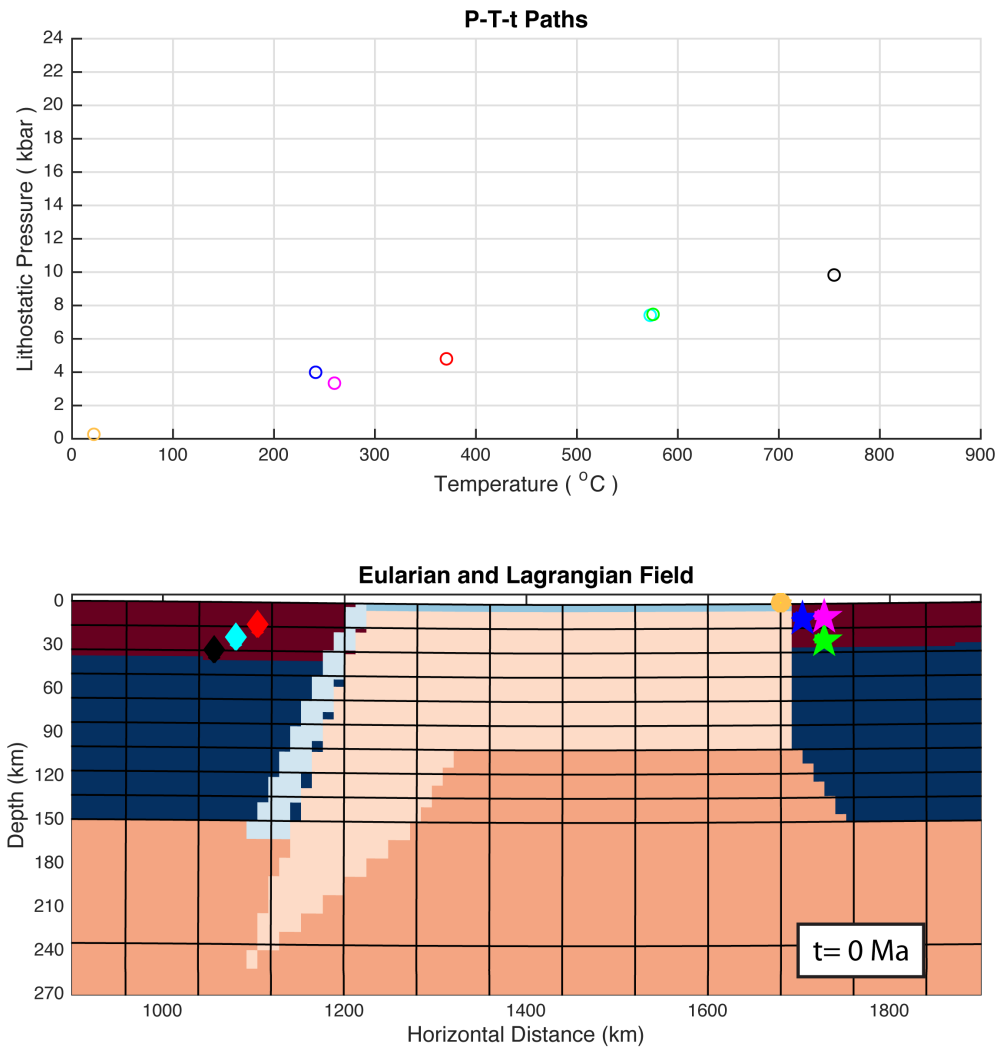


Figure 2.46. The positions of tracked lagrangian nodes (rocks) placed on the initial model configuration for the experimental set C2. Red: crust, Blue: continental lith. mantle, Yellow: oceanic lith. mantle, Orange: asthenosphere. Light Blue: weak zone.

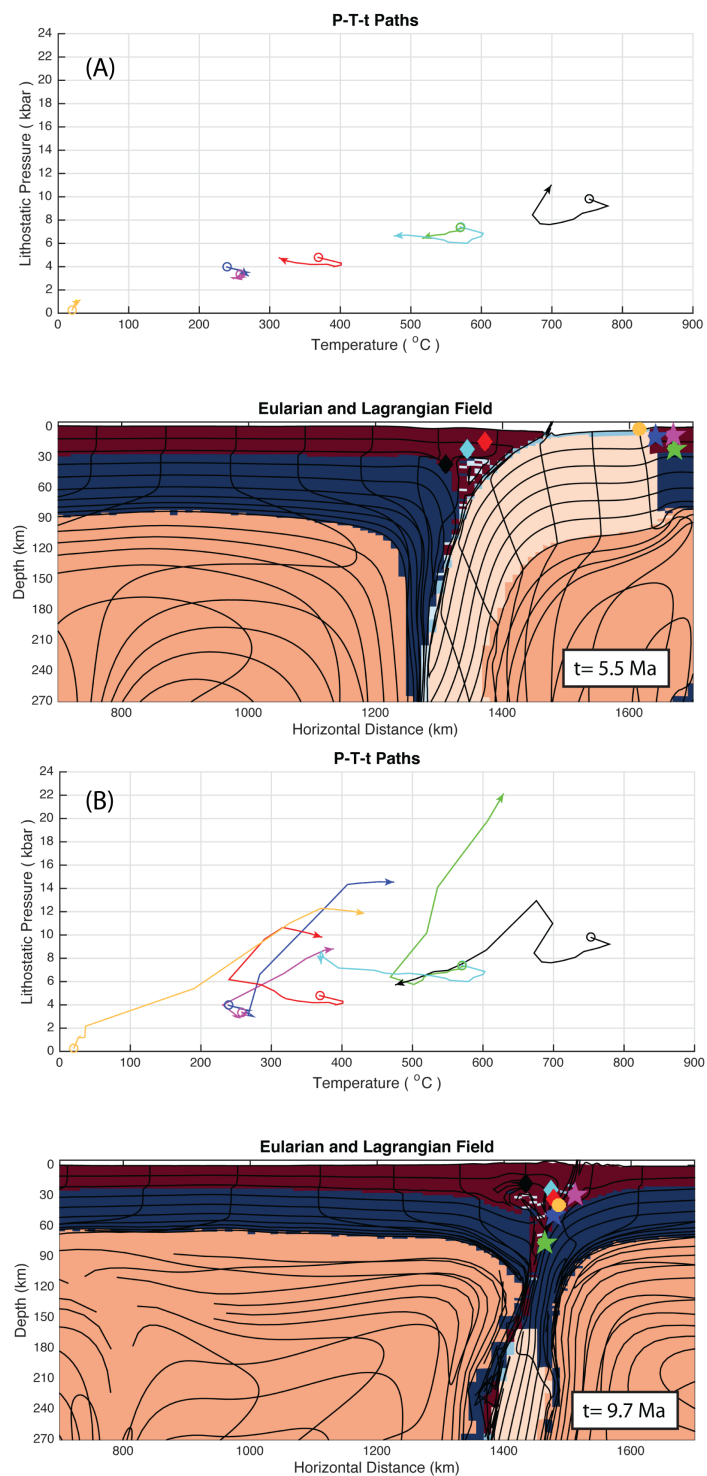


Figure 2.47. Model development and P-T-t paths of tracked particles of experiment C2 with convergence rate of 0 cm/yr (A) after 5.5 Ma, (B) after 9.7 Ma. Red: crust, Blue: continental lith. mantle, Yellow: oceanic lith. mantle, Orange: asthenosphere.

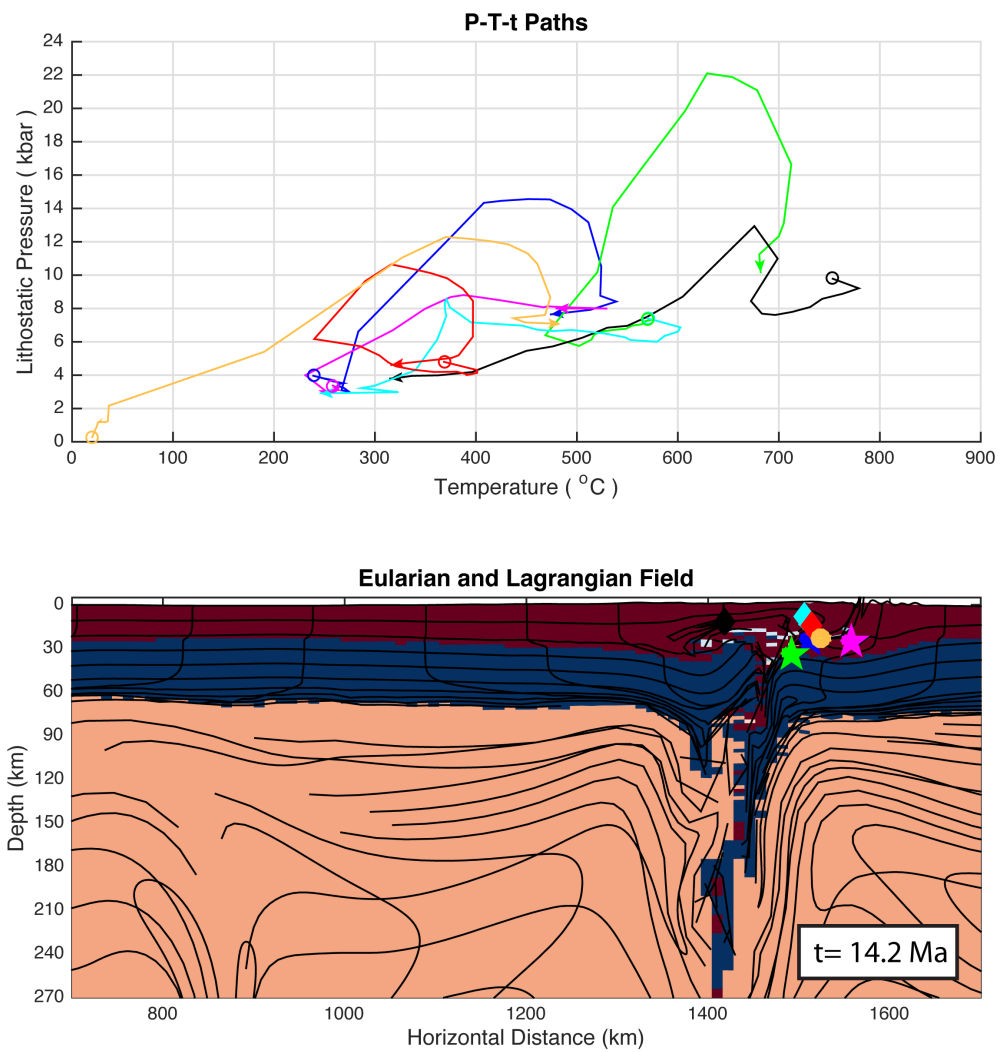


Figure 2.48. Model development and P-T-t paths of tracked particles of experiment C2 with convergence rate of 0 cm/yr after 14.2 Ma. Red: crust, Blue: continental lith. mantle, Yellow: oceanic lith. mantle, Orange: asthenosphere.

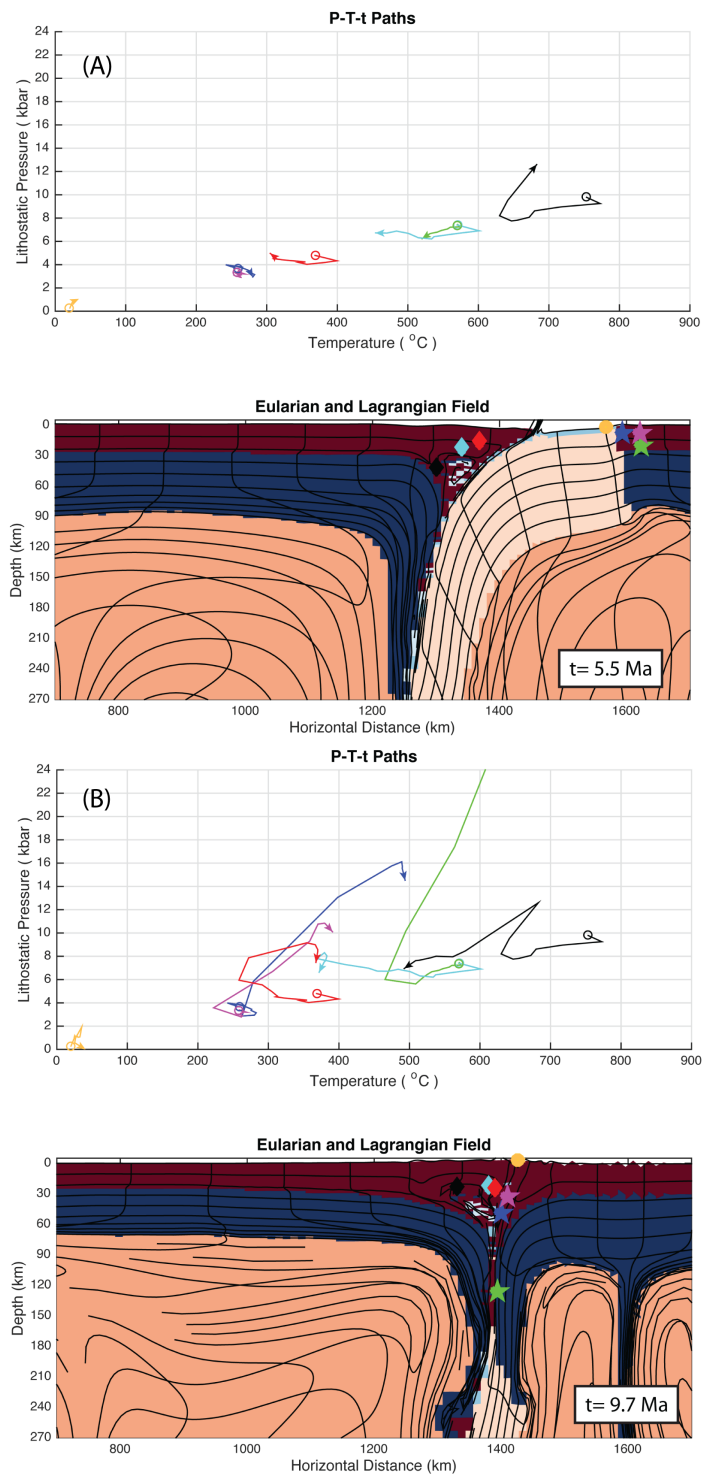


Figure 2.49. Model development and P-T-t paths of tracked particles of experiment C2 with convergence rate of 1 cm/yr (A) after 5.5 Ma, (B) after 9.7 Ma. Red: crust, Blue: continental lith. mantle, Yellow: oceanic lith. mantle, Orange: asthenosphere.

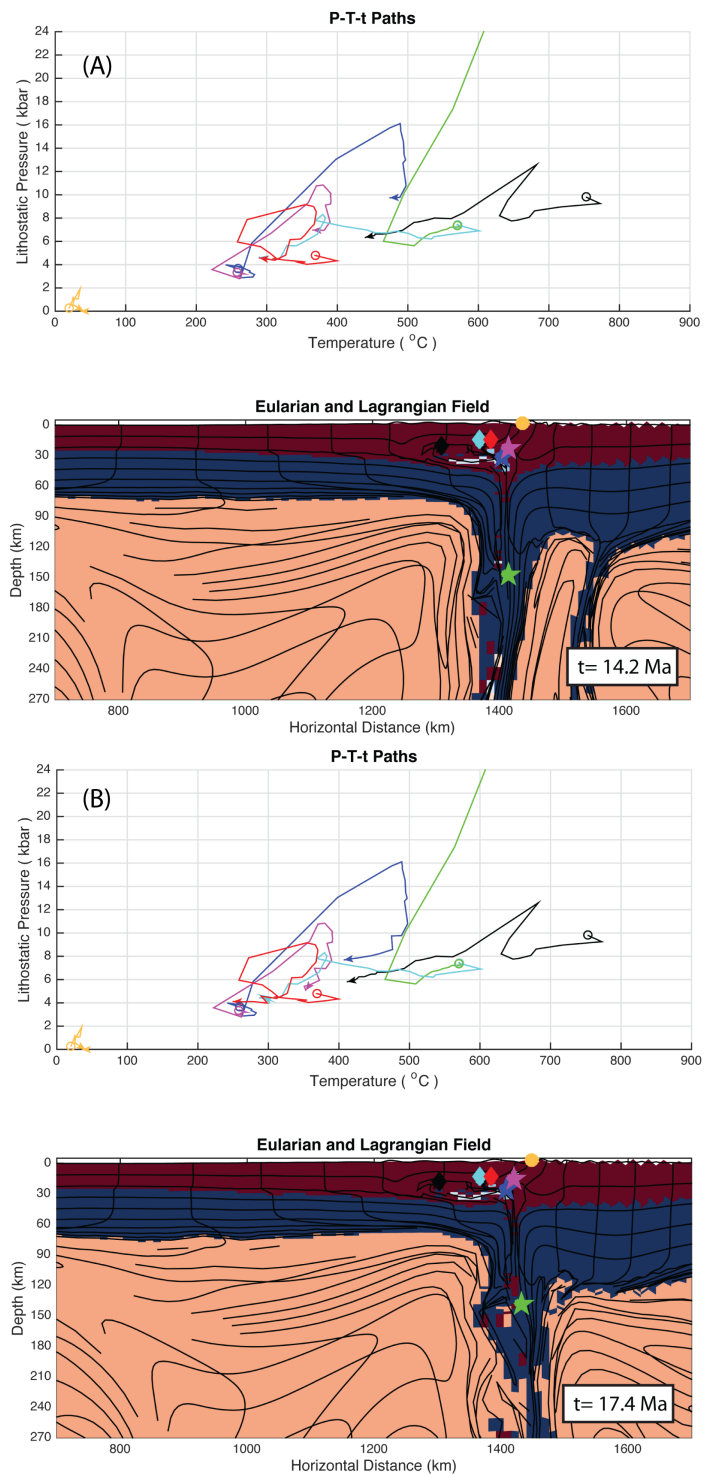


Figure 2.50. Model development and P-T-t paths of tracked particles of experiment C2 with convergence rate of 1 cm/yr (A) after 14.2 Ma, (B) after 17.4 Ma. Red: crust, Blue: continental lith. mantle, Yellow: oceanic lith. mantle, Orange: asth.

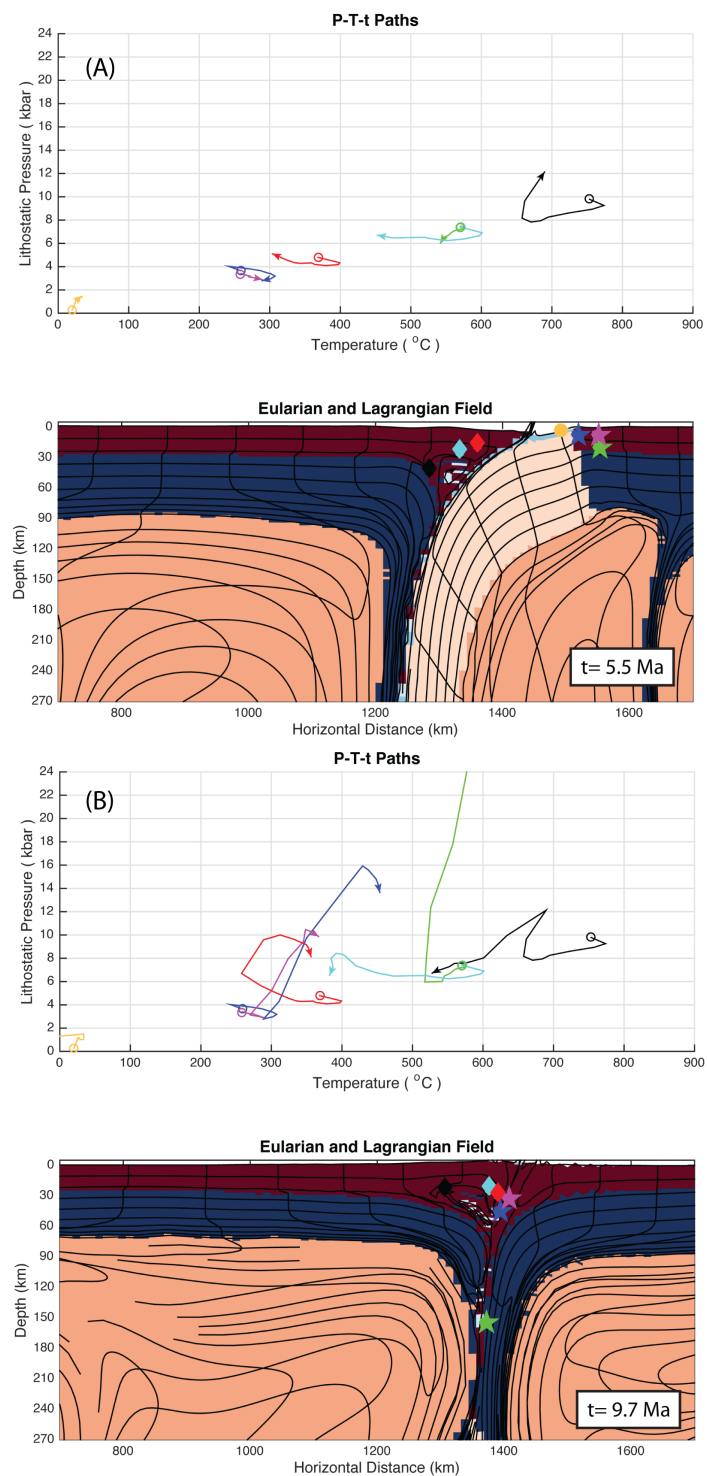


Figure 2.51. Model development and P-T-t paths of tracked particles of experiment C2 with convergence rate of 2 cm/yr (A) after 5.5 Ma, (B) after 9.7 Ma. Red: crust, Blue: continental lith. mantle, Yellow: oceanic lith. mantle, Orange: asthenosphere.

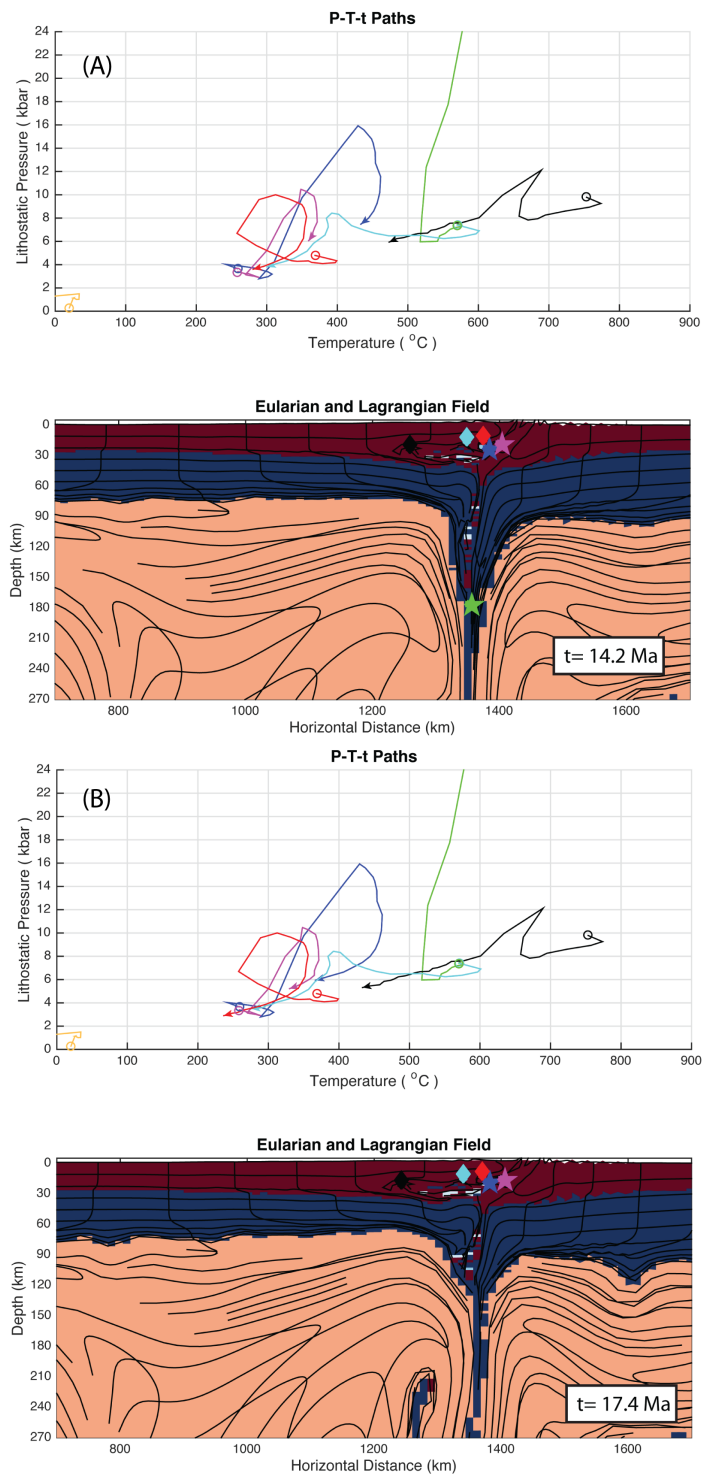


Figure 2.52. Model development and P-T-t paths of tracked particles of experiment C2 with convergence rate of 2 cm/yr (A) after 14.2 Ma, (B) after 17.4 Ma. Red: crust, Blue: continental lith. mantle, Yellow: oceanic lith. mantle, Orange: asth.

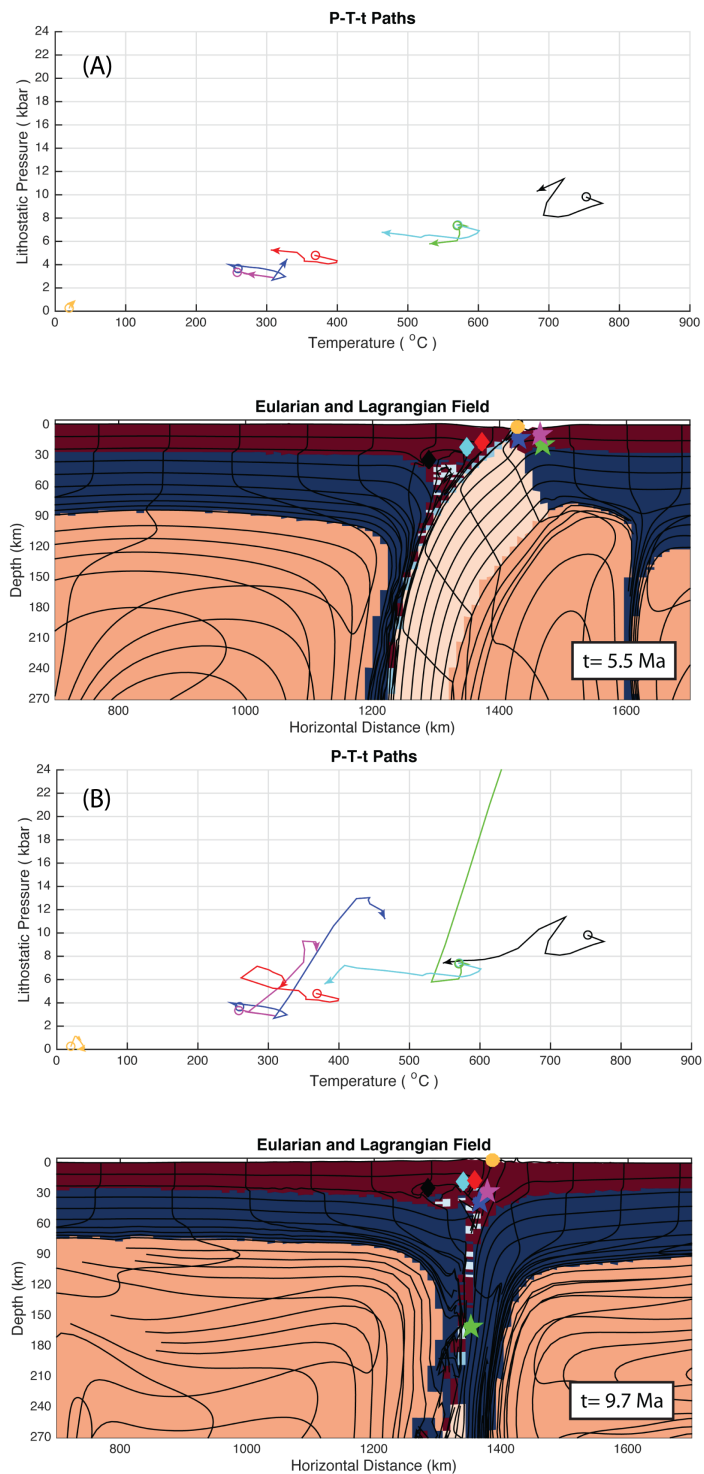


Figure 2.53. Model development and P-T-t paths of tracked particles of experiment C2 with convergence rate of 3 cm/yr (A) after 5.5 Ma, (B) after 9.7 Ma. Red: crust, Blue: continental lith. mantle, Yellow: oceanic lith. mantle, Orange: asthenosphere.

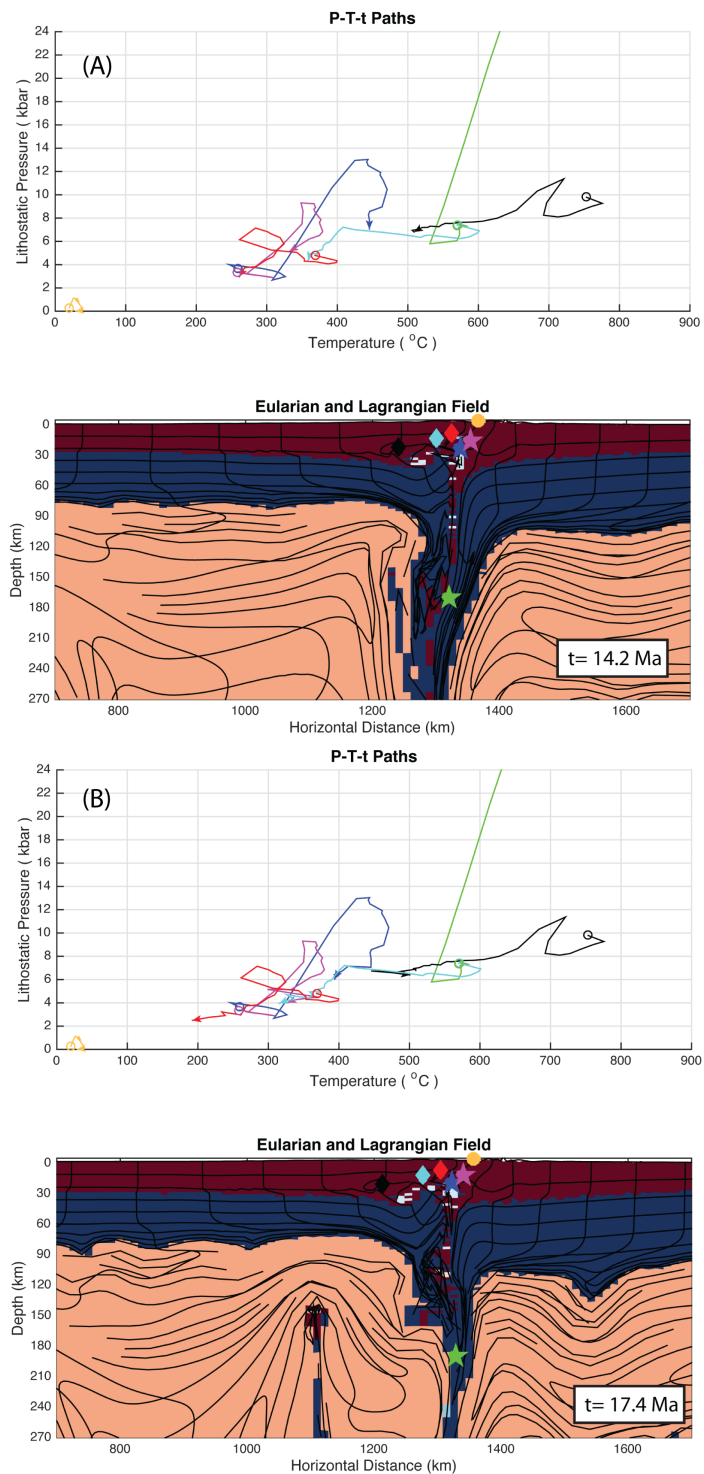


Figure 2.54. Model development and P-T-t paths of tracked particles of experiment C2 with convergence rate of 3 cm/yr (A) after 14.2 Ma, (B) after 17.4 Ma. Red: crust, Blue: continental lith. mantle, Yellow: oceanic lith. mantle, Orange: asth.

2.5.5. Experimental Set C3

In this configuration, the model geometry was kept the same as experimental set C1 and C2. The deformation type of continental lithospheric mantle kept as viscous (Newtonian) rather than frictional plastic. The aim of this experimental set is to identify the effect of activation energy of the crust to the burial and exhumation process in this tectonic configuration. The convergence rate was increased starting from 0 cm/yr with 1cm/yr increments up to 3 cm/yr. The Moho temperature was kept the same as 900 °C.

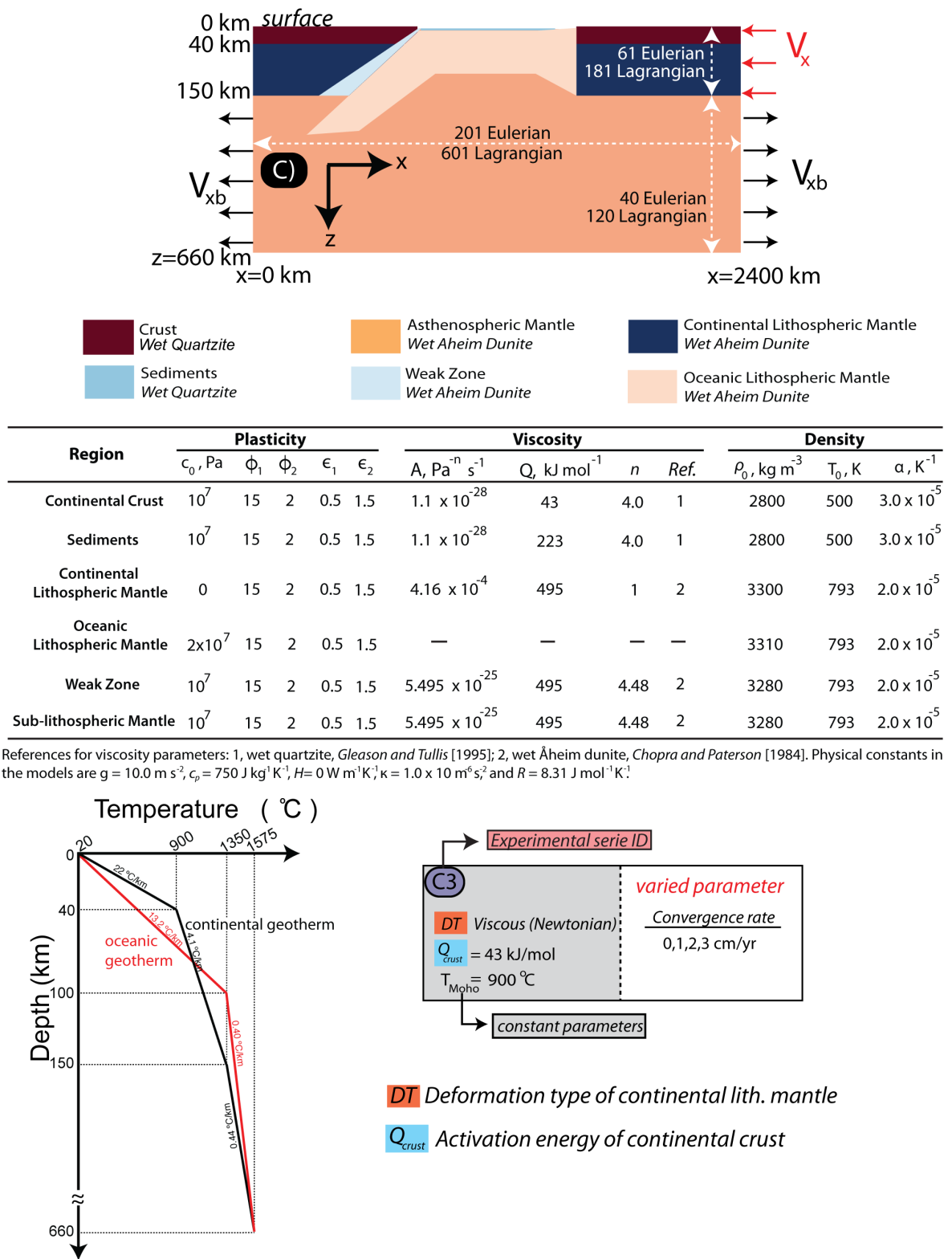


Figure 2.55. Model configuration and flow parameters for the materials of experimental set C3.

2.5.6. Results of C3

When the convergence rate is 0 cm/yr, in other words, the dynamics are driven by the slab-pull force acting in the downward direction, the process of subduction channel flow is well observed in the sense that the rocks circulate like a washing machine in a V shape like channel. The high amount of deformation that can be seen from the lagrangian mesh. After 4.8 Ma, the rocks originated from retro-plate are buried down to 84 km depth. The rock designated by black diamond already exhumes to 17 km depth, which means that polyphase exhumation is clearly reobserved. The sedimentary rock is thrust on to the continental crust just after the closure of the ocean. After 6.8 Ma, the rocks originated from pro-plate are buried down to 90 km depth, but at later stages, these rocks can not achieve to exhume to upper levels. Significant extension in the crust causes rifting in the retro-plate as can be shown in Figure 2.92. After the detachment of the oceanic slab from the continental lithospheric mantle, the rocks exhume to the upper levels. The maximum pressure - temperature values for the rocks that are buried and exhume to the upper levels are as follows: 26 kbar, 440 °C (red), 17 kbar, 620 °C (black), 13 kbar, 380 °C (cyan), and 10 kbar, 380 °C (magenta).

If the convergence rate is increased to 1 cm/yr, after 4.8 Ma, the rock originated from middle crust of retro-plate is buried to 90 km depth, which is deeper from the previous numerical model. Despite significant burial, this rock can not achieve to exhume to the crustal depths at later stages of model development. Similar notable level of burial is observed for the rocks designated by blue and green star, added to which the failure of exhumation is typical for these rocks in this tectonic configuration. After the detachment of oceanic slab from the continental lithosphere, the rocks exhume to crustal depths. Among these rocks, the one specified by cyan diamond, a middle-lower crustal rock of retro-plate, already exhumes to the surface at a time when other rocks are still being buried (Figure 2.95). The maximum pressure - temperature conditions for rocks that show notable burial and exhumation are as follows: 16 kbar, 460 °C (cyan), 15 kbar, 590 °C (black), and 13 kbar, 430 °C (magenta).

The numerical model results show that increasing the convergence rate to 2 cm/yr

enhances the burial depth of rock originated from upper crust of retro-plate. After 4.8 Ma, this rock is buried down to 93 km depth, however it can not achieve to exhume to crustal depths. At this period of time, the rock originated from lower crust of retro-plate already exhumes to 10 km depth. The rock originated from pro-plate that shows both notable burial and exhumation is the one designated by magenta star. The other rocks can be accounted as exhumed rocks come mostly from the retro-plate in this setting. The maximum pressure - temperature conditions for these rocks are as follows: 16 kbar, 700 °C (black), 12 kbar, 350 °C (cyan), and 10 kbar, 350 °C (magenta).

When the convergence rate is set as 3 cm/yr, the rock originated from the upper crust of pro-plate shows striking burial and exhumation pattern. The rocks that are circulating in the subduction channel flow are pushed to upper levels rapidly and in a linear path. This mechanism is called plunger-driven exhumation [35] in which entrance of colder or stronger continental interior material into the subduction channel drives weaker/hotter margin material to the upper level, and the weak/hotter crust is expelled out of the channel by continuous and rapid exhumation. The maximum pressure - temperature values of rocks that show notable burial and exhumation are as follows: 21 kbar, 50 °C (blue), 22 kbar, 490 °C (cyan), and 16 kbar, 720 °C (black).

In this numerical model the rocks that show notable exhumation reside on the retro-plate, no matter where they originated. Interestingly, the buoyant crust that is already buried to mantle depths reach to the lithospheric mantle depths and cause rifting on the retro-plate.

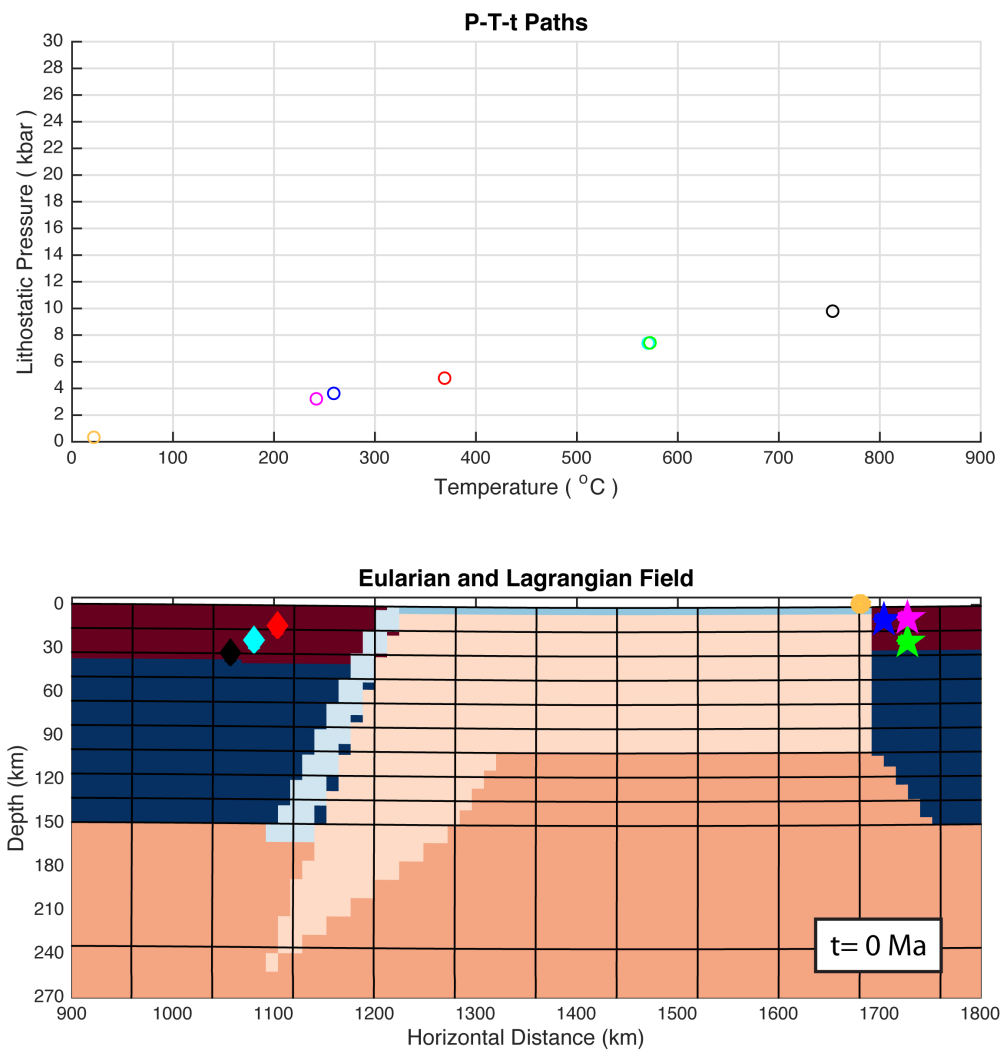


Figure 2.56. The positions of tracked lagrangian nodes (rocks) placed on the initial model configuration for the experimental set C3. Red: crust, Blue: continental lith. mantle, Yellow: oceanic lith. mantle, Orange: asthenosphere. Light Blue: weak zone.

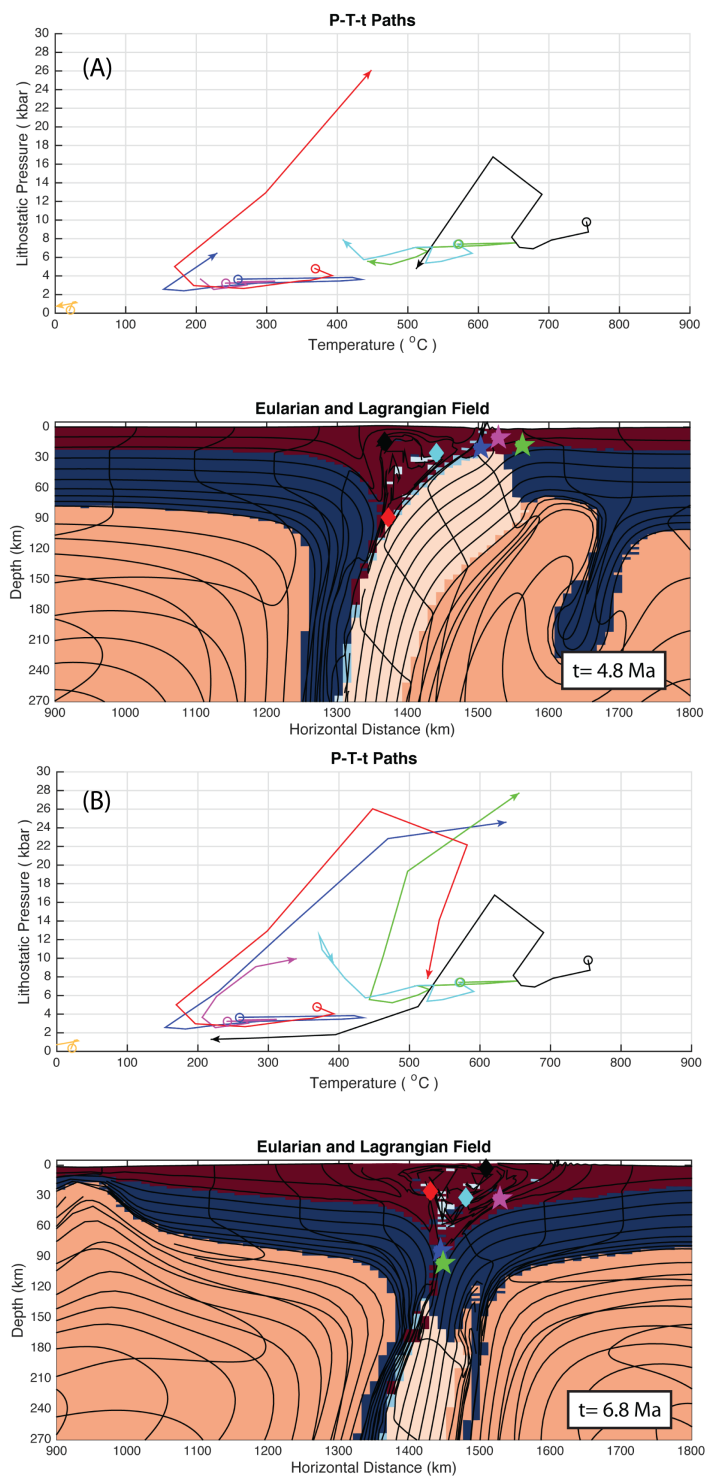


Figure 2.57. Model development and P-T-t paths of tracked particles of experiment C3 with convergence rate of 0 cm/yr (A) after 4.8 Ma, (B) after 6.8 Ma. Red: crust, Blue: continental lith. mantle, Yellow: oceanic lith. mantle, Orange: asthenosphere.

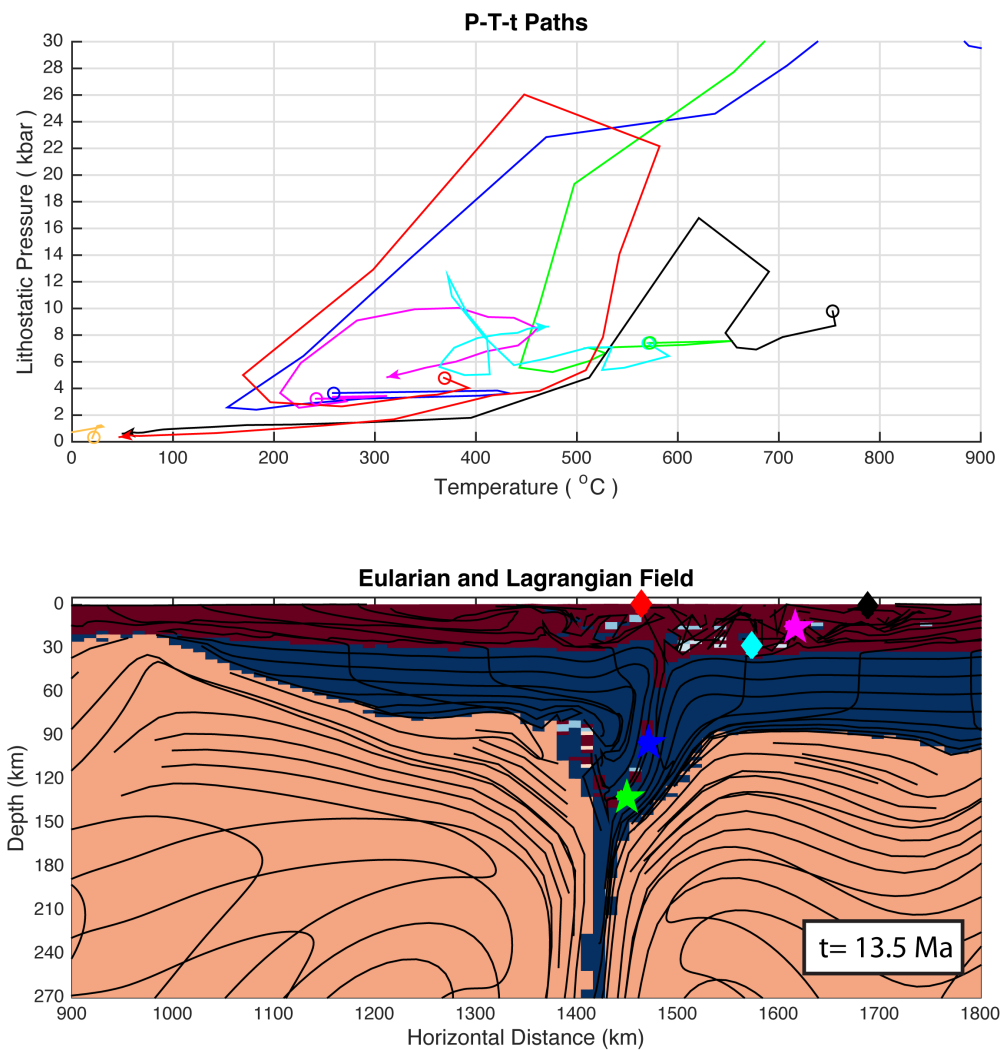


Figure 2.58. Model development and P-T-t paths of tracked particles of experiment C3 with convergence rate of 0 cm/yr after 13.5 Ma. Red: crust, Blue: continental lith. mantle, Yellow: oceanic lith. mantle, Orange: asthenosphere.

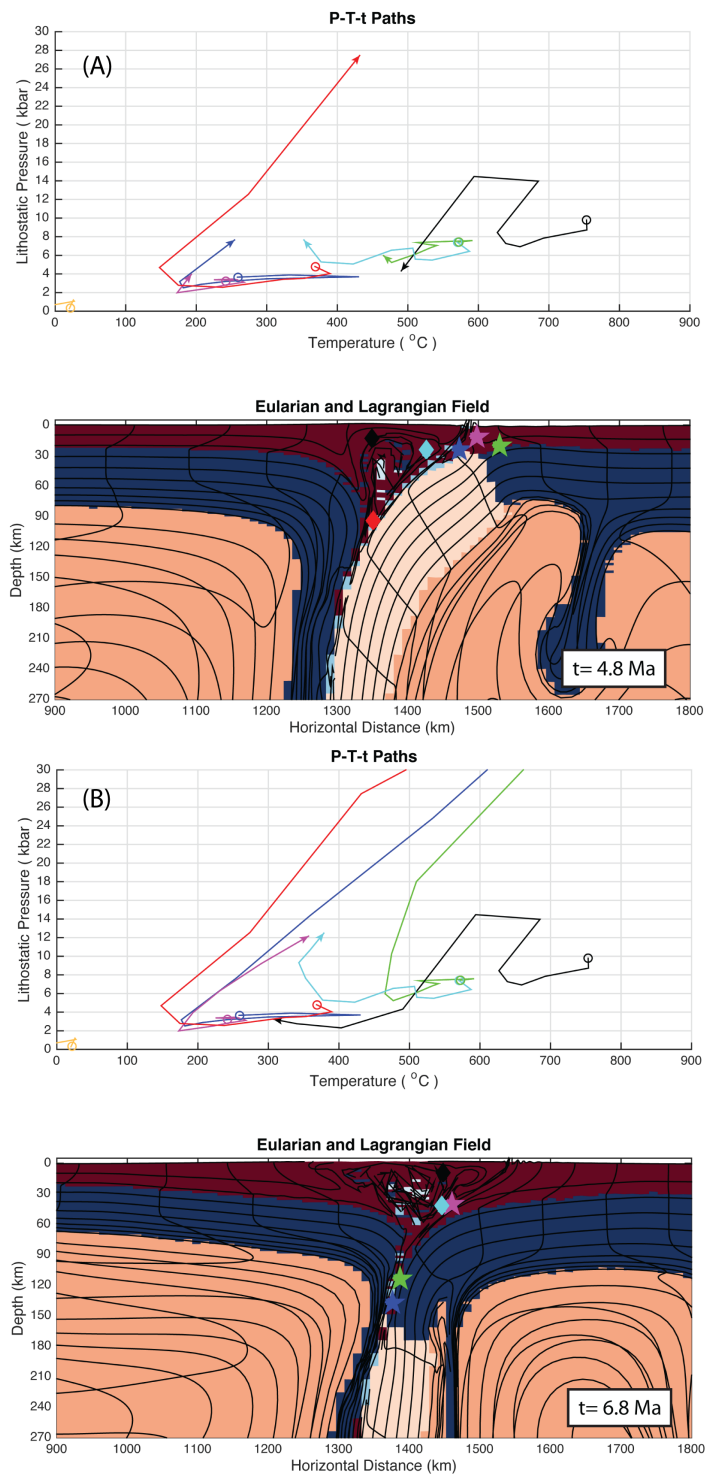


Figure 2.59. Model development and P-T-t paths of tracked particles of experiment C3 with convergence rate of 1 cm/yr (A) after 4.8 Ma, (B) after 6.8 Ma. Red: crust, Blue: continental lith. mantle, Yellow: oceanic lith. mantle, Orange: asthenosphere.

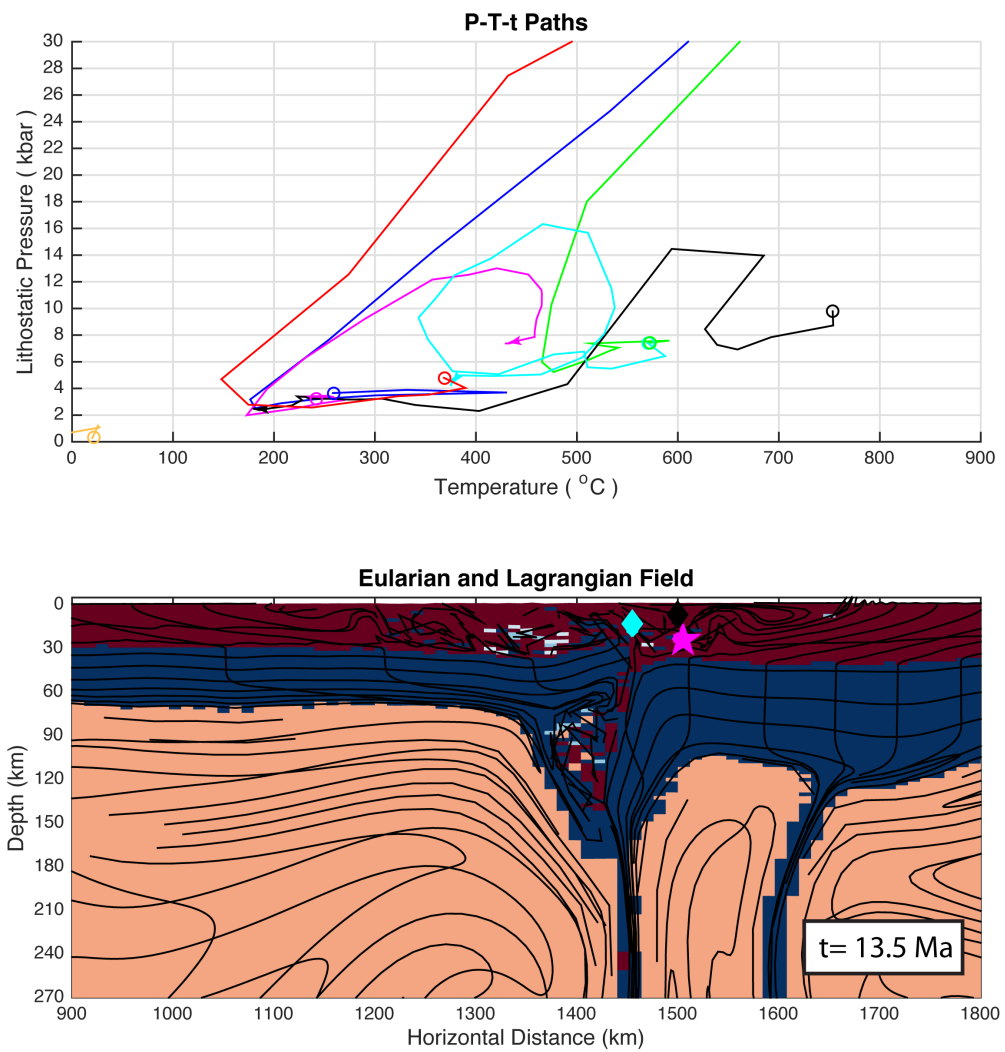


Figure 2.60. Model development and P-T-t paths of tracked particles of experiment C3 with convergence rate of 1 cm/yr after 13.5 Ma. Red: crust, Blue: continental lith. mantle, Yellow: oceanic lith. mantle, Orange: asthenosphere.

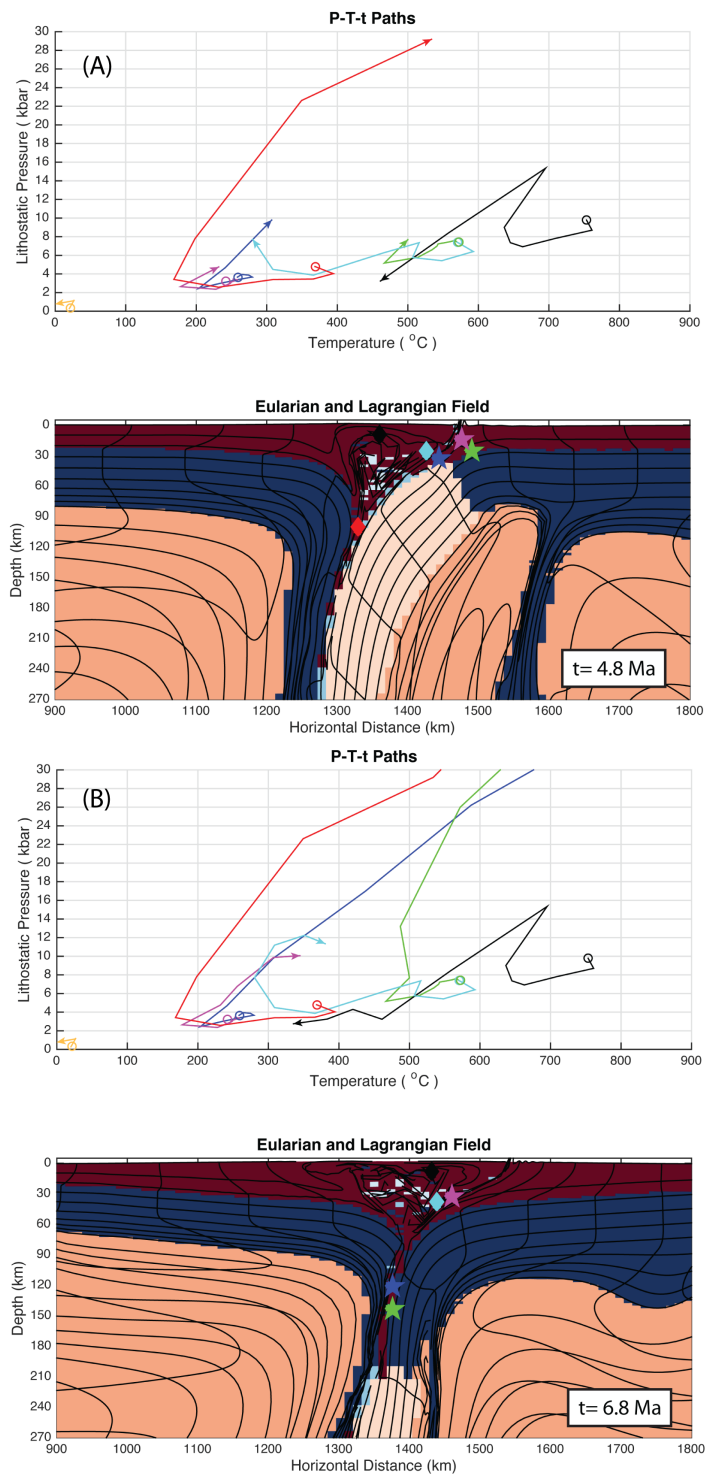


Figure 2.61. Model development and P-T-t paths of tracked particles of experiment C3 with convergence rate of 2 cm/yr (A) after 4.8 Ma, (B) after 6.8 Ma. Red: crust, Blue: continental lith. mantle, Yellow: oceanic lith. mantle, Orange: asthenosphere.

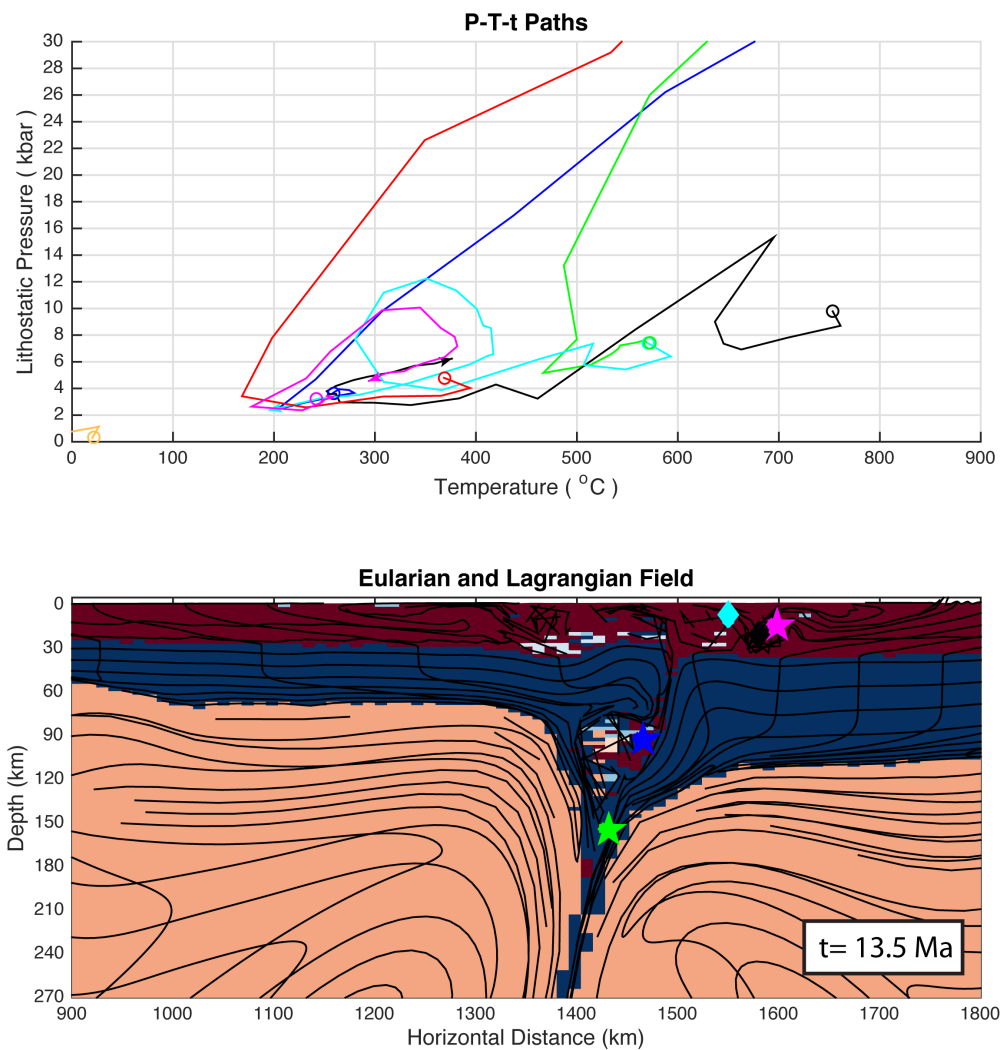


Figure 2.62. Model development and P-T-t paths of tracked particles of experiment C3 with convergence rate of 2 cm/yr after 13.5 Ma. Red: crust, Blue: continental lith. mantle, Yellow: oceanic lith. mantle, Orange: asthenosphere.

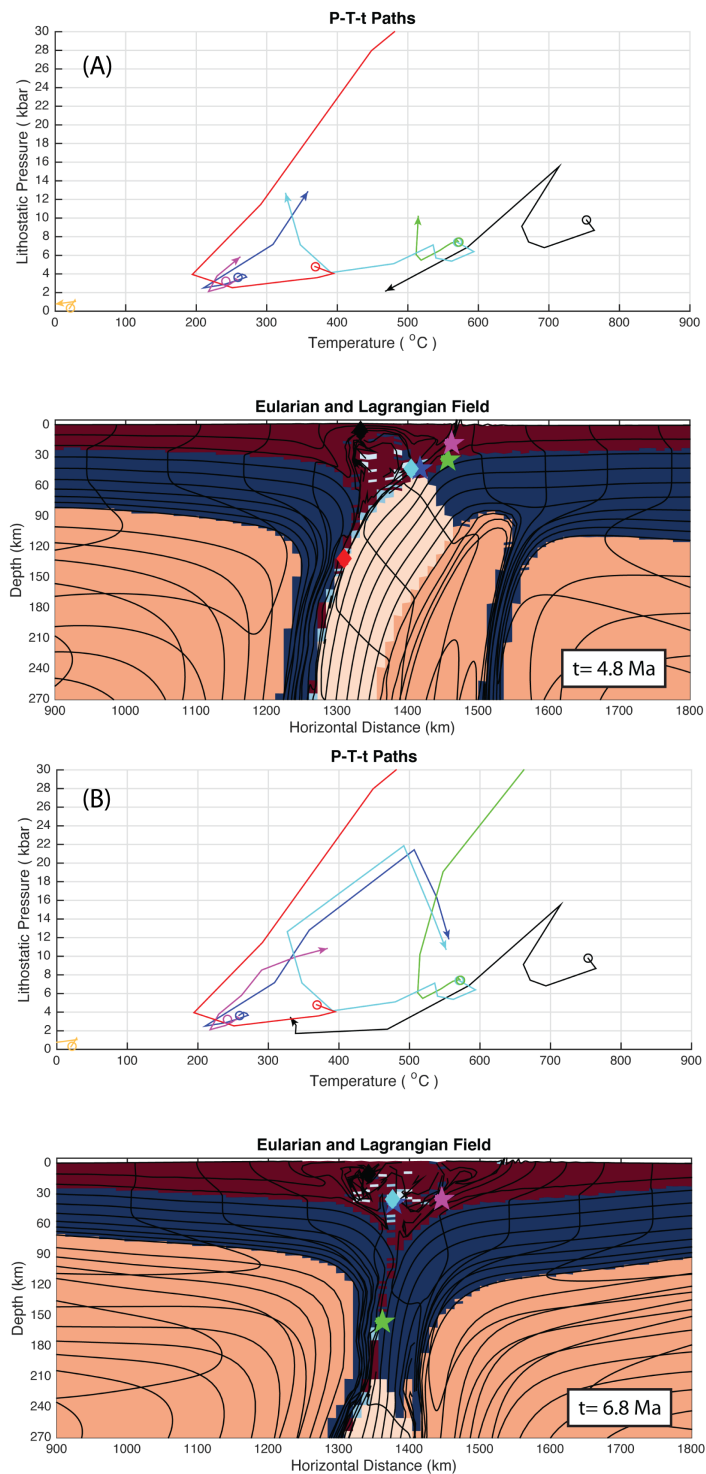


Figure 2.63. Model development and P-T-t paths of tracked particles of experiment C3 with convergence rate of 3 cm/yr (A) after 4.8 Ma, (B) after 6.8 Ma. Red: crust, Blue: continental lith. mantle, Yellow: oceanic lith. mantle, Orange: asthenosphere.

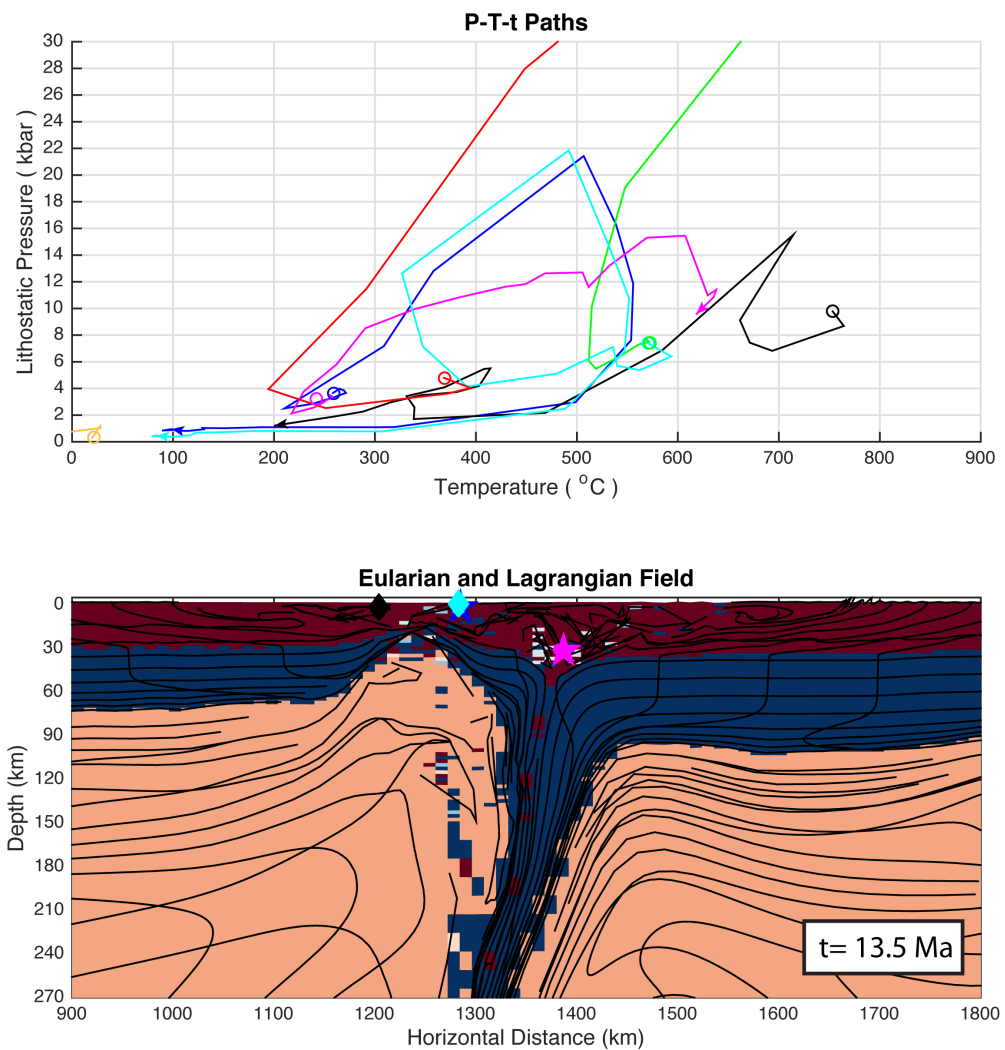


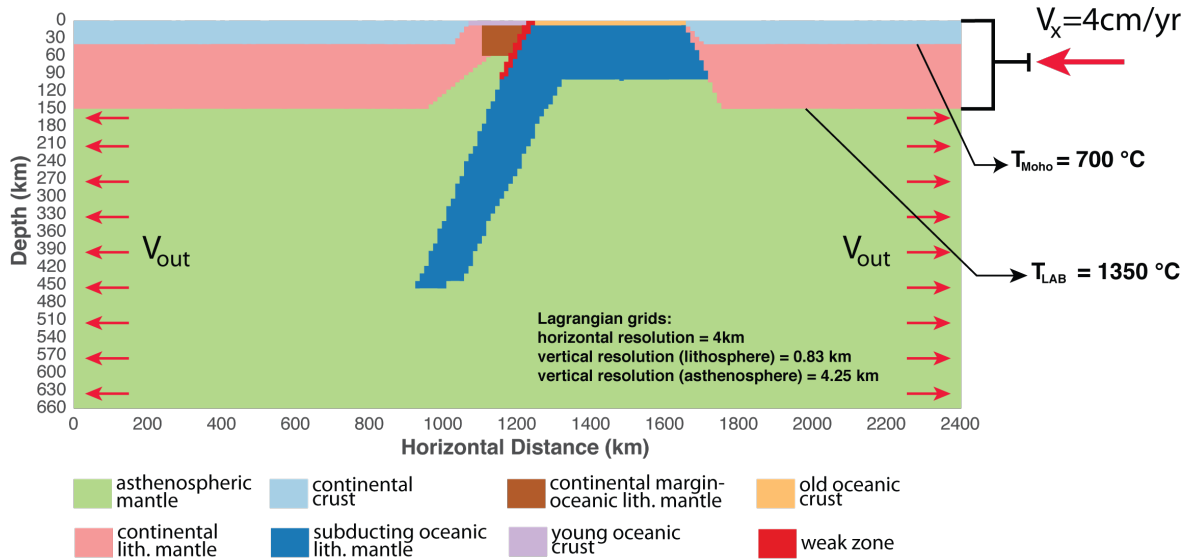
Figure 2.64. Model development and P-T-t paths of tracked particles of experiment C3 with convergence rate of 3 cm/yr after 13.5 Ma. Red: crust, Blue: continental lith. mantle, Yellow: oceanic lith. mantle, Orange: asthenosphere.

2.6. Intra-Oceanic Subduction

2.6.1. Experimental Set D1

In this tectonic configuration, the dynamics of intra-oceanic subduction, and the connection of this tectonic configuration and rheology with burial and exhumation of crustal rocks were studied. It was assumed that the older ocean already subducted under the continental margin which is supposed to be younger. Continental blocks were attached to each layers, and the leftmost side of the model box was pinned. The configuration consisted of 8 different materials that act on each other throughout the model development. To preserve the thermal boundary layer both in the ocean and continent, the temperature at the oceanic part was sharply elevated. The whole continental crust deforms in plastic rheology, but oceanic crust deforms in visco-plastic fashion.

In this experimental set, the impact of deformation type of continental lithospheric mantle to the intra-oceanic subduction dynamics, burial and exhumation of crustal rocks as well. The Moho temperature was kept constant as 700 °C. The convergence rate was set as 4 cm/yr till 12 Ma, then it was decreased to 0 cm/yr.



Region	Plasticity					Viscosity				Density		
	c_0, Pa	ϕ_1	ϕ_2	ϵ_1	ϵ_2	$A, \text{Pa}^{-n} \text{s}^{-1}$	$Q, \text{kJ mol}^{-1}$	n	Ref.	$\rho_0, \text{kg m}^{-3}$	T_0, K	α, K^{-1}
Continental Crust	0	15	2	0.5	1.5	—	—	—	—	2850	500	3.0×10^{-5}
Oceanic Crust (old)	10^7	15	2	0.5	1.5	7.96×10^{-25}	260	3.4	1	2950	750	2.0×10^{-5}
Oceanic Crust (young)	10^7	15	2	0.5	1.5	7.96×10^{-25}	260	3.4	1	2900	750	2.0×10^{-5}
Oceanic Lithospheric Mantle	2×10^7	15	2	0.5	1.5	—	—	—	—	3320	793	2.0×10^{-5}
Sub-lithospheric Mantle	10^7	15	2	0.5	1.5	5.495×10^{-25}	495	4.48	2	3280	793	2.0×10^{-5}

References: 1, Diabase, Gleason and Tullis [1995]; 2, wet Åheim dunite, Chopra and Paterson [1984]. Physical constants in the models are $g = 10.0 \text{ m s}^{-2}$, $c_p = 750 \text{ J kg}^{-1} \text{ K}^{-1}$, $H = 0 \text{ W m}^{-1} \text{ K}^{-1}$, $\kappa = 1.0 \times 10^{-6} \text{ m}^2 \text{ s}^{-2}$, and $R = 8.31 \text{ J mol}^{-1} \text{ K}^{-1}$.

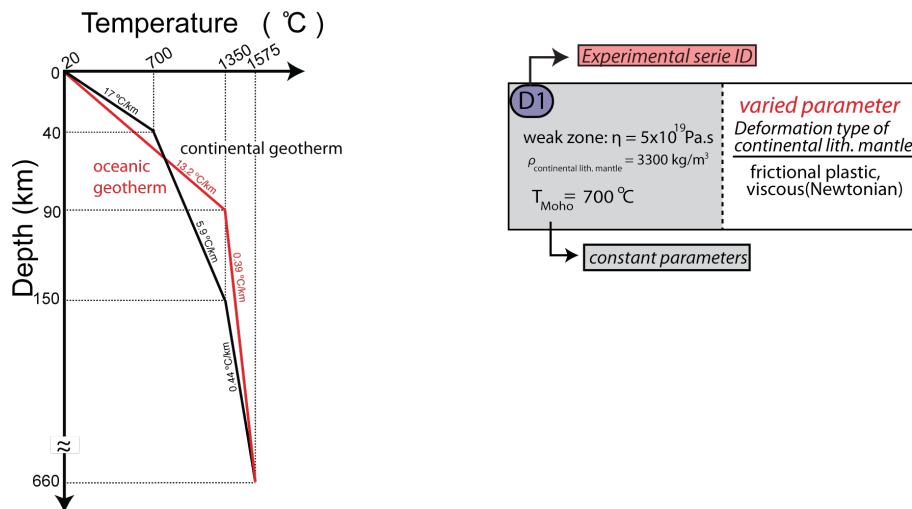


Figure 2.65. Model configuration and flow parameters for the materials of experimental set D1.

2.6.2. Results of D1

When plastic rheology is imposed in the whole lithospheric mantle, after 6 Ma, the ophiolites cool about 300 °C by advection of colder rocks into the subduction channel. The oceanic slab continues to subduct and pull the crust along with continental slab under the ophiolites. The temperature of crustal rocks increase by about 150 - 200 °C. The foreland bulge is seen by focusing on the curvature that initiates right on the margin of subduction ocean-continent transition zone. The pressure of the rock designated by violet circle decreases due to foreland bulge mechanism. Older oceanic crust subducts beneath the ophiolites.

After 12 Ma, the continental rocks are buried down to 80 km at most. The oceanic slab continues to pull the crust beneath the ophiolites. Because of direct contact with asthenospheric flow underneath, by advection, the rocks get heated and their temperatures reach to 640 °C. The temperature of the rock designated by violet circle increase not due to asthenospheric intrusion, but because of increased geotherm that was prescribed for the passive margin.

After 42 Ma, The oceanic slab already detaches from the continent. The asthenospheric flow widens the subduction channel to about 200 km below and narrowing down to 50 km at 30 km beneath the surface. The rock designated by violet circle exhumes back to the surface by buoyancy force without being heated much. The rock designated by blue star can not achieve to decouple from the continental lithospheric mantle and is encapsulated in the mantle. There is some folding on the retro-plate because of shortening mechanism.

When viscous (Newtonian) rheology is imposed only in the continental lithospheric mantle, after 6 Ma, the ophiolites cool about 250 °C by advection of colder rocks into the subduction channel. While the oceanic slab continues to subduct and pull the crust, the continental lithospheric mantle deforms by the the effect of convection in the mantle and convergence between the plates. The temperature of the crustal rocks increase by about 150 - 200 °C. The subduction dynamics of strong oceanic slab

initiates foreland bulge on the retro-plate. This is supported by the decrease of pressure of rock designated by violet circle. A south dipping thrust is well observed in the numerical model.

After 12 Ma, affected by the subduction of oceanic slab, some portion of ophiolite body is detached from its origin and subducted into the asthenospheric mantle. At this stage, the continental rocks are buried into the subduction channel to depths smaller than the case for plastic rheology. The subduction channel is closed by advection of continental lithospheric mantle that is deforming continuously in viscous rheology. The pressure-temperature of rocks at this stage are 16 kbar, 500 °C (blue), and 9 kbar, 350 °C (violet). The ophiolites are cool enough and already obducted to the pro-plate.

The increase in pressure continuous till 16 Ma at time which we already imposed 0 cm/yr convergence before 4 Ma. At 42 Ma, the rocks exhume back to the upper levels provided that their temperature does not show a significant increase throughout the process. It is worth to note that the subduction channel is closed, oceanic slab already detached and metamorphic rocks reside beneath the ophiolitic body. The exhumation of these rocks happen by two distinct major forces which are buoyancy and faulting. The south dipping thrust is translated into a normal fault in the later stages of numerical model.

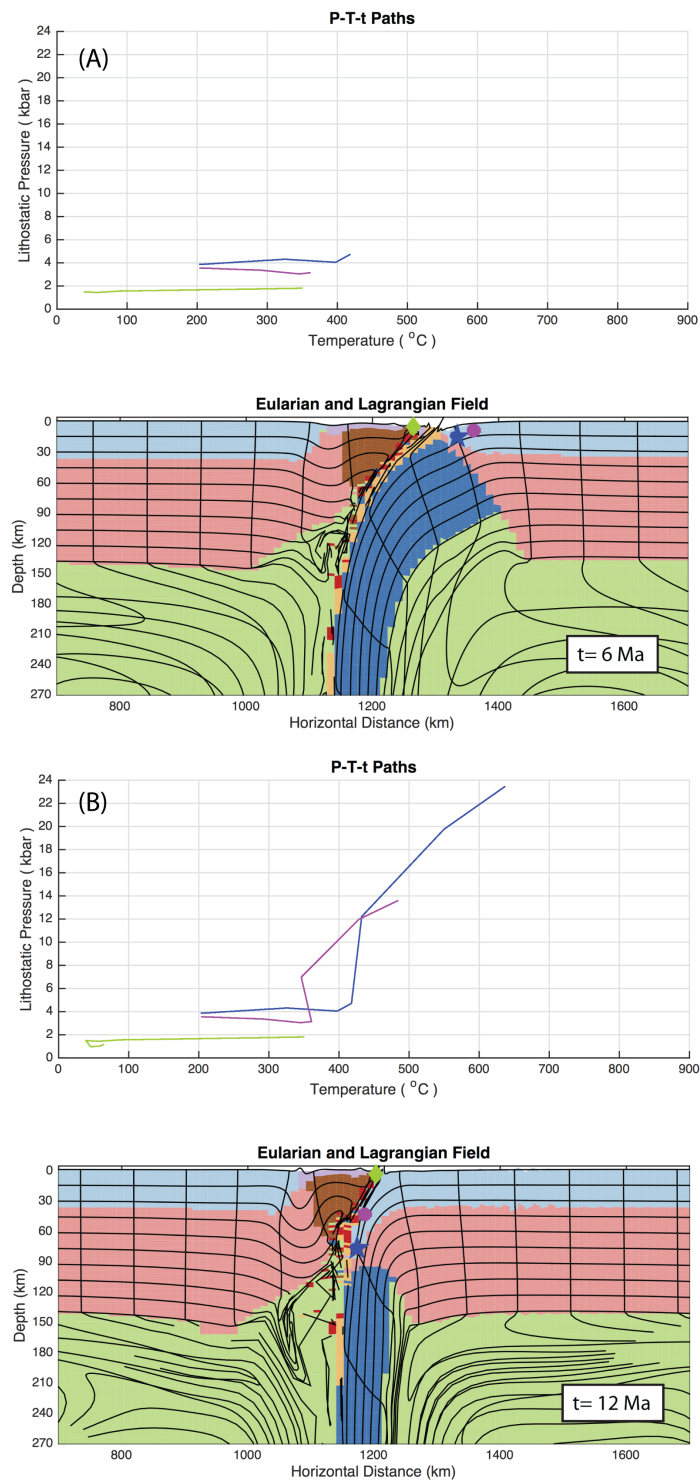


Figure 2.66. Model results and P-T-t paths in exp. D1(plastic lith.) (A)after 6 Ma, (B)after 12 Ma. Blue(light/dark):crust/oceanic slab, Pink:cont. lith. mantle, Green:asth. Brown:cont. margin, Purple/Orange:young/old oceanic crust.

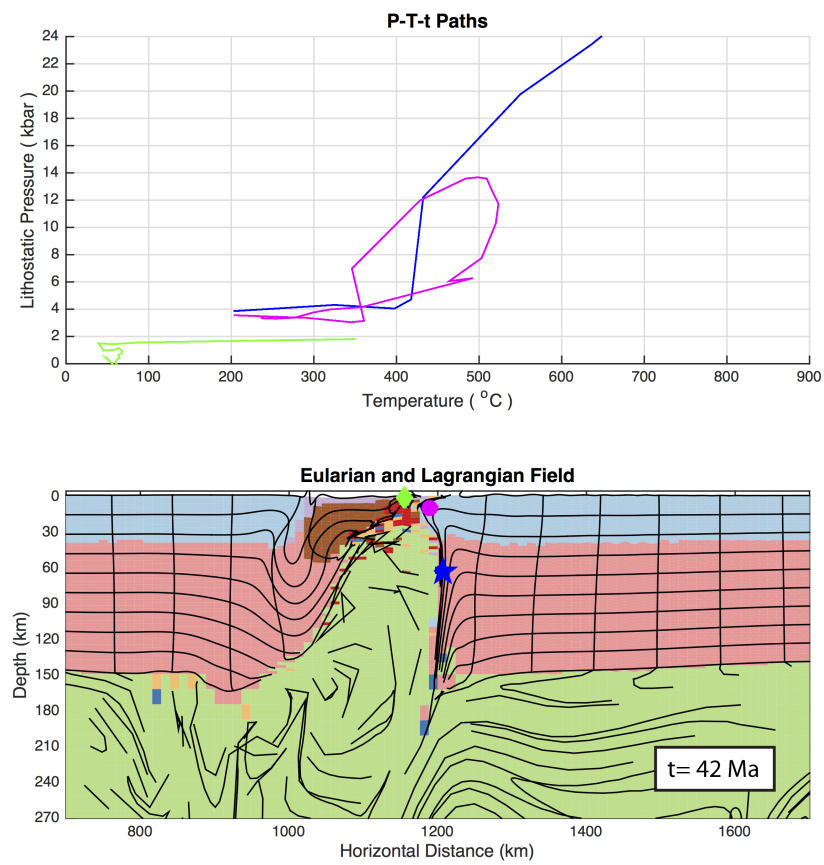


Figure 2.67. Model results and P-T-t paths in exp. D1(plastic lith.) after 42 Ma. Blue(light/dark):crust/oceanic slab, Pink:cont. lith. mantle, Green:asth. Brown:cont. margin, Purple/Orange:young/old oceanic crust.

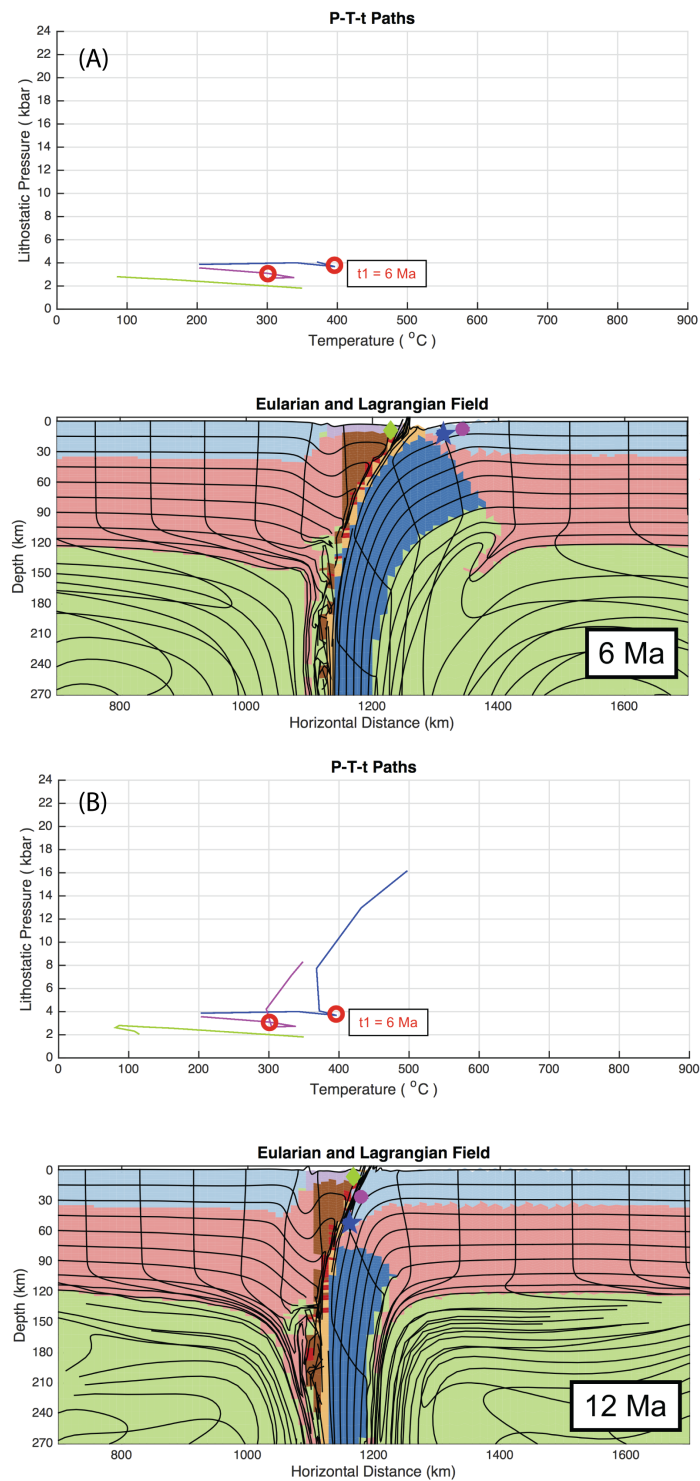


Figure 2.68. Model results and P-T-t paths in exp. D1(viscous lith.) (A)after 6 Ma, (B)after 12 Ma. Blue(light/dark):crust/oceanic slab, Pink:cont. lith. mantle, Green:asth. Brown:cont. margin, Purple/Orange:young/old oceanic crust.

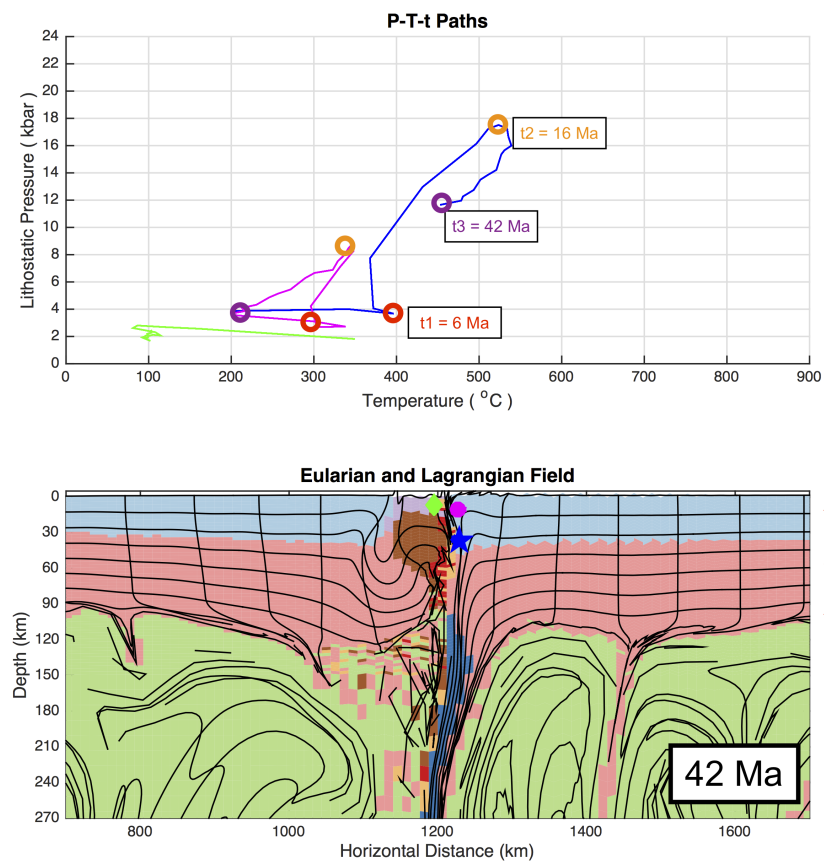
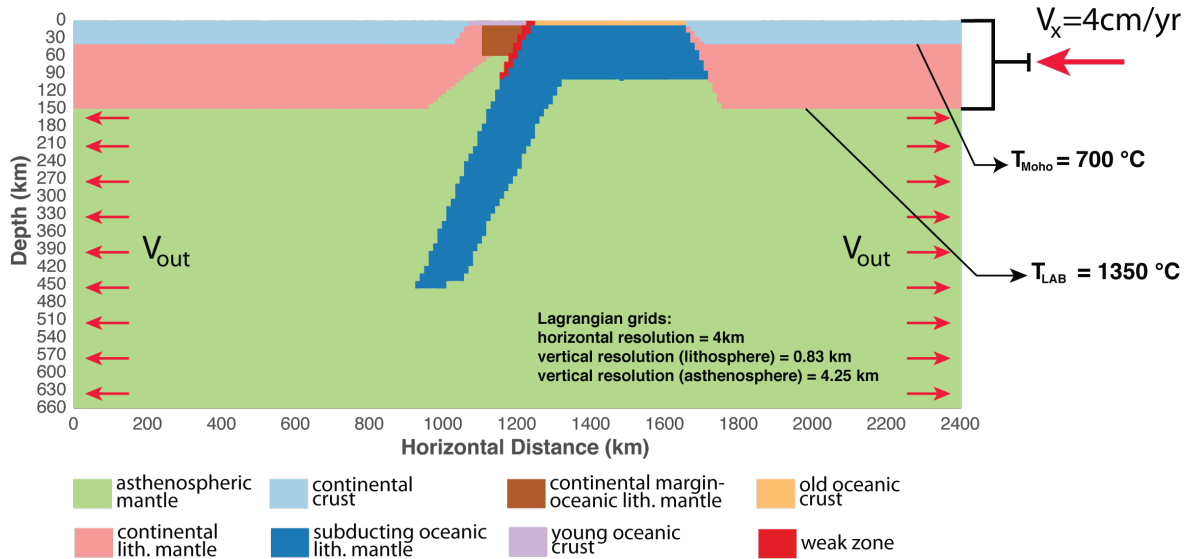


Figure 2.69. Model results and P-T-t paths in exp. D1(viscous lith.) after 42 Ma. Blue(light/dark):crust/oceanic slab, Pink:cont. lith. mantle, Green:asth. Brown:cont. margin, Purple/Orange:young/old oceanic crust.

2.6.3. Experimental Set D2

In this experimental set, the configuration was kept the same with the experimental set D1. The effect of crustal rheology on intra-oceanic subduction dynamics as well as burial and exhumation of crustal rocks was investigated. The model result only for the case of visco-plastic rheology in the continental crust is shown. The corresponding model which has the crust deforming in plastic rheology is already presented in the presented in the previous case. The continental lithospheric mantle deforms in viscous (Newtonian) rheology. The Moho temperature was kept at 700 °C. In order to preserve the thermal boundary layer both in the ocean and continent, the temperature at the oceanic part was sharply elevated.



Region	Plasticity					Viscosity				Density		
	c_0, Pa	ϕ_1	ϕ_2	ϵ_1	ϵ_2	$A, \text{Pa}^{-n} \text{s}^{-1}$	$Q, \text{kJ mol}^{-1}$	n	Ref.	$\rho_0, \text{kg m}^{-3}$	T_0, K	α, K^{-1}
Oceanic Crust (old)	10^7	15	2	0.5	1.5	7.96×10^{-25}	260	3.4	1	2950	750	2.0×10^{-5}
Oceanic Crust (young)	10^7	15	2	0.5	1.5	7.96×10^{-25}	260	3.4	1	2900	750	2.0×10^{-5}
Oceanic Lithospheric Mantle	2×10^7	15	2	0.5	1.5	—	—	—	—	3320	793	2.0×10^{-5}
Continental Lithospheric Mantle	—	—	—	—	—	4.16×10^{-4}	495	1	2	3300	793	2.0×10^{-5}
Sub-lithospheric Mantle	10^7	15	2	0.5	1.5	5.495×10^{-25}	495	4.48	2	3280	793	2.0×10^{-5}

References: 1, Diabase, Gleason and Tullis [1995]; 2, wet Åheim dunitite, Chopra and Paterson [1984]. Physical constants in the models are $g = 10.0 \text{ m s}^{-2}$, $c_p = 750 \text{ J kg}^{-1} \text{ K}^{-1}$, $H = 0 \text{ W m}^{-1} \text{ K}^{-1}$, $\kappa = 1.0 \times 10^{-6} \text{ m}^2 \text{ s}^{-2}$, and $R = 8.31 \text{ J mol}^{-1} \text{ K}^{-1}$.

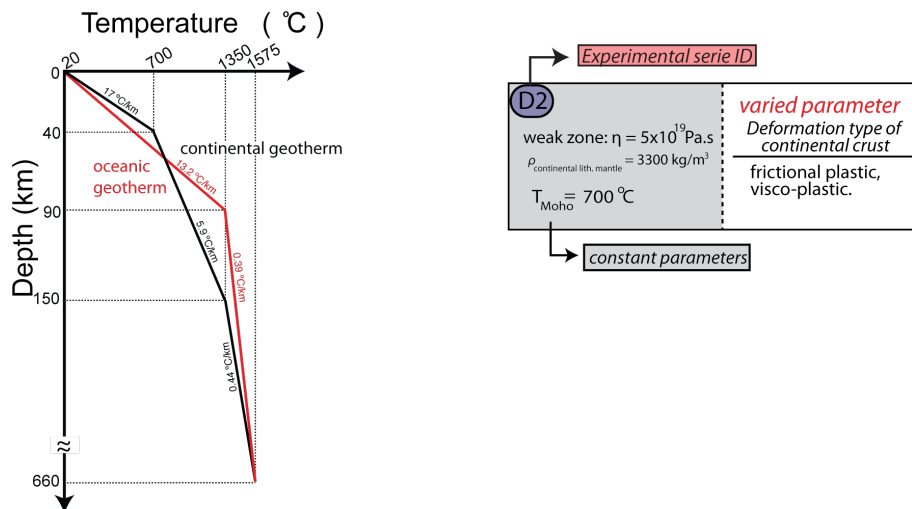


Figure 2.70. Model configuration and flow parameters for the materials of experimental set D2.

2.6.4. Results of D2

When the crustal rocks deform in visco-plastic fashion, it is expected that they will deform highly enough and detach from the lithospheric mantle beneath. After 4 Ma, the oceanic slab continues to subduct under the continental block. The foreland bulge is clearly seen from the model output and pressure decrease of crustal rocks in the P-T-t graph in Figure 2.76. It is worth to note that the foreland bulge is more effective than the previous case. This is so because the crust deforms in higher strain rates and lower viscosities, hence it deforms high enough that can be affected by any tectonic forces during the subduction process. The temperature of rocks in the continent get heated by about 100 - 150 °C, whereas the ophiolites cool by about 180 °C.

After 8 Ma, the continental rocks in the lower crust are subduction into the subduction channel, but the rocks on the upper levels are thrust to the retro-plate. The subduction channel is closed by the advection of continental lithospheric mantle. The ophiolitic body is subsided below the thrust continental rocks. The pressure-temperature values of rocks at that stage are 14 kbar, 430 °C (blue), 5 kbar, 250 °C (violet) and 4 kbar, 150 °C (green).

After 28 Ma, the continental rocks already exhume to the upper levels. The deformation of the lagrangian mesh suggests significant deformation in the continental crust. The ophiolitic body is wholly subsided below the continental rocks and metamorphics. The subduction channel is closed by advection of continental lithospheric mantle and this provided cooler temperatures for the rocks.

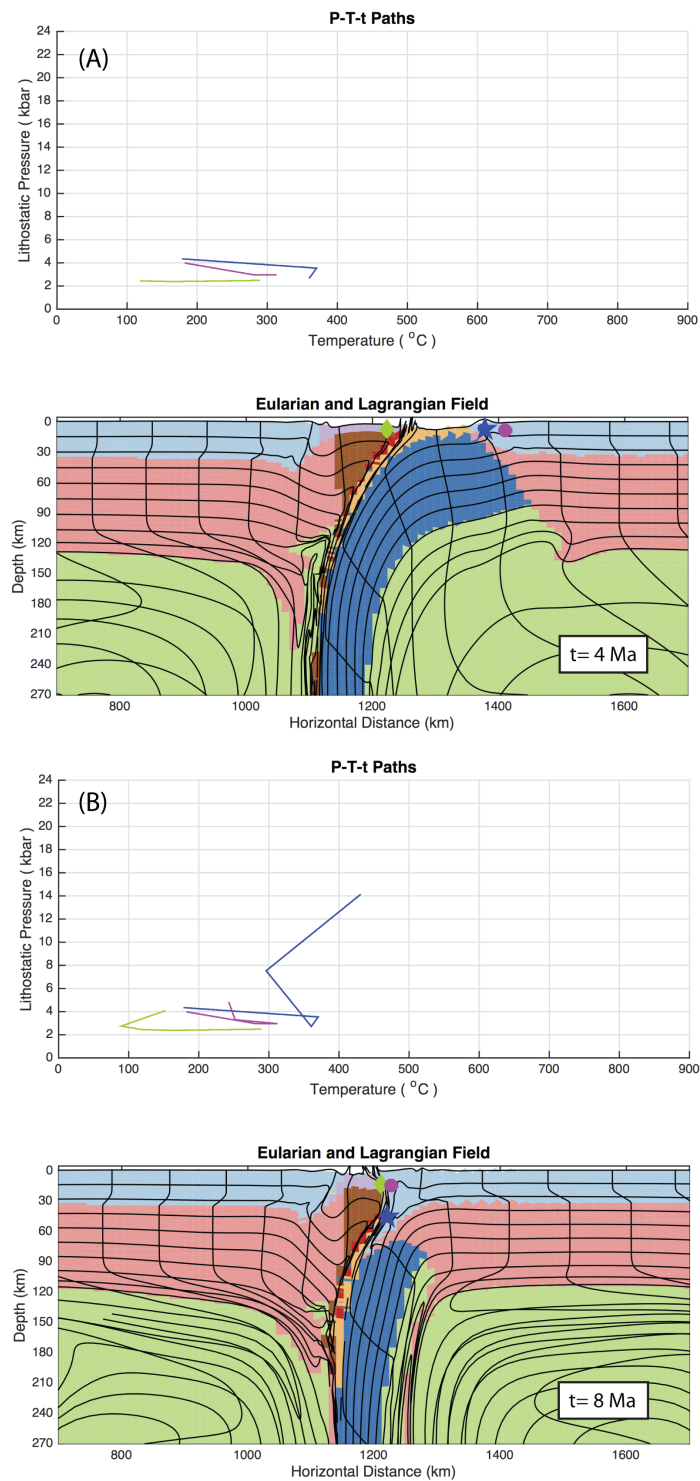


Figure 2.71. Model results and P-T-t paths in exp. D2(viscoplastic crust.) (A) after 4 Ma, (B) after 8 Ma. Blue(light/dark):crust/oceanic slab, Pink:cont. lith. mantle, Green:asth. Brown:cont. margin, Purple/Orange:young/old oceanic crust.

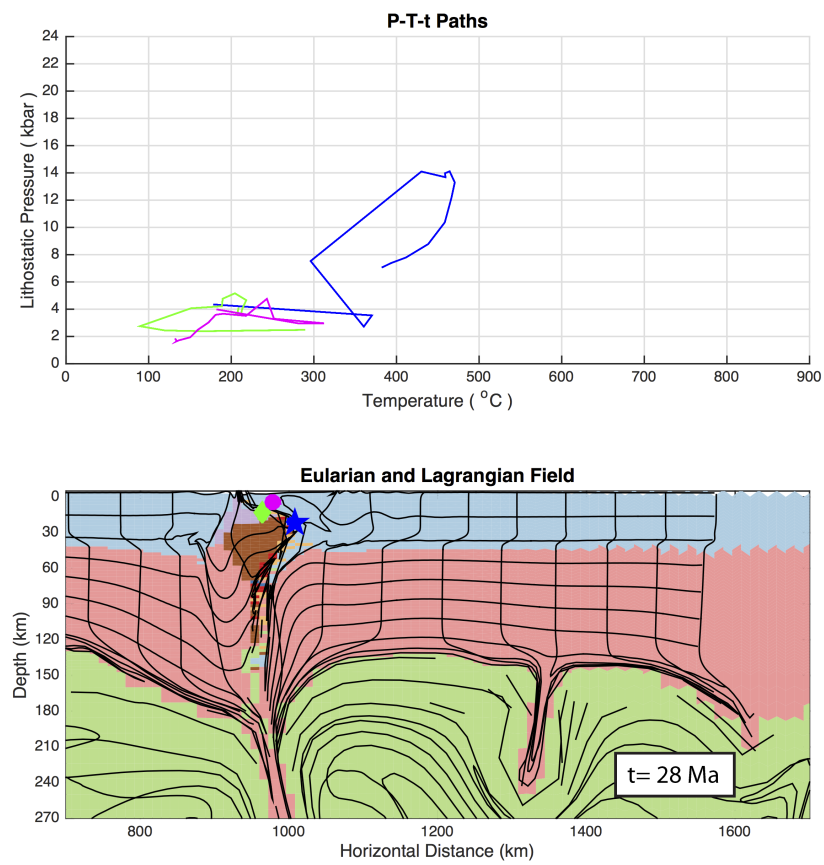


Figure 2.72. Model results and P-T-t paths in exp. D2(viscoplastic crust.) after 28 Ma. Blue(light/dark):crust/oceanic slab, Pink:cont. lith. mantle, Green:asth. Brown:cont. margin, Purple/Orange:young/old oceanic crust.

3. DISCUSSION AND CONCLUSION

The mechanism of burial and exhumation was investigated in various tectonic configurations such as oceanic plate subduction under continent, intra-oceanic subduction and post-collision. The first and second set of experiments were performed to understand the post-collisional dynamics. The main focus was to give some rheological constraints to the burial and exhumation of crustal rocks. This was primarily done to simulate the later stages of Tethyan evolution of Western Anatolia. It was assumed that after the consumption of the Tethyan ocean, continental collision was the active mechanism that might have been the key actor for the burial and exhumation of continental rocks.

The numerical experiments in the post-collision configuration show that it is possible to observe exhumation of lower crust in continental collision or intra-plate regions if the Moho temperature is high enough (900°C) to effect the crustal depths during the time at which continental lithosphere drips down into the asthenosphere; and the upper/middle crust is weak enough ($Q = 43 \text{ kJ/mol}$) not to overcome the stress applied onto it by the accumulated lower crust during Rayleigh-Taylor instability. Though these constraints provide exhumation of lower crust in this tectonic configuration, the maximum pressure-temperature values of the rocks are mostly in high pressure / high temperature (HP/HT) region, therefore these values are not in good agreement with natural data for Tavsanli and Afyon Zone.

Modeling results for the oceanic plate subduction under continent show that when continental lithospheric mantle deforms in plastic rheology, the continental rocks are buried to 50 km depth at 3 cm/yr, but at higher velocities, the rocks are buried down to 94 km (for convergence rate of 4 cm/yr) and 112 km depth (for convergence rate of 5 cm/yr). It is clear that increasing the convergence rate enhances the burial depth of crustal rocks in plastic rheology. This is possible because of coupling between the crust and the lithospheric mantle at higher speeds. The continental lithospheric mantle deforms as a coherent massive block, and rocks are buried along the subduction channel

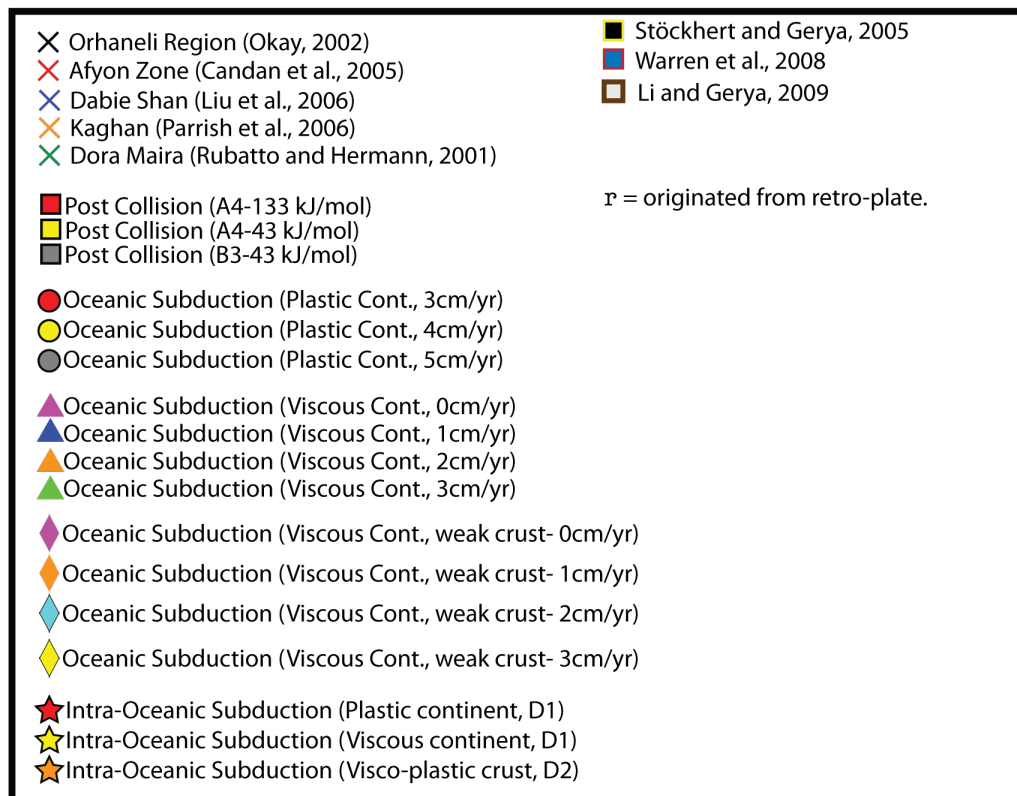
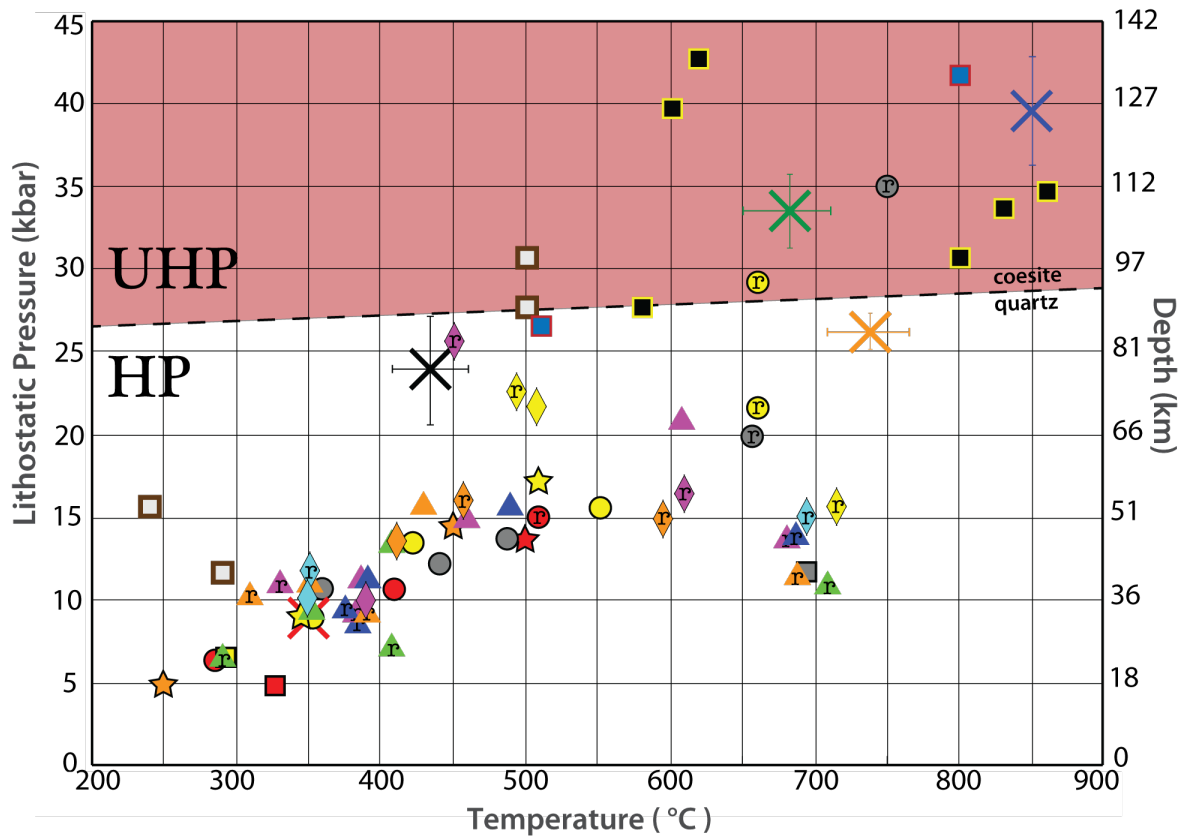


Figure 3.1. Maximum pressure-temperature values for the whole set of experiments.

The results are compared with other works and natural data in the literature.

by slab traction. For convergence rates equal or greater than 3cm/yr the opening in the subduction channel and asthenospheric intrusion has two major effects on the buried rocks. The first effect is the buoyancy force. The second effect is the increase in temperature by advection, and then conduction in time. It is important to note that the exhumation rate of these rocks are high enough not to get heated in the first place by the hot rising asthenosphere into the subduction channel. The pressure - temperature conditions for higher convergence rates are in good agreement with natural data of metamorphic rocks in Dabie Shan (> 30 kbar, $600 - 750$ °C) [2,44].

High pressure / low temperature (HP/LT) exhumation is possible if the continental lithospheric mantle deforms in viscous (Newtonian) rheology. This is possible, because the viscous rheology is the key factor for the closure of the subduction channel. If the subduction channel is closed by continental lithospheric mantle, then it is possible to get lower geotherm, hence lower temperatures for the buried continental rocks as well. The asthenospheric intrusion is not observed in this configuration, which means that there is no notable melting close to the suture zone, which is very consistent with Tavsanlı and Afyon Zones. The numerical models for this tectonic setting indicate that rocks are buried to 72 km depths at most when there is no convergence rate. Increasing the convergence rate reduces the burial depth. This shows that vertical tectonics drive the burial and exhumation in viscous rheology. Horizontal forces diminish the effect of vertical forces. The problem is that some of the rocks from the retro-plate come into the subduction channel, circulate like a washing machine, and then exhume back to the pro- or retro-plate. This is not the case for the Tavsanlı and Afyon Zones where all of the metamorphic rocks for both continental units are interpreted to be originated from Anatolides block [5, 58, 66] which is the pro-plate (lower plate) attached to the older oceanic slab.

If the crust is weak enough, then it is possible to bury the continental rocks down to 85 km depth and keep their temperature below 460 °C, then exhume them back to the surface by subduction channel-flow process. The numerical modelling results for viscous continental plate subduction with weaker crust suggest that Tavsanlı Zone might have been formed with a weaker crustal rheology. Combining this suggestion

with the Afyon Zone gives a very interesting result: there might have been some heterogeneity within the continental crust of Anatolides block and this might have played a key factor on the significant difference in their burial depths and can provide explanation for the preservation of their heat. Again, the major contrasting point might be the fact that both Tavsanlı and Afyon Zone metamorphic rocks must originated from the pro-plate, but numerical modelling results do give some rocks that come from the pro-plate as well.

Modifying the configuration to represent intra-oceanic subduction (in plastic rheology) gives very similar results in the sense that the metamorphic rocks are buried beneath the ophiolite body and exhume back to the upper levels. This is in good agreement with the Tavsanlı Zone and Afyon Zone, because the ophiolites are mostly obducted onto the metamorphic rocks in these regions [29]. When the deformation of continental lithospheric mantle is plastic, the subduction channel widens about 100 km at the later stages of subduction and collision, hence it is of high probability to observe notable melting in the pro-plate which is not observed in Tavsanlı and Afyon Zone. It is worth to note that there is some small amount of granodiorite intrusion to the metamorphics, but this intrusion was aged to Eocene epoch.

If the continental lithospheric mantle deforms in viscous (Newtonian) rheology, then the idea of closure of subduction channel proves to be a strong and major mechanism in intra-oceanic subduction system as well. The viscously deforming lithospheric mantle is the main component that can shield the buried rocks from asthenospheric intrusion. The crustal rocks are buried beneath the ophiolite body and their temperatures are kept reasonably lower than the previous case. The pressure-temperature conditions of rocks originated from pro-plate fits well to the Afyon Zone metamorphic rocks, and close enough to the Tavsanlı metamorphics. The obduction of ophiolites onto the pro-plate and above the metamorphic rocks is the significant result of this tectonic configuration. It is also worth to note that, all of the metamorphic rocks originate from the pro-plate, and there is no space for the retro-plate crustal rocks to be buried into channel. This is in good agreement with Tavsanlı and Afyon Zones as well.

REFERENCES

1. Liou, J. G., T. Tsujimori, R. Y. Zhang, I. Katayama, and S. Maruyama, “Global UHP Metamorphism and Continental Subduction/Collision: The Himalayan Model”, *International Geology Review*, Vol. 46, No. 1, pp. 1–27, 2004.
2. Liu, D., P. Jian, A. Kröner, and S. Xu, “Dating of prograde metamorphic events deciphered from episodic zircon growth in rocks of the Dabie-Sulu UHP complex, China”, *Earth Planet. Sci. Lett.*, Vol. 250, No. 3-4, pp. 650–666, 2006.
3. Mposkos, E. D. and D. K. Kostopoulos, “Diamond, former coesite and supersilicic garnet in metasedimentary rocks from the Greek Rhodope: A new ultrahigh-pressure metamorphic province established”, *Earth Planet. Sci. Lett.*, Vol. 192, No. 4, pp. 497–506, 2001.
4. Okay, A. I., “Jadeite chloritoid glaucophane lawsonite blueschists in north-west Turkey : unusually high P / T ratios in continental crust”, *J. Metamorph. Geol.*, Vol. 20, pp. 757–768, 2002.
5. Candan, O., M. Çetinkaplan, R. Oberhänsli, G. Rimmelé, and C. Akal, “Alpine high-P/low-T metamorphism of the Afyon Zone and implications for the metamorphic evolution of Western Anatolia, Turkey”, *Lithos*, Vol. 84, No. 1-2, pp. 102–124, 2005.
6. Parrish, R. R., S. J. Gough, M. P. Searle, and D. J. Waters, “Plate velocity exhumation of ultrahigh-pressure eclogites in the Pakistan Himalaya”, *Geology*, Vol. 34, No. 11, pp. 989–992, 2006.
7. Kylander-Clark, A. R. C., B. R. Hacker, and C. G. Mattinson, “Size and exhumation rate of ultrahigh-pressure terranes linked to orogenic stage”, *Earth Planet. Sci. Lett.*, Vol. 321-322, pp. 115–120, 2012.

8. Gilotti, J. A. and E. J. K. Ravna, “First evidence for ultrahigh-pressure metamorphism in the North-East Greenland Caledonides”, *Geology*, Vol. 30, No. 6, pp. 551–554, 2002.
9. Ghent, E. D., M. Z. Stout, and P. Erdmer, “Pressure-temperature evolution of lawsonite-bearing eclogites, Pinchi Lake, British Columbia”, *J. Metamorph. Geol.*, Vol. 11, No. 2, pp. 279–290, 1993.
10. Danis, C. R., N. R. Daczko, M. A. Lackie, and S. J. Craven, “Retrograde metamorphism of the Wongwibinda Complex, New England Fold Belt and the implications of 2.5D subsurface geophysical structure for the metamorphic history”, *Aust. J. Earth Sci.*, Vol. 57, No. 3, pp. 357–375, 2010.
11. Tagiri, M., T. Yano, A. Bakirov, T. Nakajima, and S. Uchiumi, “Mineral parageneses and metamorphic PT paths of ultrahigh-pressure eclogites from Kyrghyzstan TienShan”, *Isl. Arc*, Vol. 4, No. 4, pp. 280–292, 1995.
12. Liou, J. G., W. G. Ernst, R. Y. Zhang, T. Tsujimori, and B. M. Jahn, “Ultrahigh-pressure minerals and metamorphic terranes - The view from China”, *J. Asian Earth Sci.*, Vol. 35, No. 3-4, pp. 199–231, 2009.
13. Warren, C. J., “Exhumation of (ultra-)high-pressure terranes: concepts and mechanisms”, *Solid Earth*, Vol. 4, No. 1, pp. 75–92, 2013.
14. Hacker, B. R. and T. V. Gerya, “Paradigms, new and old, for ultrahigh-pressure tectonism”, *Tectonophysics*, Vol. 603, pp. 79–88, 2013.
15. Okay, A. I. and O. Tuysuz, “Tethyan sutures of northern Turkey”, *Geol. Soc. London, Spec. Publ.*, Vol. 156, No. 1, pp. 475–515, 1999.
16. Pourteau, A., O. Candan, and R. Oberhänsli, “High-pressure metasediments in central Turkey: Constraints on the Neotethyan closure history”, *Tectonics*, Vol. 29, No. 5, p. TC5004, 2010.

17. Burov, E. and A. Watts, "The long-term strength of continental lithosphere: "jelly sandwich" or "crème brûlée?"", *GSA Today*, Vol. 16, No. 1, pp. 4–11, 2006.
18. Bucher, K. and M. Frey, *Petrogenesis of Metamorphic Rocks*, Springer-Verlag, 6 edition, 1994.
19. Ranalli, G., "Rheology of the lithosphere in space and time", *Geol. Soc. London, Spec. Publ.*, Vol. 121, No. 1, pp. 19–37, 1997.
20. Gleason, G. C. and J. Tullis, "A flow law for dislocation creep of quartz aggregates determined with the molten salt cell", *Tectonophysics*, Vol. 247, No. 1-4, pp. 1–23, 1995.
21. Chopra, P. and M. Paterson, "The role of water in the deformation of dunite", *Journal of Geophysical Research*, Vol. 89, No. B9, pp. 7861–7876, 1984.
22. Marshak, S., *Earth Portrait of a Planet*, W.W. Norton & Company, 1955.
23. Wilson, M., *Igneous Petrogenesis: A Global Tectonic Approach*, London: Chapman & Hall, 1997.
24. Rohlf, J., *Modern Physics from α to Z0*, John Wiley Sons Inc., 1994.
25. Griffiths, D. J., *Introduction to Quantum Mechanics*, Vol. 1, Pearson Education Limited, 2005.
26. Serway, R. a. and L. D. Kirkpatrick, *Physics for Scientists and Engineers with Modern Physics*, Vol. 26, Thomson-Brooks/Cole, 1988.
27. Kittel, C., *Introduction to Solid State Physics*, John Wiley Sons Inc., 2005.
28. Turcotte, D. L., S. Gerald, and D. Lawson, *Geodynamics*, Cambridge University Press, 2002.

29. Okay, A. I., N. B. Harris, and S. P. Kelley, “Exhumation of blueschists along a Tethyan suture in northwest Turkey”, *Tectonophysics*, Vol. 285, No. 3-4, pp. 275–299, 1998.
30. Okay, A. I., “Paragonite Eclogites from Dabie-Shan, China - Re-Equilibration during Exhumation”, *J. Metamorph. Geol.*, Vol. 13, No. 4, pp. 449–460, 1995.
31. Reuber, G., B. J. Kaus, S. M. Schmalholz, and R. W. White, “Nonlithostatic pressure during subduction and collision and the formation of (ultra)high-pressure rocks”, *Geology*, Vol. 44, No. 5, p. G37595.1, 2016.
32. England, P. and P. Molnar, “Surface uplift, uplift of rocks, and exhumation of rocks”, *Geology*, Vol. 18, pp. 1173–1177, 1990.
33. Boutelier, D., A. Chemenda, and C. Jorand, “Continental subduction and exhumation of high-pressure rocks: insights from thermo-mechanical laboratory modelling”, *Earth Planet. Sci. Lett.*, Vol. 222, No. 1, pp. 209–216, 2004.
34. Warren, C. J., C. Beaumont, and R. A. Jamieson, “Formation and exhumation of ultra-high-pressure rocks during continental collision: Role of detachment in the subduction channel”, *Geochemistry, Geophys. Geosystems*, Vol. 9, No. 4, pp. n/a–n/a, apr 2008.
35. Warren, C., C. Beaumont, and R. Jamieson, “Modelling tectonic styles and ultra-high pressure (UHP) rock exhumation during the transition from oceanic subduction to continental collision”, *Earth Planet. Sci. Lett.*, Vol. 267, No. 1-2, pp. 129–145, 2008.
36. Brun, J. P. and C. Faccenna, “Exhumation of high-pressure rocks driven by slab rollback”, *Earth Planet. Sci. Lett.*, Vol. 272, No. 1-2, pp. 1–7, 2008.
37. Chemenda, A. I., M. Mattauer, J. Malavieille, and A. N. Bokun, “normal faulting : Results from physical modelling”, *Earth Planet. Sci. Lett.*, Vol. 132, No. 1-4, pp.

- 225–232, 1995.
38. Duretz, T. and T. V. Gerya, “Slab detachment during continental collision: Influence of crustal rheology and interaction with lithospheric delamination”, *Tectonophysics*, Vol. 602, pp. 124–140, 2013.
 39. Gerya, T. and B. Stöckhert, “Two-dimensional numerical modeling of tectonic and metamorphic histories at active continental margins”, *Int. J. Earth Sci.*, Vol. 95, No. 2, pp. 250–274, 2006.
 40. Li, Z. and T. V. Gerya, “Polyphase formation and exhumation of high- to ultrahigh-pressure rocks in continental subduction zone: Numerical modeling and application to the Sulu ultrahigh-pressure terrane in eastern China”, *J. Geophys. Res.*, Vol. 114, No. B9, p. B09406, 2009.
 41. Li, Z. H., Z. Q. Xu, and T. V. Gerya, “Flat versus steep subduction : Contrasting modes for the formation and exhumation of high- to ultrahigh-pressure rocks in continental collision zones”, Vol. 301, pp. 65–77, 2011.
 42. Sizova, E., T. Gerya, and M. Brown, “Exhumation mechanisms of melt-bearing ultrahigh pressure crustal rocks during collision of spontaneously moving plates”, *J. Metamorph. Geol.*, Vol. 30, No. 9, pp. 927–955, 2012.
 43. Beaumont, C., R. Jamieson, J. Butler, and C. Warren, “Crustal structure: A key constraint on the mechanism of ultra-high-pressure rock exhumation”, *Earth Planet. Sci. Lett.*, Vol. 287, No. 1-2, pp. 116–129, 2009.
 44. Okay, A. and A. M. C. Şengör, “Evidence for intracontinental thrust-related exhumation of the ultra-high-pressure rocks in China Evidence for intracontinental thrust-related exhumation of the ultra-high-pressure rocks in China”, *Geology*, pp. 411–414, 1992.
 45. Andersen, T. B., B. Jamtveit, J. F. Dewey, and E. Swensson, “Subduction and

- duction of continental crust: major mechanisms during continent-continent collision and orogenic extensional collapse, a model based on the south Norwegian Caledonides”, *Terra Nova*, Vol. 3, pp. 303–310, 1991.
46. Şengör, A. M. C., M. Satır, and R. Akkök, “Timing of Tectonic Events in the Menderes Massif, Western Turkey: Implications for Tectonic Evolution and Evidence for Pan-African Basement in Turkey”, *Tectonics*, Vol. 3, No. 7, pp. 693–707, 1984.
 47. Jolivet, L. and J.-P. Brun, “Cenozoic geodynamic evolution of the Aegean”, *International Journal of Earth Sciences*, Vol. 99, No. 1, pp. 109–138, 2008.
 48. Gessner, K., L. A. Gallardo, V. Markwitz, U. Ring, and S. N. Thomson, “What caused the denudation of the Menderes Massif: Review of crustal evolution, lithosphere structure, and dynamic topography in southwest Turkey”, *Gondwana Research*, Vol. 24, No. 1, pp. 243 – 274, 2013.
 49. Tirel, C., J.-P. Brun, E. Burov, M. Wortel, and S. Lebedev, “A plate tectonics oddity: Caterpillar-walk exhumation of subducted continental crust”, *Geology*, Vol. 41, No. 5, pp. 555–558, 2013.
 50. Hirth, G. and D. L. Kohlstedt, “Water in the oceanic upper mantle: implications for rheology, melt extraction and the evolution of the lithosphere”, *Earth and Planetary Science Letters*, Vol. 144, No. 12, pp. 93 – 108, 1996.
 51. Bird, P., “Continental delamination and the Colorado Plateau”, *J. Geophys. Res.*, Vol. 84, No. B13, 1979.
 52. Gogus, O. H. and R. N. Pysklywec, “Mantle lithosphere delamination driving plateau uplift and synconvergent extension in eastern Anatolia”, *Geology*, Vol. 36, No. 9, pp. 723–726, 2008.
 53. Şengör, A. and Y. Yilmaz, “Tethyan evolution of Turkey: A plate tectonic ap-

- proach”, *Tectonophysics*, Vol. 75, No. 3-4, pp. 181–241, 1981.
54. Okay, A. I. and M. Siyako, “The new position of the Izmir-Ankara Neo-Tethyan suture between Izmir and Balikesir (in Turkish). In: Turgut, S. (Ed.), *Tectonics and Hydrocarbon Potential of Anatolia and Surrounding Regions.*”, pp. 333–355, 1993.
 55. Okay, A., “Distribution and characteristics of the north-west Turkish blueschists”, *Geol. Soc. London, Spec. Publ.*, Vol. 17, No. 1, pp. 455–466, 1984.
 56. Ketin, I., “Tectonic units of anatolia (asia minor)”, *Bull. Miner. Res. Explor. Inst. Turkey*, , No. 66, pp. 24–37, 1966.
 57. Okay, A. I. and S. P. Kelley, “Tectonic setting, petrology and geochronology of jadeite + glaucophane and chloritoid + glaucophane schists from north-west Turkey”, *J. Metamorph. Geol.*, Vol. 12, No. 4, pp. 455–466, 1994.
 58. Pourteau, A., M. Sudo, O. Candan, P. Lanari, O. Vidal, and R. Oberhnsli, “Neotethys closure history of Anatolia: insights from $^{40}\text{Ar}/^{39}\text{Ar}$ geochronology and PT estimation in high-pressure metasedimentary rocks”, *Journal of Metamorphic Geology*, Vol. 31, No. 6, pp. 585–606, 2013.
 59. Fullsack, P., “An arbitrary Lagrangian-Eulerian formulation for creeping flows and its application in tectonic models”, *Geophys. J. Int.*, Vol. 120, pp. 1–23, 1995.
 60. Göğüş, O. H. and R. N. Pysklywec, “Near-surface diagnostics of dripping or delaminating lithosphere”, *J. Geophys. Res.*, Vol. 113, No. B11, p. B11404, 2008.
 61. J., B., “The strength of the Earth’s crust. I. Geologic tests of the limits of strength.”, *Journal of Geology*, Vol. 22, pp. 28–48, 1914.
 62. Jackson, J., “Strength of the lithosphere:time to abandon the jelly sandwich?”, *GSA Today*, Vol. 2, No. September, pp. 1–11, 2002.

63. Karato, S.-I., “Rheology of the deep upper mantle and its implications for the preservation of the continental roots: A review”, *Tectonophysics*, Vol. 481, No. 1-4, pp. 82–98, 2010.
64. Rychert, C. A., K. M. Fischer, and S. Rondenay, “A sharp lithosphereasthenosphere boundary imaged beneath eastern North America”, *Nature*, Vol. 436, No. 7050, pp. 542–545, 2005.
65. Fischer, K. M., H. A. Ford, D. L. Abt, and C. A. Rychert, “The Lithosphere-Asthenosphere Boundary”, *Annu. Rev. Earth Planet. Sci.*, Vol. 38, No. 1, pp. 551–575, 2010.
66. Plunder, A., P. Agard, C. Chopin, A. Pourteau, and A. I. Okay, “Accretion, underplating and exhumation along a subduction interface: From subduction initiation to continental subduction (Tavsanlı Zone, W. Turkey)”, *Lithos*, 2015.